2010-12-14

Contrasting View on Asphaltene and Human Cardiac Troponin I: A Surface Chemistry and Spectroscopy Perspective

Jhony Orbulescu
University of Miami, ojhony@gmail.com

UNIVERSITY OF MIAMI

CONTRASTING VIEW ON ASPHALTENE AND HUMAN CARDIAC TROPONIN I: A SURFACE CHEMISTRY AND SPECTROSCOPY PERSPECTIVE

By

Jhony Orbulescu

A DISSERTATION

Submitted to the Faculty
of the University of Miami
in partial fulfillment of the requirements for
the degree of Doctor of Philosophy

Coral Gables, Florida

December 2010

UNIVERSITY OF MIAMI

A dissertation submitted in partial fulfillment of
the requirements for the degree of
Doctor of Philosophy

CONTRASTING VIEW ON ASPHALTENE AND HUMAN CARDIAC TROPONIN I: A SURFACE CHEMISTRY AND SPECTROSCOPY PERSPECTIVE

Jhony Orbulescu

Approved:

_____ Roger M. Leblanc, Ph.D. Professor of Chemistry	_____ Terri A. Scandura, Ph.D. Dean of the Graduate School
_____ Thomas K. Harris, Ph.D. Professor of Chemistry	_____ Burjor Captain, Ph.D. Professor of Chemistry
_____ Jacqueline E. Dixon, Ph.D. Professor of Geological Sciences	

ORBULESCU, JHONY (Ph.D., Chemistry)

Contrasting View on Asphaltene and Human Cardiac Troponin I: A Surface Chemistry and Spectroscopy Perspective (December 2010)

Abstract of a dissertation at the University of Miami.

Dissertation supervised by Professor Roger M. Leblanc.
No. of pages in text. (173)

Surface chemistry has proven in the recent years that it could be used for a variety of applications. In the current work, the surface chemistry and spectroscopic techniques are used to emphasize their great potential in aggregation studies of UG8 asphaltene and the contrasting results for a surface chemistry perspective for the human cardiac troponin I. The first part of the work focuses on the influence of different spreading solvents on the aggregation of UG8 asphaltene and their comparison to the literature on the topic. It is shown that the surface chemistry approach employed in the current work has significant advantages compared to the methods used until today. The second part of the work focuses on the characterization of monoclonal antibodies and human cardiac troponin I and the use of monoclonal antibodies for the detection of human cardiac troponin I that could eventually lead to the development of a fast, cheap and selective bioassay to detect human cardiac troponin I in blood or blood serum. Different avenues are discussed to study the interaction between antibodies and human cardiac troponin I such as air-water interface and surface-bound antibodies. While detection of human cardiac troponin I was successful alternative approaches to improve the sensitivity are proposed.

To my parents

ACKNOWLEDGEMENTS

My special thanks go to Dr. R. M. Leblanc for being a great advisor, mentor and friend for the past decade. In addition to his guidance and teachings, I truly appreciate his patience and freedom in research.

I would like to thank my doctoral committee: Dr. B. Captain and Dr. T. K. Harris for their valuable insight and advice during the past years. I would like to extend my thanks to Dr. J. Dixon for her advice, discussions and help; without her assistance, it would not have been possible to get my Ph.D.

I would like to thank Dr. S. Daunert for the helpful discussions and troponin samples and also to Dr. O. Mullins (Schlumberger) for his valuable input and gift of UG8 asphaltene.

I acknowledge the help of Dr. M. Micic for the gift of chemicals and mutant antibodies without which most of the work could not have been performed.

I would like to thank everyone in the Department of Chemistry for their help during the years especially Juanita Hernandez, Edward Torres, Dr. David Hudson and Cristian Moreno.

I would like to thank my fellow graduate students and friends at the University of Miami who made these years a memorable experience, especially Dr. P. Kele, Dr. G. Sui and Stefania Impellizzeri. In addition I would like to thank for their support to my friends Sorina Ailiesei and George and Runa Zalanca.

Finally, I would like to thank my parents, brothers and my sister for their continuous and unconditional love and support.

TABLE OF CONTENTS

Page

LIST OF FIGURES

Chapter 2

Chapter 4

LIST OF TABLES

Chapter 1. Introduction

Surface chemistry and spectroscopy of the Langmuir and Langmuir-Blodgett films are well established techniques for the study of amphiphilic molecules that can be spread on the water surface and their assembly studied as a function of compression. The main use of such techniques was related to the study of molecular orientation, packing, phase transitions and stability of films. One main characteristic of the molecules under investigation is to have a polar group and a hydrophobic chain (typically a hydrocarbon chain) in such a way that the polar group will be anchored in the water subphase while the long chain will be located in the air. Such a molecule is called an *amphiphile*. Early studies were related to the molecular orientation of the hydrocarbon chains. Are the chains perpendicular to the water surface or at a certain angle? If they are not perpendicular to the water surface, what is the angle with the normal to the surface?

For such films the solvent from which the molecules are spread on the water surface needs to fulfill certain conditions such as immiscibility with the water subphase and fairly fast evaporation rate.[1] The first condition is required so that no amphiphile should be lost in the water subphase due to dissolution. The second condition, related to a fairly fast evaporation rate, is needed to ensure that during the surface chemistry studies, the amphiphile is the molecule under study and therefore no solvent molecule should be present. The presence of the solvent could alter and hinder the study of the amphiphile. Good solvents that could be used, that fulfill these two conditions, are chloroform and hexane. In some cases a small amount of ethanol or methanol in small portions (chloroform: (M)EtOH: 9:1, v/v) could be also used. The addition of the ethanol or

methanol is justified for the molecules that are not readily soluble in chloroform. Same mixtures with alcohols can be used in combination with hexane.

In the latest years, the application of the surface chemistry and spectroscopy techniques show a growth in diversity of application as the experimental techniques evolved. A summary of the specialized techniques are explained in Chapter 2, in detail, while the more common analytical techniques are briefly mentioned.

In Chapter 3, the evaporation time of the spreading solvents is investigated. It will be shown that other solvents used in Langmuir film studies such as toluene and benzene that were known to evaporate from the water surface in a fairly fast manner, actually do not. A common evaporation time generally accepted in the Langmuir film studies at the air-water interface is about 10 – 15 min. It will be shown using UV-vis spectroscopy at the air-water interface that these aromatic solvents in fact require a time period of 1 h at 20ºC or if the water subphase is heated to 40ºC the evaporation rate is increased and the waiting time for evaporation is then reduced to 10 min.

A direct application of the findings described in Chapter 3 are reported in Chapter 4 related to the investigation of the surface chemistry and spectroscopy of asphaltenes using solvents such as toluene and benzene (that evaporate fairly slow) and chloroform (evaporates in 15 min).

Asphaltenes are a component from crude oil and are the leading cause of pipeline obstruction. Because of this fact, it is the main cause for spills caused by pipe burst and leading to environmental issues. It is estimated that the asphaltene causes a loss to the crude oil industry estimated to $250 million dollars per day. Because of these facts asphaltene was the topic of research for several decades.

The factors that determine whether a newly precipitated solid phase actually forms a deposit which then grows and occludes pipelines and production facilities involve not only the oil chemistry but are compounded by interfacial interactions of the organics with oil, water, gas, mineral, and metal surfaces.

Asphaltenes are known to be surface active, as its main component belongs to hydrocarbons. Based on this fact, any questions related to the interfacial science of crude oils will most likely have a component that involves asphaltenes. Issues related to emulsion, stability, deposition or wettability involve interfaces.

Current research involves solution work using toluene as solvent or surface chemistry at toluene-water interface. Key issues are addressed in Chapter 4, such as presence of toluene within the asphaltene aggregates. Issues related to the time required for the toluene evaporation, therefore improper assignment of spectroscopic properties and nevertheless, the advantages of chloroform use in the asphaltene research, virtually inexistent until the present work was performed. The use of Atomic force microscopy revealed major differences in the aggregate size using different solvents.

Until now all the interfacial work was related to amphiphilic molecules that are not water soluble. The experimental conditions need to be changed if a water soluble molecule is under investigation, such as a protein.

Proteins can also be considered amphiphic molecules because they do posses polar and hydrophobic regions similar to a more typical amphiphilic molecule.

There are two reasons why the interfacial properties of a protein should be studied[2]: (i) to determine if the protein denatures at an interface, i.e. water surface; (ii) to determine if it interacts with lipid membranes.

Denaturation of a protein at the air-water interface can be viewed as a phase transition or aggregation similarly to an amphiphilic molecule that can form aggregates or domains. Some proteins have a tendency to denaturate and a major change in their secondary structure accompanies the denaturation process.

Regarding the second reason, with respect to interactions with lipid membranes, one could actually replace the lipid membrane with another protein and use the Langmuir film to study protein-protein interaction, or as the present case under study protein-antibody interactions.

The protein of choice for the Langmuir film studies was human cardiac troponin I (cTnI). This choice was based on the fact that this protein was basically not studied in great details from a surface chemistry and spectroscopy perspective. The human cardiac troponin I is part of a protein complex formed by troponin C, troponin I and Troponin T and are part of the human heart muscle related to contraction of the human heart. When a human suffers an acute myocardial infarction (AMI) some of the muscle cells are released in the blood stream. Human cardiac troponin I, myoglobin and creatine kinase-myoglobin (CK-MB) were the primary choices to be studied as cardiac biomarkers for point-of-care detection. In the latest years, troponin I became the preferred choice or the gold standard in assessing an AMI. Since at the moment there is no unified test to assess the presence of cTnI in the human blood (more than 100 tests are available) there is a lot of confusion regarding the choice of one test over a different one. One commonly accepted test is the use of surface plasmon resonance (SPR) for cTnI detection, although, there are major issues regarding false positives obtained with the SPR methodology.

Having in mind the importance of this protein, we have first decided to perform a systematic investigation of its interfacial properties. With both the solution and interfacial properties in hand, one could have a new insight regarding the possibilities for detection of cTnI. The complete surface chemistry and spectroscopic study of cTnI is the subject of Chapter 4. In parallel with the study of the cTnI, a suitable antibody that could bind cTnI was also investigated with the aim to develop a cheap fluorescence based bioassay.

The surface chemistry and spectroscopy of this antibody, mouse monoclonal immunoglobulin G mutant 560 (mab560), as well as the attempted binding studies with cTnI are presented in Chapter 5.

Due to the unsuccessful results using air-water interface, an attempt using a different antibody, mouse monoclonal immunoglobulin G mutant 19C7 (mab19C7), attached on a transparent solid substrate to detect cTnI from solution is presented in Chapter 6. Different attachment strategies are presented and the modified surfaces were extensively characterized. The proof-of-principle for the detection scheme is given and was found to be experimentally sound.

While typical amphiphiles do not aggregate at the air-water interface, it was found that asphaltenes in fact do aggregate regardless of the spreading solvent used. On the other hand, the opposite is shown for the human cardiac troponin I.

Using specialized techniques, a contrasting view on asphaltene and human cardiac troponin I was shown from a surface chemistry and spectroscopy perspective. In addition, the proof-of-principle for cTnI detection was demonstrated, using a simple bioassay based on a surface-attached mouse antibody.

Chapter 2. Methodology

2.1 Surface Tension

Molecules present in a liquid have a tendency to attract each other to an extent that depends on the substance under investigation. When these molecules are not in equilibrium/balance, for example the air-water interface, a larger attraction towards the liquid occurs. This effect is visualized in Figure 2.1.

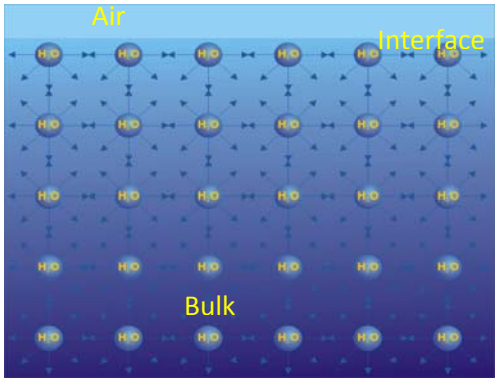

Figure 2.1. Air-water interface showing the interaction of molecules in bulk and at the interface.

This effect leads to the minimization of the surface and it is called *surface tension*. The same effect can be expressed as molecules at the interface have a certain free energy and can be expressed as the ratio of energy to the area.

Therefore, we can define:

$$\Delta G = Gibbs\ free\ energy$$

$$\gamma = \left(\frac{\partial \Delta G}{\partial S} \right)_{T,P,n_i} \qquad (2.1)$$

where, γ is the surface tension that is defined as the smallest change in the free energy (ΔG) per unit area (S) under constant temperature (T), pressure (P) and number of moles of the components (n_i).

2.2 Surface Pressure

Surface pressure is generally defined as the change in the surface tension when a film is present[1]. The presence of the film is reflected in a reduction of the surface for the pure component (water). Therefore, the surface pressure is defined as:

$$\pi = \gamma_0 - \gamma \tag{2.2}$$

where π is the surface pressure, γ_0 is the surface tension of the pure water and γ is the surface tension of the water with the film on top.

Regarding the units in which the surface pressure is measured, we can apply the definition for the surface tension:

$$units\ \gamma = \frac{energy}{surface} = \frac{joule}{m^2} = \frac{N \times m}{m^2} = \frac{N}{m} \tag{2.3}$$

Since surface pressure is the difference of two different surface tensions, it will have the same units of energy per surface, or more commonly used, force per distance (N/m).

It was determined experimentally that pure water has a surface tension of 72.6-72.8 mN/m at room temperature, which means the energy or the force is very small. Based on this example, all surface pressures will be expressed in mN/m.

The surface pressure is measured by the Wilhelmy plate-method. In this method a measurement is made by determining the force due to surface tension on a plate suspended so that it is partially immersed in the subphase (Figure 2.2). The Wilhelmy plate can be made of platinum, glass, metal or filter paper with the main property being the plate hydrophilicity (Figure 2.2).

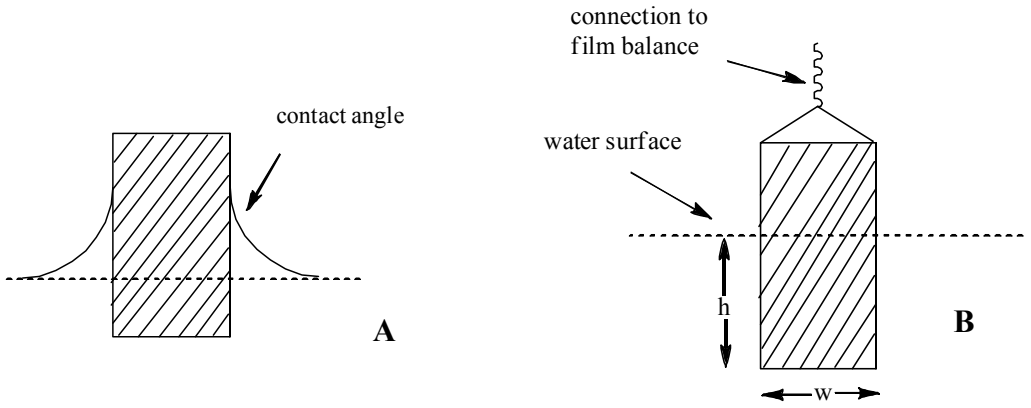

Figure 2.2. Diagram showing the required hydrophilicity of the Wilhelmy plate (**A**) and the connection of a partially immersed plate in water that is connected to the film balance (**B**).

2.3 Surface Pressure – Area Isotherm

When a film is spread on the water surface, it will be compressed by two barriers, which will be reflected in an increase of molecular density of the molecules at the air-water interface. This increase will cause the Wilhelmy plate to be pulled down and the vertical pull is converted by a film balance in surface pressure as shown in Figure 2.3. This effect is called surface pressure-area isotherm and is the fundamental property of a Langmuir monolayer.

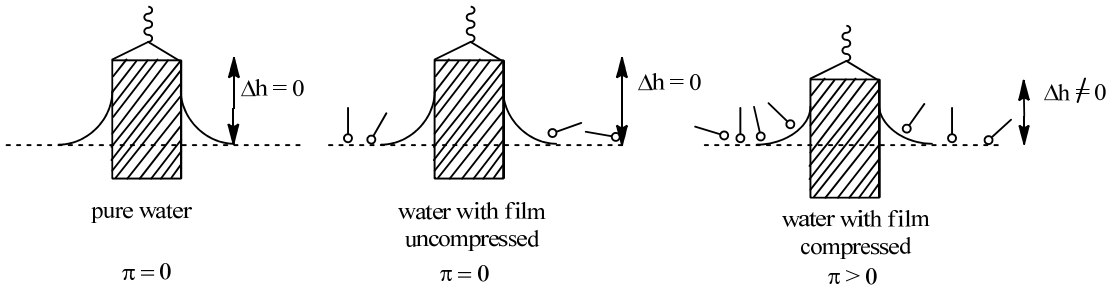

Figure 2.3. Illustration of surface pressure measurement using the Wilhelmy method at the air-water interface when a film is spread on the water surface.

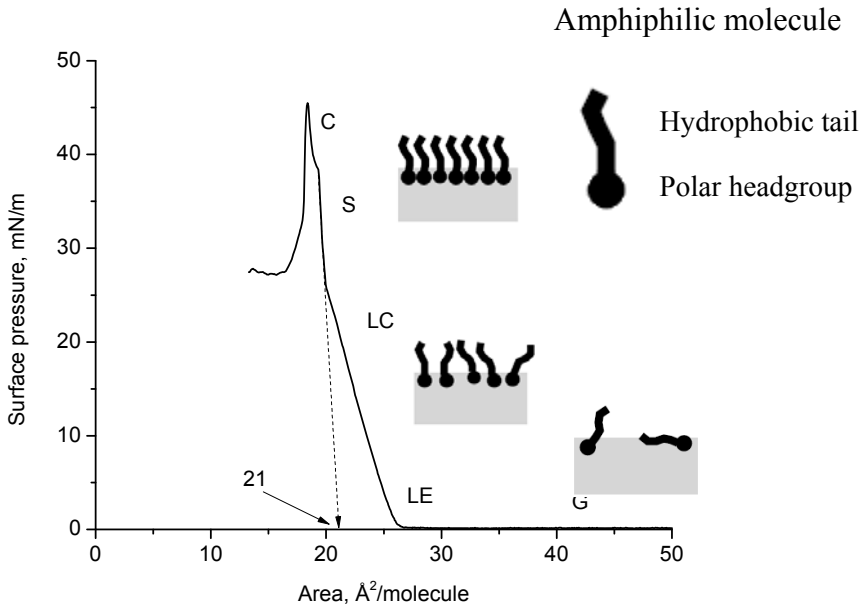

Figure 2.4. Surface pressure – area isotherm for stearic acid (10^{-3} M in $CHCl_3$), 75 µL spread and compressed after 15 min waiting time.

It is obtained by recording surface pressure (or interfacial pressure) versus the molecular area of the Langmuir monolayer. The surface pressure - area isotherm measures free-energy changes and reflects the packing status and phase behavior of the monolayer. In Figure 2.4, a typical surface pressure – area isotherm for stearic acid (CH_3-$(CH_2)_{16}$-COOH) is shown[3] on a trough with an area of 225 cm^2. The molecular constituents consist of a hydrocarbon chain and a polar headgroup that is submerged in the water subphase, whereas the hydrophobic chain stays in the air. The shape of the isotherm shows typical physical states of a monolayer. This includes a gaseous phase (G) in which the molecules have large distance between them. Therefore, the molecules behave in a similar way to a gas in which the molecules behave independently, and their orientation on the water surface is completely random. When such a monolayer is compressed, a

stage of liquid expanded (LE) is reached. In this case, some ordering between the headgroups appears, whereas the hydrocarbon chains are still randomly orientated. Upon further compression, the liquid condensed phase (LC) is reached. There are cases where this transition is clearer than in other cases, and it all depends on the size and nature of the headgroup (neutral or charged). The only way to discriminate between them in many cases is by their compressibility. LC state is less compressible than an LE state. The next physical state is the solid state (S). This state can be present or not and depends not only on the headgroup but also on the type of the hydrocarbon chain (linear or non-linear) and its length. If the hydrocarbon chain contains less than between 10 and 14 carbon atoms, the monolayer will have the LC state, as highest state. But if the hydrocarbon chain has between 14 and 22 carbon atoms it will reach the S state for a linear hydrocarbon chain. This is the state with the smallest compressibility of all, or no compressibility whatsoever. The lack of compressibility is translated to a high increase in the surface pressure for a very small decrease in the molecular area. Another property of the surface pressure – area isotherms is the extrapolation of the linear portion of the plot which gives the smallest area occupied by a single molecule and therefore called limiting molecular area. If a monolayer is compressed beyond this point, the monolayer will buckle and collapse, which is the last physical state of a monolayer, the collapsed state (C).

These measurements are possible when the monolayer forming molecules are insoluble in water and need to be dissolved in an organic solvent that has a fairly fast evaporation rate (chloroform b.p. 61ºC or n-hexane b.p. 69ºC are good solvents).[2]

The schematic of the experimental setup to measure the surface pressure – area isotherm is shown in Figure 2.5[4].

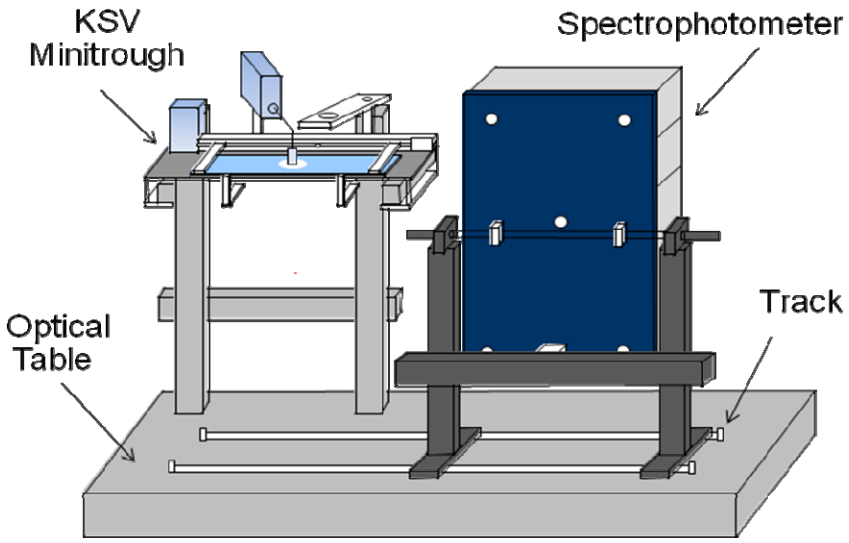

Figure 2.5. KSV Langmuir minitrough suitable for surface pressure, surface potential, UV-vis and fluorescence at the air-water interface.

The case presented above is for insoluble monolayers at the air-water interface that have in their structure a clearly defined hydrocarbon chain and a polar headgroup. What if one wants to obtain a monolayer of a biomolecule (enzyme, protein or peptide)?

A monomolecular film can be obtained even in the case of water soluble biomolecules that are indeed miscible with water. There are two ways to obtain a monolayer for this particular case that will be briefly explained below:

a) If the biomolecule of interest is available in large amounts, a Gibbs monolayer can be formed.

If sufficient protein is available, a solution of a certain concentration in water or buffer could be injected in the water subphase as shown in Figure 2.6. Depending on the protein, it can take several hours or days until equilibrium is reached between the molecules in the subphase and interface, which continuously exchange position.

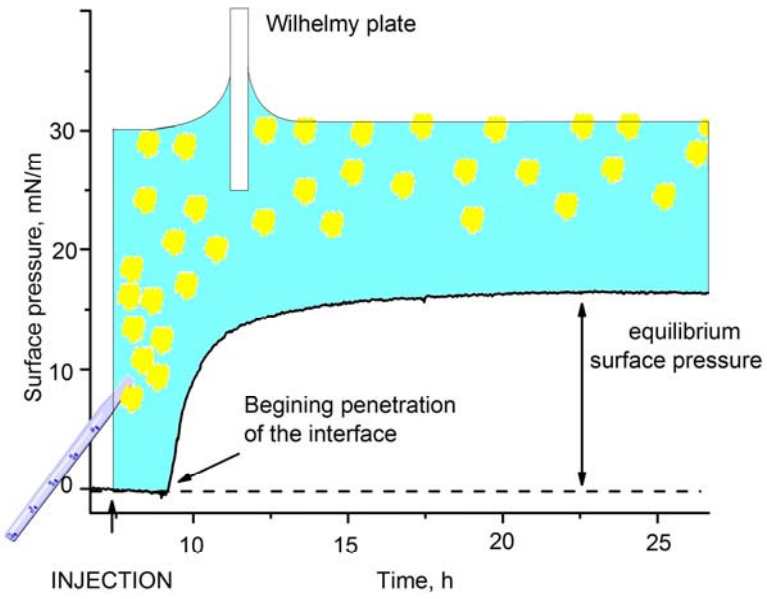

Figure 2.6. Formation of a Gibbs monolayer using an injected protein in water.

When the injected molecules start to diffuse in the bulk and some of them reach the interface, the surface tension starts to decrease, and this can be corelated to an increase in the surface pressure following its definition. After a certain time, equilibrium is reached. The drawback of this method is the extended time period required to reach the equilibrium surface pressure, which in turn means that evaporation of the subphase water could be a factor. Because fairly large volumes of subphase are required, in addition to the previously mentioned factors, this method is not often used.

b) If the biomolecule is extremely limited, the ionic strength of the water subphase needs to be changed and a Langmuir film can be formed in this case. This statement is supported by the opening remark made by Irving Langmuir[5]: *"Many proteins, although soluble in water, may be spread on a cleaned water surface to form insoluble monomolecular film"*. Moreover, in the same manuscript Irving Langmuir goes even

further to explain this phenomenon by saying that *"It is remarkable that, although many proteins are very soluble in water, the monolayers formed from them are extraordinarily insoluble….Substances form insoluble monolayers on a water surface only if the surfaces of their molecules have both hydrophilic and hydrophobic parts."*

As proteins have both hydrophobic and hydrophilic regions it makes sense for them to be stable on the water surface. To further limit the protein dissolution in the water subphase, the use of a salt (KCl) is justified by the following factors:

i) A high concentration of salt will require more water molecules for the hydration of the ions (K^+ and Cl^- if KCl is used) thus reducing the number of water molecules available to hydrate the protein.

ii) A high concentration of salt will increase the viscosity of the solution which in turn will cause the protein to stay on the water surface.

iii) Inserting a syringe just below the surface and spreading the protein or spreading the protein by lowering a droplet of protein solution until touches the salt surface is equally acceptable[6].

Based on the brief explanation of the Langmuir and Gibbs monolayers, all present work is related to Langmuir monolayers using organic solvents for insoluble monolayers or changing the ionic strength of the water subphase when a protein is used to form the Langmuir monolayer.

2.4 Surface Potential – Area Isotherm

The change in phase boundary potential produced by an interfacial film is defined as the interfacial potential or surface potential, ΔV. By recording surface potential versus molecular area, surface potential-area isotherm (ΔV–A isotherm) can be obtained. There

are two methods to record surface potential: the ionizing electrode method and the vibrating plate method.[1] Both methods measure the potential difference between two electrodes, one in the subphase and the other in the air. The ionizing electrode method uses a radioactive air electrode to ionize the gap between the air electrode and the surface and to make it conducting. The vibrating plate method is (Figure 2.7) a capacity method, using alternating current generated by the air electrode to detect the potential change of the surface.[1]

From the surface potential-area isotherm, information about the molecular orientation and heterogeneity in the film can be obtained. Surface potential depends primarily on three factors. These are the concentration of film molecules, the contributions from the dipoles in the film, and, in the case of a charged monolayer, the electrical potential Ψ_0, in the plane of charged groups. Surface potentials can be interpreted by the following equation:

$$\Delta V = 4\pi n\mu/D + \Psi_0 \qquad (2.4)$$

where n is the number of dipoles (usually molecules) per unit area, μ is the effective interfacial dipole moment in the perpendicular direction, and D is the dielectric constant, which is normally assumed to be unity. μ can be interpreted by

$$\mu = \bar{\mu}\cos\theta \qquad (2.5)$$

where $\bar{\mu}$ is an intrinsic moment that makes an angle θ with the vertical direction. For non-charged monolayers, $A\Delta V$ is proportional to μ, thus the molecular orientation angle θ can be obtained. For charged monolayers, the effect of Ψ_0 can be studied by keeping constant the area of the monolayer to fix the term $4\pi n\mu/D$ in equation (2.4). Then change

the subphase pH or ionic strength to change the charge status of the monolayer, and record the change of ΔV.

Surface potential is also a valuable method for detecting heterogeneity in the monolayer. When moving the air electrode over the surface, the presence of heterogeneity is made evident by wild fluctuations of the potential. This can be used to investigate the completeness of spreading or phase changes in monolayers.

The overall dipole moment can be decomposed to yield parallel ($\mu_{\parallel}$) and perpendicular ($\mu_{\perp}$) dipole moment with respect to the water surface. When measuring the surface dipole moment, only the perpendicular dipole moment is measured (Eq. 2.6), whereas the parallel dipole moments cancel due to random orientation in the x-y plane.

$$\mu_{\perp} = \frac{1}{4\pi} \cdot \frac{\Delta V}{n} \text{ with } \mu_{\parallel} = 0 \qquad (2.6)$$

where n is the number of molecules per cm^2 and ΔV is the surface potential. Experimentally, the area is expressed in $Å^2$/molecule, and the surface potential in millivolts (mV). When this term is replaced in equation (2.6) the expression for the surface dipole moment is given in millidebye (mD):

$$\mu_{\perp} = \frac{A \cdot \Delta V}{12\pi} \qquad (2.7)$$

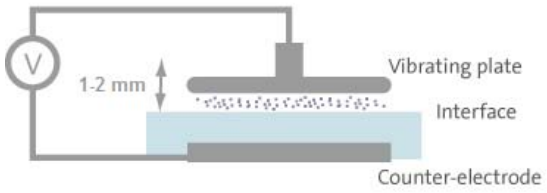

Figure 2.7. Capacitance method to detect changes in the surface potential.

2.5 Langmuir-Blodgett Film

Monolayers at the air-water interface can be transferred on to solid support by two methods: Langmuir-Blodgett (LB) deposition and Langmuir-Schaefer (LS) transfer. In the current investigation, both techniques were used. The LB technique involves the vertical movement of a solid substrate through the monolayer surface.[7] The surface pressure and the temperature are maintained constant in order to keep constant conditions during deposition. Since the transfer process is critically dependent on the surface pressure it is generally desirable to make depositions at surface pressures not less than 10 mN m^{-1} but not above the collapse surface pressure. Outside this range the depositions are seldom successful. There are three possibilities to deposit multilayers using the LB technique, namely "x", "y" and "z" type of depositions as illustrated in Figures 2.8 and 2.9.

The film transfer is characterized by measurement of the transfer ratio (R), which is expressed as the decrease in the area occupied by the monolayer (A_l) on the surface divided by the coated area of the solid substrate (A_s).

$$R = \frac{A_l}{A_s} \qquad (2.8)$$

The closer the value of R is to unity the more successful the deposition is. The final molecular arrangement in a LB film is not always as shown in Figure 2.8. It mainly depends on the particular molecule that forms the film. The driving forces for the rearrangement of the molecules during deposition may originate from interactions such as those between polar headgroups, between hydrocarbon tails or between head and tails of the molecules and the water molecules of the subphase[2].

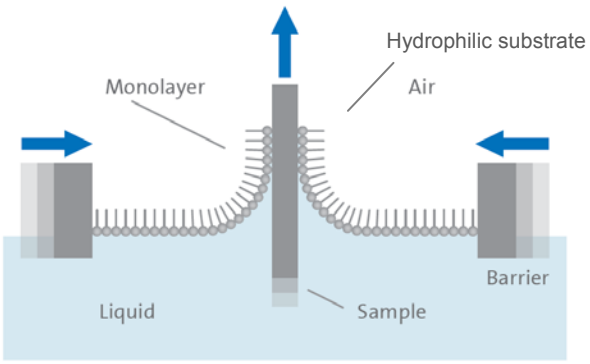

Figure 2.8. Illustration of Langmuir-Blodgett technique.

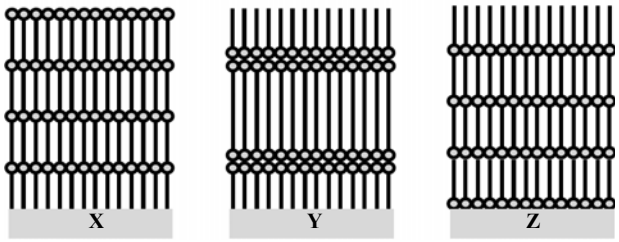

Figure 2.9. Langmuir-Blodgett film deposition with different possible molecular arrangement.

2.6 Langmuir-Schaefer Film

In contrast to LB deposition, the Langmuir-Schaefer deposition (Figure 2.10) is mainly used only hydrophobic substrates and for the transfer of a single monolayer onto the solid substrate. Seldomly, one would attempt to deposit multilayers using the LS technique. Even though it is very useful it is a method more exposed to experimental error, which is user error. The LB technique, as shown in Figure 2.8, allows the substrate to be held tightly with a clamp or holder, and mechanically dipped in the subphase or retracted and repeated, depending on the number of multilayers desired. The same accuracy cannot be obtained in the LS technique. After the monolayer is compressed to the desired surface pressure (Figure 2.10A), the user needs to hold the substrate parallel to the subphase with tweezers and carefully lower it at an angle until the substrate touches the subphase (Figure 2.10B).

The next step is to quickly change the angle of substrate until all of it comes in contact with the subphase onto which the monolayer is located (Figure 2.10C) and withdraw it (Figure 2.10D) just as quickly.

Therefore, the LS technique is a much quicker deposition method (only seconds required). In constrast, the LB technique requires tens of minutes for a single monolayer transfer and hours for multilayers, all depending on the size of the substrate.

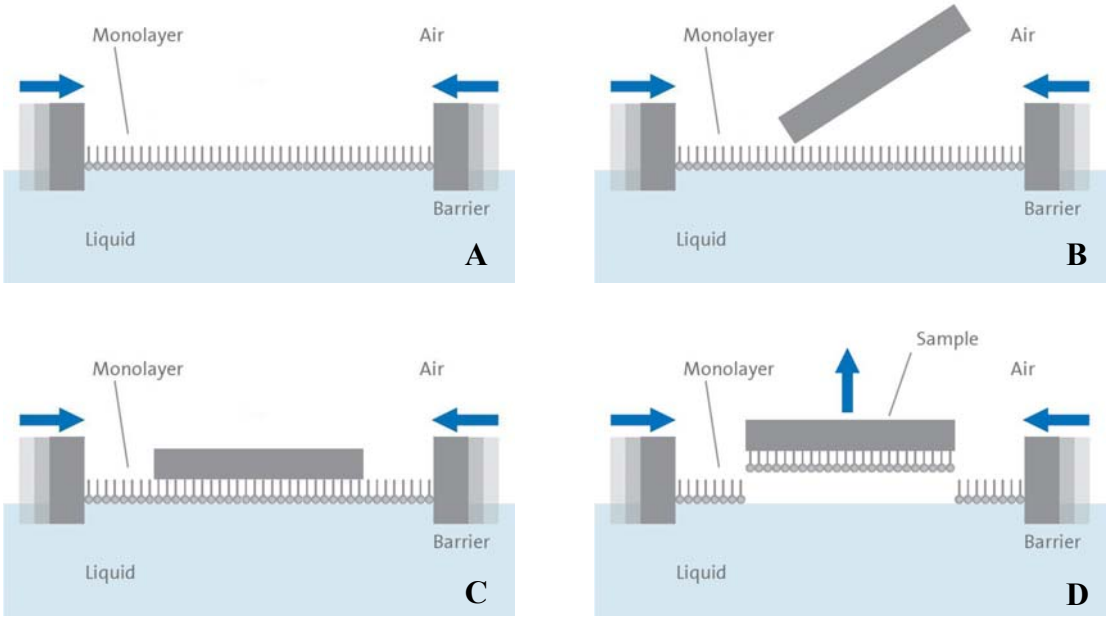

Figure 2.10. Illustration of the different steps required for a Langmuir-Schaefer technique.

The dipping or retraction speeds used for LB deposition are 1 mm/min. Typical substrates used for deposition are highly oriented pyrolytic graphite (HOPG), a very common hydrophobic substrate, and mica used in the deposition of proteins due to its hydrophilic and negatively charged surface. Other substrates can be used depending on the process under investigation. If absorption or fluorescence studies are of interest, hydrophilic or hydrophobic glass or quartz slides can be employed depending on the absorption maximum of the species under study, as the UV cut-off wavelength of glass is 360 nm. In

the present study, the substrate of choice was HOPG and quartz, as it will be explained in the chapters to follow.

2.7 Infrared Spectroscopy

The main application of infrared spectroscopy (IR) is related to its use in the identification of organic compounds based on the IR active groups present. However, the development of specialized IR techniques such as Bio-ATR and Infrared reflection-absorption spectroscopy, as will be shown below, extends the application of infrared spectroscopy not only to the identification of the groups that are IR active but also to studies on protein denaturation and molecular packing.

2.7.1 Bio-ATR Infrared Spectroscopy

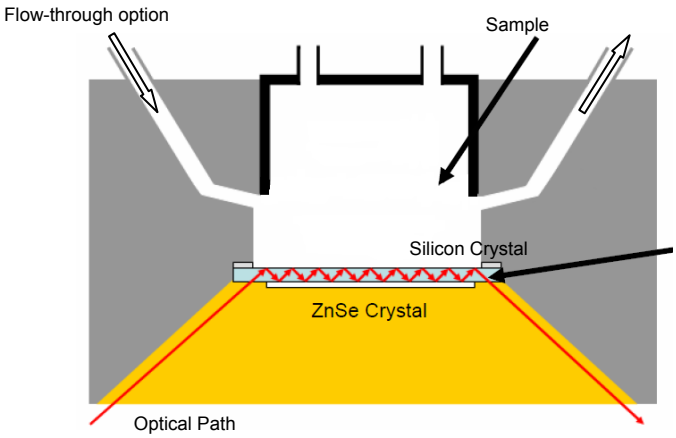

Figure 2.11. Diagram of the Bio-ATR cell.

Attenuated total reflectance (ATR) is a technique that can be used to obtain the infrared spectrum of a compound in a solid or liquid state. In ATR, the solid or liquid is placed on top of the ATR crystal (silicon, germanium or KRS-5), and it is pressed firmly against the crystal. In Bio-ATR[8], there is no need to press the sample that can be placed on top of the ATR crystal, and the IR spectrum can be readily obtained. The advantages of this method (Bio-ATR cell II is shown in Figure 2.11) are that it can be used in static

mode, a solution is placed on top the crystal and the spectrum acquired, or in a flow-through design. The static mode requires only 15 – 20 µL of solution, with the only specification that its concentration should be larger than 0.5 mg/mL in order to have enough sample in contact with the ATR crystal. In flow-through mode, a volume between 100 – 200 µL is sufficient to obtain the desired spectrum. The acquisition speed depends on the type of detector used and the scanner velocity. In the present work, a mercury-cadmium-telluride (MCT) detector (Kolmar Technologies) was used with a scanner velocity of 5 KHz. Pure solvents were used as background before any measurements were performed in solution with the Bio-ATR cell II placed in the cell compartment of a Bruker Optics Equinox55 FTIR.

2.7.2 Infrared Reflection – Absorption Spectroscopy

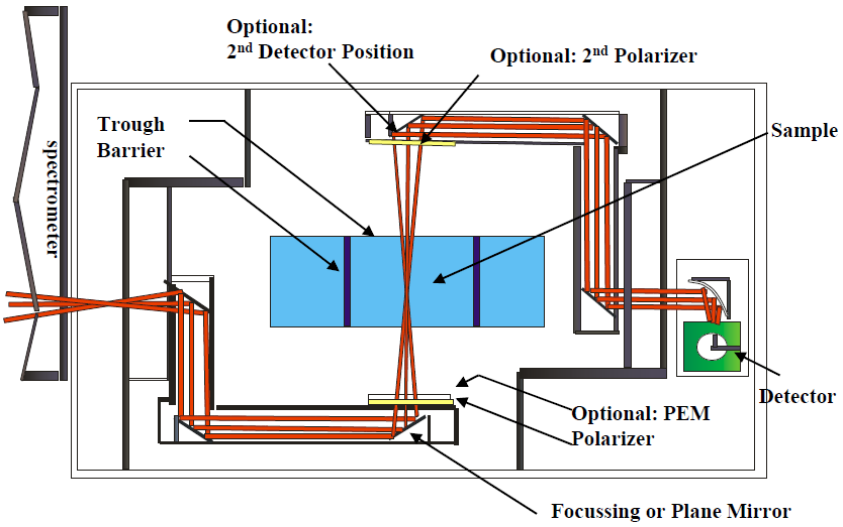

Figure 2.12. Air-water interface accessory for Infrared Reflection-Absorption Spectroscopy.

Reflection-absorption spectroscopy was first applied to Langmuir-Blodgett films of metal stearates on the surface of metallic mirrors[9]. Since its discovery the technique

was improved and mainly employed for the calculation of molecular orientation in thin films on metallic substrates[10], glass slides[11,12] and air-water interface.[13-16]

The main components of the instruments for Infrared Reflection-Absorption Spectroscopy (IRRAS) are given in Figure 2.12. Connected to an FT-IR spectrometer are two movable arms that contain fixed mirrors that provide the optical path for the IR beam. Just before the IR beam hits the air-water interface, there is a polarizer that allows the selection of the desired polarized light (s- or p-polarization) depending on the experiment required to be run. All current work was performed using p-polarized light because the signal in p-polarized light flips from negative to positive or viceversa therefore allowing an easy way to identify IR weak absorption bands. This is not the case for s-polarized light. After interaction with the beam there is either a flat or focusing mirror, depending on the position of the Mercury-Cadmium-Telluride (MCT) detector. If the detector is placed in the second position a parabolic focusing mirror is required. An optional Photoelastic Modulator (PEM) is shown. This is used when polarization-modulation IRRAS (PM-IRRAS) is required to be performed. The difference between IRRAS and PM-IRRAS is the way the actual signal is calculated and their application. While in IRRAS the intensity of the light is measured for either s- or p-polarization, IRRAS requires the measurement of a background spectrum (for p-polarization, the absorbance is defined as $A_{Ip}=log(I_p/I_p^0)$, with I_p as the intensity of the p-polarized light for the sample scan and I_p^0 being the intensity of the p-polarized light for the background), there is no such requirement in PM-IRRAS. This is due to the fact that in PM-IRRAS, $A=(I_p-I_s)/(I_p+I_s)$, where I_p and I_s are the intensities of p- and s-polarized light, respectively. The advantage of PM-IRRAS is that the spectral output is not affected

by the presence of the water vapors, while IRRAS suffers from this drawback. But PM-IRRAS has its own drawback, where it has a poorer signal to noise ratio (S/N) compared to IRRAS. This drawback comes from the way the signal is measured in PM-IRRAS. Each signal, I_p and I_s will have its own S/N. Here, subtracting, adding and taking the ratio of them will increase the noise of the output leading to a decrease in S/N for PM-IRRAS. Even as of today, there is still a debate as of which technique is better. Research groups from France (Desbat B.) and Canada (Pezolet M.) prefer PM-IRRAS based on its water vapor compensation benefit,[17-20] whereas groups from United States prefer IRRAS.[21-26] In IRRAS there are two ways to compensate the water vapors. The first involves adding additional water troughs that would saturate the environment with water vapors so that their contributions are the same. Alternatively, the closed system is purged with compressed N_2 gas at slow flow rates during the measurements to provide a low water vapor concentration that is maintained constant. The latter method was the one used in the current work since it seemed to yield more consistent results.

2.8 UV-vis Spectroscopy

For the solution UV-vis measurements a UV-VIS-NIR instrument was used (Lambda 900, Perkin-Elmer) available in the Department of Chemistry. Unless otherwise specified an optical path length of 1 cm was used throughout the solution work. For the *in situ* UV-vis measurements on Langmuir films at the air-water interface, an HP Spectrophotometer (model 8452A) settled on a rail close to a Langmuir trough was employed (Figure 2.5, page 12). The light passes through a quartz window located in the middle of the trough which is, in turn, placed inside the sample compartment of the spectrophotometer. The subphase without any Langmuir film on top was taken as blank,

as the measurements were performed as a function of time or surface pressure, as will be explained in the following chapters.

2.9 Fluorescence Spectroscopy

The fluorescence spectra obtained in solution were performed on a Fluorolog-3 spectrofluorimeter (Horiba Scientific) equipped with a 450 W Xenon short arc lamp. For all solution measurements a fluorescence cuvette (Hellma, Plainview, NY) with an optical path length of 1 cm was used. The fluorescence spectra of the monolayer at the air-water interface were measured using an optical fiber accessory fitted in the cell compartment of the Fluorolog-3 instrument. For excitation and emission, a bifurcated optical fiber that collects the backscattered fluorescence of the Langmuir film was used. For this purpose the bifurcated optical fiber is placed 1 – 2 mm above the air-water interface.

2.10 Epifluorescence Microscopy

Langmuir monolayer at the air-water interface can form domains or aggregates. If the molecule of interest has a built-in fluorophore, epifluorescence microscopy can be used as a visual tool to investigate the presence of the domains or aggregates. Another application of the epifluorescence microscopy is to visualize phase transitions that could occur during the monolayer compression.

The components of an epifluorescence microscope[27] are given in Figure 2.13. This methodology also requires a Langmuir trough that is placed on top of the sample stage. The Langmuir trough requires a quartz window to allow the excitation light to penetrate the subphase and excite the fluorophores at the air-water interface.

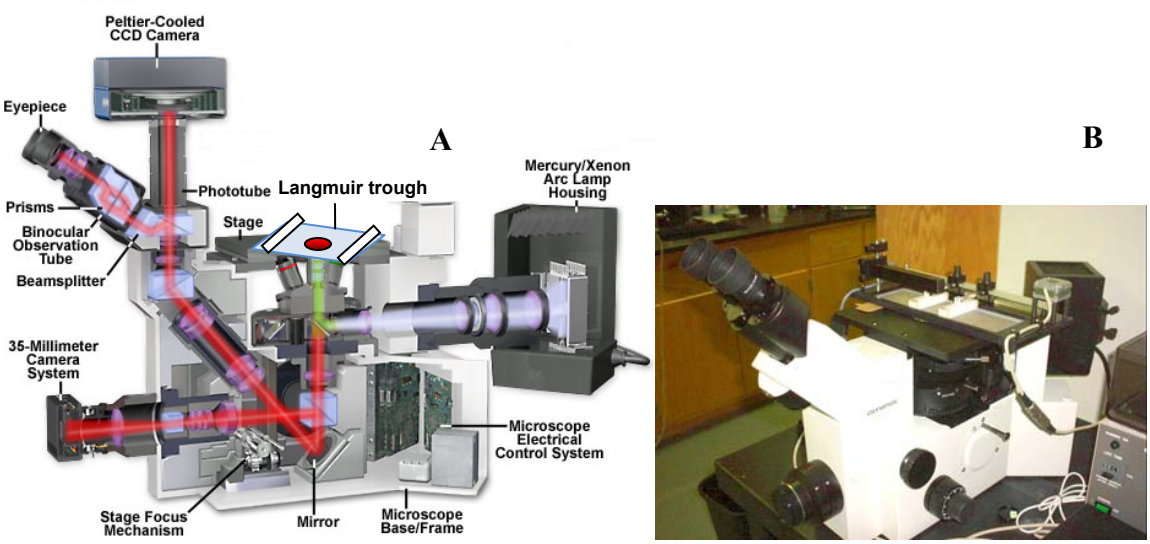

Figure 2.13. Components of the Olympus IX70 inverted microscope: internal view (**A**) and external view (**B**).

Only the backscattered fluorescence light is collected with this experimental setup, and the image obtained is the bottom of the monolayer in contact with the water subphase. The epifluorescence image can be visualized with the naked eye, a 35 mm-camera system or using a CCD camera. The experimental setup used in the present research used a Kibron minitrough (area available for spreading solution 5.9 × 19.5 cm^2, Kibron Inc., Helsinki, Finland) combined with an epifluorescence microscope (Olympus IX-FLA), and the epifluorescence image is captured by a thermoelectrically cooled Optronics Magnafire^{TM} CCD camera.

If there is no fluorophore present in the structure of the molecule of interest or the emission occurs in the UV region (intrinsic protein fluorescence), an amphiphilic molecule with a built-in fluorophore can be used as a contrast agent. In order for the contrast agent not to perturb the properties of the Langmuir monolayer under study, a very small concentration of the fluorophore is used (0.5 – 1%).

As an alternative, if a protein is under study, labeling with fluorescein isothiocyanate (FITC) could provide the contrast needed to visualize the protein monolayer.

In some cases, the addition of a fluorophore is not desired, e.g. limited amounts of protein or molecules that have absorption and the addition of a fluorophore can lead to Förster resonance energy transfer (FRET). If indeed, this is the case a different technique needs to be used, namely Brewster angle microscopy. This technique is summarized below.

2.11 Brewster Angle Microscopy

The reflectivity of an incoming light beam on the interface can be described by Fresnel equations (Eq. 2.9)[28]:

$$n_1 \sin\theta = n_2 \sin\phi \tag{2.9}$$

$$R_p = \frac{I_r}{I_i} \tag{2.10}$$

$$R_p = \left(\frac{\tan(\theta - \phi)}{\tan(\theta + \phi)} \right)^2 \tag{2.11}$$

where n_1, n_2: refractive index of the air and media, θ: incident angle of light, φ: refractive angle of light, R_p: reflectivity of the parallel component of the electric field, I_i, I_r: power of *p*-polarized incident and reflected light, respectively. The Brewster angle θ_B is defined as

$$\theta_B = \tan^{-1}\left(\frac{n_2}{n_1} \right) \tag{2.12}$$

From Eq. (2.9) to Eq. (2.11), we can see that R_p is a function of n, when $\theta=\theta_B$, $R_p = 0$, and the intensity of the parallel component of the reflection beam is zero. For air/water interface: $n_1 = 1$, $n_2 = 1.33$, $\theta_B = 53$ deg. Figure 2.14 shows the relationship between the

R_p and θ, around θ_B. While $\theta=\theta_B$, the presence of a monolayer at the air-water interface will increase the value of R_p because the intensity of the reflected light I_r will increase due to the refractive index of the monolayer, which means the presence of the monolayer does not satisfy anymore the condition that the reflected light is minimal, as shown in Figure 2.15.

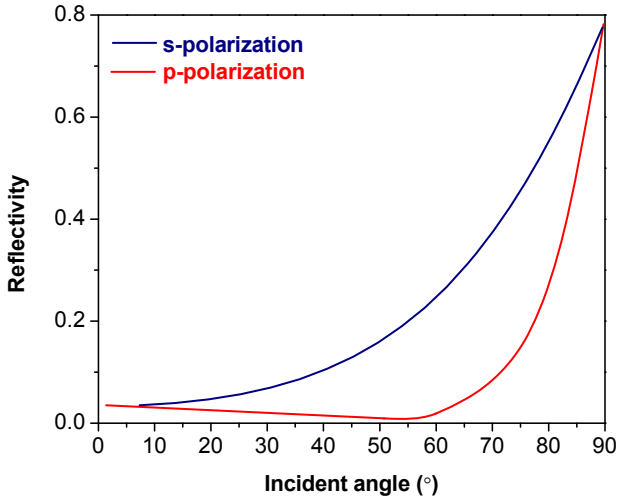

Figure 2.14. Reflectivity dependence on the incident angle for s- and p-polarized light.

In summary, if a *p*-polarized light beam is applied at the air-water interface at Brewster angle and the reflection light is monitored by a camera, a dark field will be observed. The existence of a monolayer at the air-water interface will be seen by the camera as a bright region. The brightness of the monolayer is a function of the refractive index of the monolayer. Different types of the molecules have different refractive index values. The packing density of the monolayer also affects the actual value of refractive index at the interface. Therefore, Brewster angle microscopy yields topographical information of the monolayers.

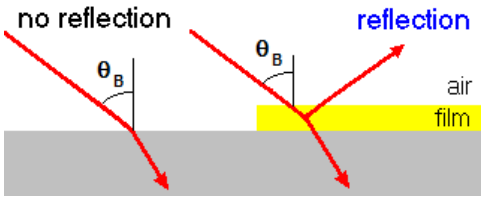

Figure 2.15. Diagram showing the Brewster angle for water (no reflection) and the change in the reflectivity when the monolayer is present (reflection is present).

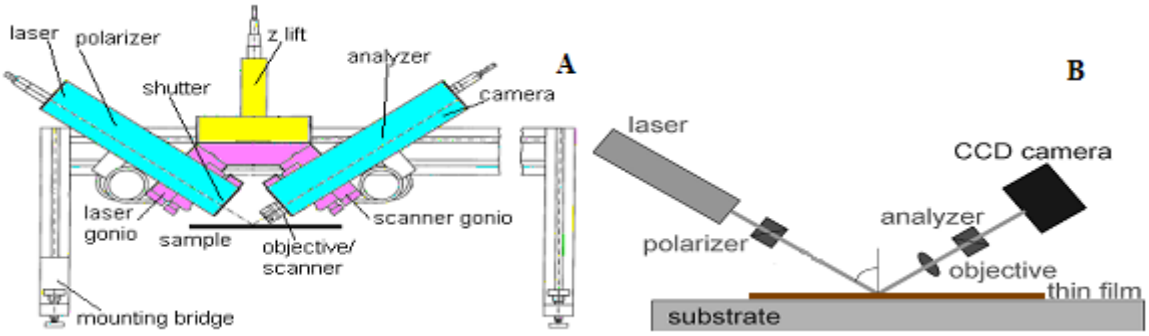

Figure 2.16. Diagram for the IElli-2000 imaging ellipsometer design (**A**) and main optical components (**B**).[29]

The measurements presented in this work were performed using the IElli-2000 imaging ellipsometer with the compensator turned off. Figure 2.16A shows a summary of the mechanical and optical components that allow changing the incident angle and the reflection, either in tandem or not, as the main optical components are located on two goniometers. In the left arm is located the laser source together with the polarizer and a shutter. The beam hits the sample, which in our case is the air-water interface, after which the reflected light goes into an objective, passes through an analyzer and finally into the camera that acquires the image. To allow the instrument to be focused on the air-water interface, a small motor controls the vertical movement (z-lift). The power of the laser, polarizer angle, shutter, focuse, objective movement, analyzer controls and the camera are all controlled by the BAM2Plus software. A simplified view of the instrument is presented in Figure 2.where the presence of a thin film increases the reflectivity.

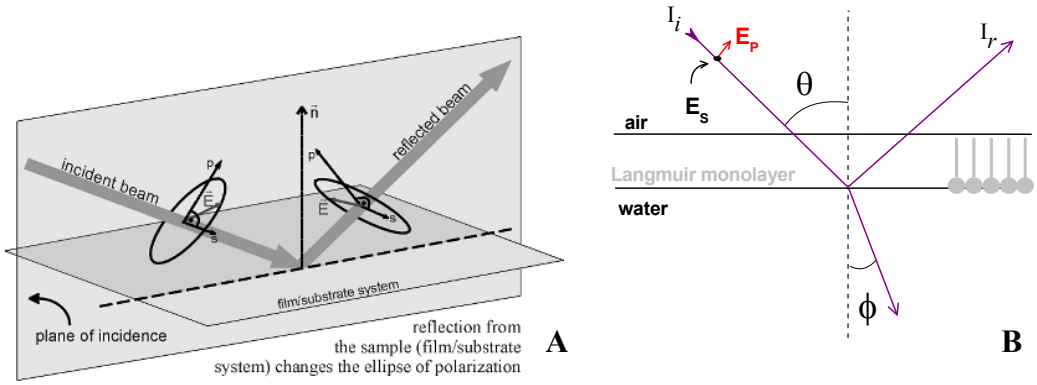

Figure 2.17. Depiction of the electric field vectors before and after the interaction with the sample[29] (**A**) and a close-up view of the interaction with the film (**B**).

The most important aspect regarding the principle of BAM imaging is that a polarized incident light changes its polarization after interacting with the sample (Figure 2.17A). Moreover, if the light is *p*-polarized at the Brewster angle of the subphase (water) the signal is nil. Therefore there is no reflected light. But the presence of the monolayer changes the refractive index of the medium, and therefore reflected light will appear (Figure 2.17B).

The standard laser of the BAM2plus is a frequency doubled Nd-YAG laser with a wavelength of 532 nm. The high-power laser has 50 mW primary output power in a collimated beam.

2.12 Atomic Force Microscopy

Atomic force microscopy is a technique used for the visualization of physisorbed or chemisorbed molecules on solid substrates. In the present work, the substrate of choice for the deposited LB and LS films is HOPG. Here, the deposited film is hydrophobic just like the substrate, and therefore makes the substrate suitable for deposition.

The main components of an atomic force microscope are given in Figure 2.18. Basically a laser beam is calibrated to hit the tip of a cantilever in a way that the reflected laser light is captured by a four-diode array detector. The contact of the cantilever with the surface will change the angle of the reflected beam, which will shift the position of the beam in the photodetector. An image is created from the different positions and intensities of the laser beam in the photodetector.

Atomic force microscopy (AFM) can be used for imaging in two different modes, contact and non-contact. The contact mode is used for hard films as the AFM cantilever is dragged on the surface and allows the imaging of the whole surface with high resolution (atomic resolution can be achieved in this mode).

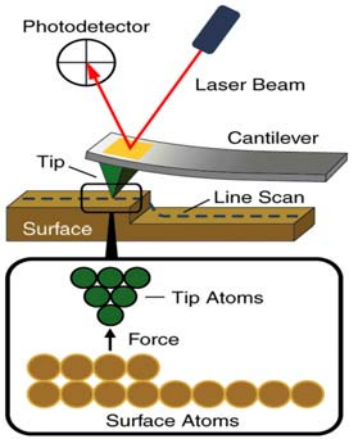

Figure 2.18. Atomic force microscopy principle.[30]

The second imaging technique, non contact or intermittent contact mode, can be used for "soft" surfaces, such as for imaging ultrathin films of organic molecules, biomolecules or polymers. These types of films cannot be imaged in contact mode as the cantilever can penetrate the film and the resulting image is either artifactual or a so-called false image produced by some regions within the film. In any case of soft films, the image obtained using contact mode will never reproduce the true topography of the imaged film.

When the cantilever and sample are close to each other, during each oscillation cycle, the tip moves through an interaction potential that includes both long-range attractive and short term repulsive components (Figure 2.19). The complex tip-sample forces cause changes in the amplitude, phase and resonance frequency of the oscillating cantilever. Thus, topography, amplitude and phase can be collected simultaneously. The phase and amplitude images may highlight physical properties that are not readily discernible in the topographic map. For example, fine morphological features are, in general, better distinguished in amplitude and phase images. The force of the oscillating tip is directed almost entirely in the z-axis; thus, very little lateral force is developed and tip/sample degradation is minimized. This benefit also makes it possible to obtain clear images of soft samples.

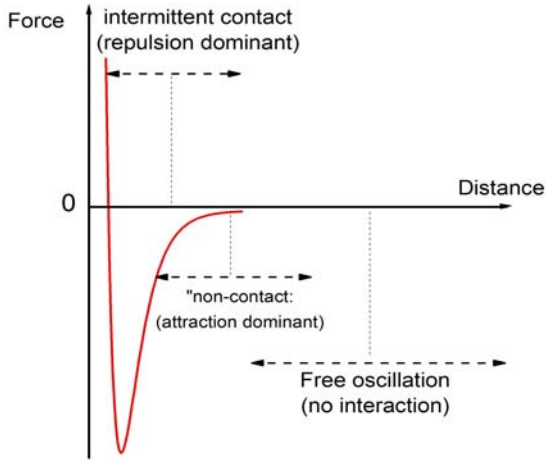

Figure 2.19. Force versus distance interaction between the AFM tip and the sample.

Alternating Current (AC) Mode AFM is another implementation of Intermittent Contact Mode AFM. In AC Mode AFM, the AFM cantilever is driven at its fixed end with a piezoelectric actuator that is positioned under the substrate to which the cantilever is attached. An alternating current (AC) voltage is applied to this actuator, whose

resulting motion is then amplified at the cantilever's free end, where the tip is. The AC mode was used for imaging, employing an Agilent AFM (model 5420). AC Mode can operate in either the intermittent contact (net repulsive) regime or the non-contact (attractive) regime. During intermittent contact, the tip is brought close to the sample so that it lightly contacts the surface at the bottom of its travel, causing the oscillation amplitude to drop (Figure 2.19). The tip is usually driven by a sinusoidal force, with the drive frequency typically at or near one of the cantilever's resonance frequencies (eigenfrequencies), and most often at the fundamental frequency. Absent any tip-sample interactions, the cantilever oscillations are also sinusoidal if the drive amplitude is small enough to keep the cantilever motion small compared with the cantilever thickness (Figure 2.20).

At the beginning of the measurement, the tip of the cantilever and the sample are separated by a large distance (Figure 2.20). As they approach, tip and sample atoms first weakly attract each other. This zone of interaction is known as the non-contact regime. Closer still, in the intermittent contact regime, the repulsive van der Waals force predominates. When the distance between tip and sample is just a few angstroms, the forces balance, and the net force drops to zero. When the total force becomes positive (repulsive), the atoms are in the contact regime. In the intermittent contact mode, the cantilever is oscillating near its resonance frequency; therefore throughout the measurements the frequency is set 0.1 kHz lower than the resonant frequency.

Interaction with the sample reduces the oscillation amplitude—this reduction is used as a feedback signal to maintain constant amplitude of the cantilever motion.

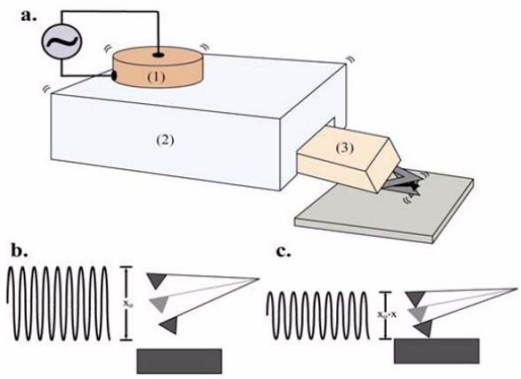

Figure 2.20. Description of the AC mode AFM: voltage applied to piezo (1) that controlled the vertical position of the cantilever holder (2) that has a secondary piezo (3) that shakes that cantilever near its resonant frequency (a); sinusoidal force with x_0 amplitude before contact (b) and decrease in the sinusoidal amplitude in contact with the sample (c).[30]

Chapter 3. Aromatic Solvent Evaporation at the Air-water Interface

Herein, it is shown that aromatic spreading solvents can be detected using in situ UV spectroscopy at the air-water interface beyond the common accepted time for evaporation of 10 – 20 min in the preparation of a Langmuir monolayer. Toluene and benzene, even though are not significantly surface active, can be detected, and their behavior as a function of time and temperature is investigated. To our knowledge, this is the first time that the vibrational fine structure of the benzenoid bands is detected at the air-water interface.

3.1 Background

During the years, the spreading solvent choices for researchers focusing on surface chemistry at the air-water interface has ranged from pure solvents such as chloroform, toluene[31,32] and benzene[33,34] to solvent mixtures such as chloroform or hexane : methanol or ethanol (5:1 or 9:1, v/v), depending on the characteristics of the amphiphilic molecule under study. The rationale to choose a spreading solvent is its immiscibility with the water subphase and a fairly fast evaporation rate.[1] The use of ethers as a spreading solvent is not recommended even though their evaporation is fast because it leads to cooling at the air-water interface (ethyl ether b.p. 35ºC). The variation in the surface tension of the subphase during compression of a Langmuir monolayer, also known as surface pressure, is monitored by the so-called surface pressure-area isotherm, which implies a constant temperature. Therefore, the cooling process is not desired. In this study the focus is on the use of pure solvents, more exactly on toluene, benzene and chloroform (as a reference), which have acceptable evaporation rates and are immiscible

with water. Throughout the literature on Langmuir monolayers at the air-water interface, there is a waiting time period that researchers are using to allow the spreading solvent to evaporate. What is expected is that the molecules remaining at the interface after solvent evaporation are the amphiphilic molecules under study. The waiting time period varies between different research groups around the world as the ambient temperature under which the measurements are performed, are slightly different. Some groups[35] prefer to use 25°C while others are using temperatures below this value. Temperatures higher than 25°C are used mostly if one would like to study the effect of temperature on the interfacial properties such as phase transitions, aggregation and domain formation. The generally accepted waiting time period for spreading solvent evaporation during the preparation of the Langmuir monolayer is between 10 and 20 min.[36,37] After this waiting time period, the generally accepted assumption is that the spreading solvent is completely evaporated and therefore has no influence on the interfacial properties.[38]

It is worthwhile mentioning that neither chloroform, toluene nor benzene are significantly surface active[38] (upon compression of pure solvent spread on the water subphase the maximum changes in the surface pressure are less than 0.5 mN/m).

During a control experiment using UV absorption at the air-water interface, we observed the presence of benzenoid absorption[39] bands when we spread pure benzene on the water surface at a time beyond the generally accepted waiting time period.

These observations lead us to a more rigorous investigation of this fact. For this purpose, we decided to use toluene and benzene for which their UV absorption spectra are well known (toluene and benzene with a peak maximum at 262 and 254 nm, respectively) and chloroform as reference (which does not absorb above 220 nm).

3.2 In situ UV-vis Spectroscopy

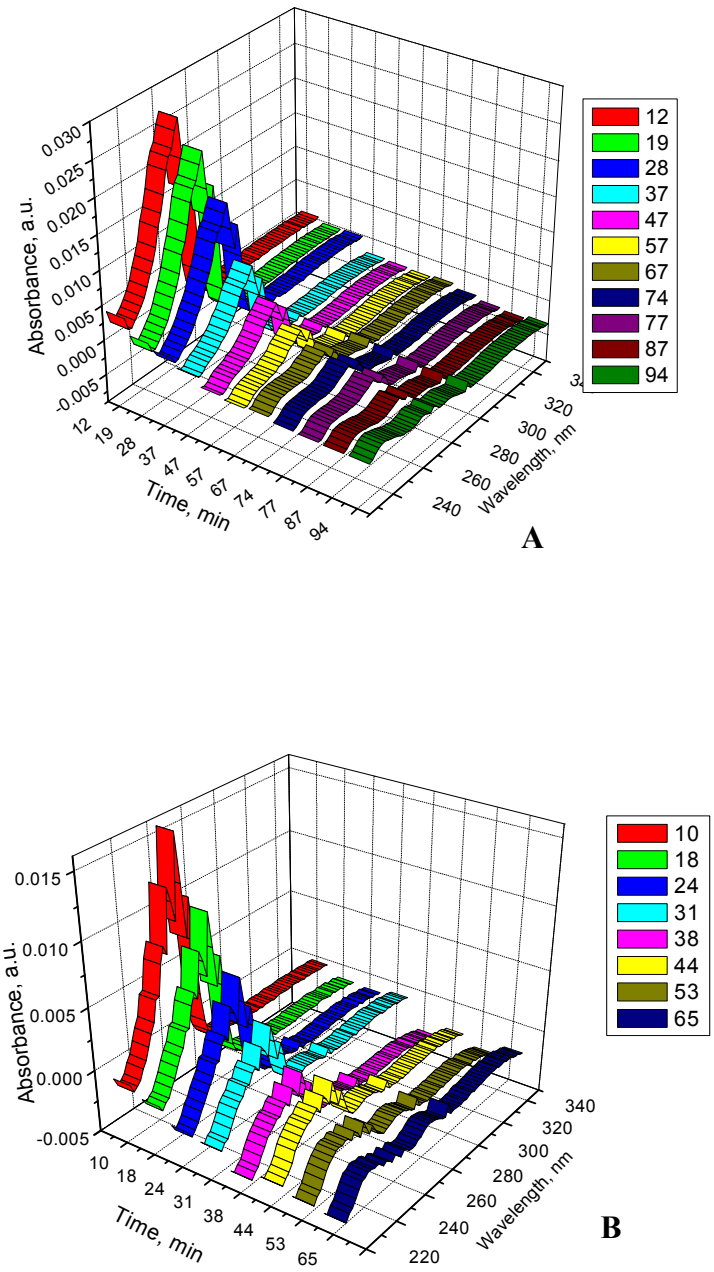

Figure 3.1. UV absorption at the air-water interface as a function of time for toluene (A) and benzene (B).

When toluene is spread on the water surface, the benzenoid absorption bands can be detected and are decreasing as a function of time (Figure 3.1A), which allows the detection of toluene well beyond 60 min. A similar dependence was obtained for benzene (Figure 3.1B).

In order to determine the effect of time on the absorbance, the peak maximum at 262 nm (typical for toluene) was plotted as a function of time, as shown in Figure 3.2, and then fitted mathematically.

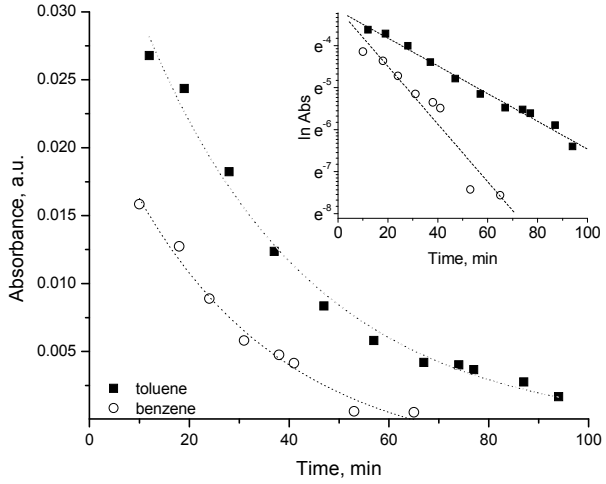

Figure 3.2. Absorbance at the air-water interface as a function of time for benzene (○) at 254 nm and toluene (■) at 262 nm at a temperature of 20.0 ± 0.5°C. Inset: ln (Abs) vs. time showing the linear dependence.

As can be seen from Figure 3.2, we have determined that the absorbance is decreasing exponentially with time. The inset shows that ln (Abs) as a function of time gives a linear dependence. This behavior can be described by the following equation:[40]

$$C=C_0e^{-kt} \qquad (3.1)$$

where C is the concentration of toluene at the air-water interface at time t; C_0 is the initial concentration of toluene and k is a constant depending of the solvent. The mathematical

treatment is performed on both data on toluene and benzene. As expected the slope for benzene is steeper compared to the slope for toluene, (see Inset in Figure 3.2) as benzene has a lower boiling point and a higher evaporation rate than toluene.

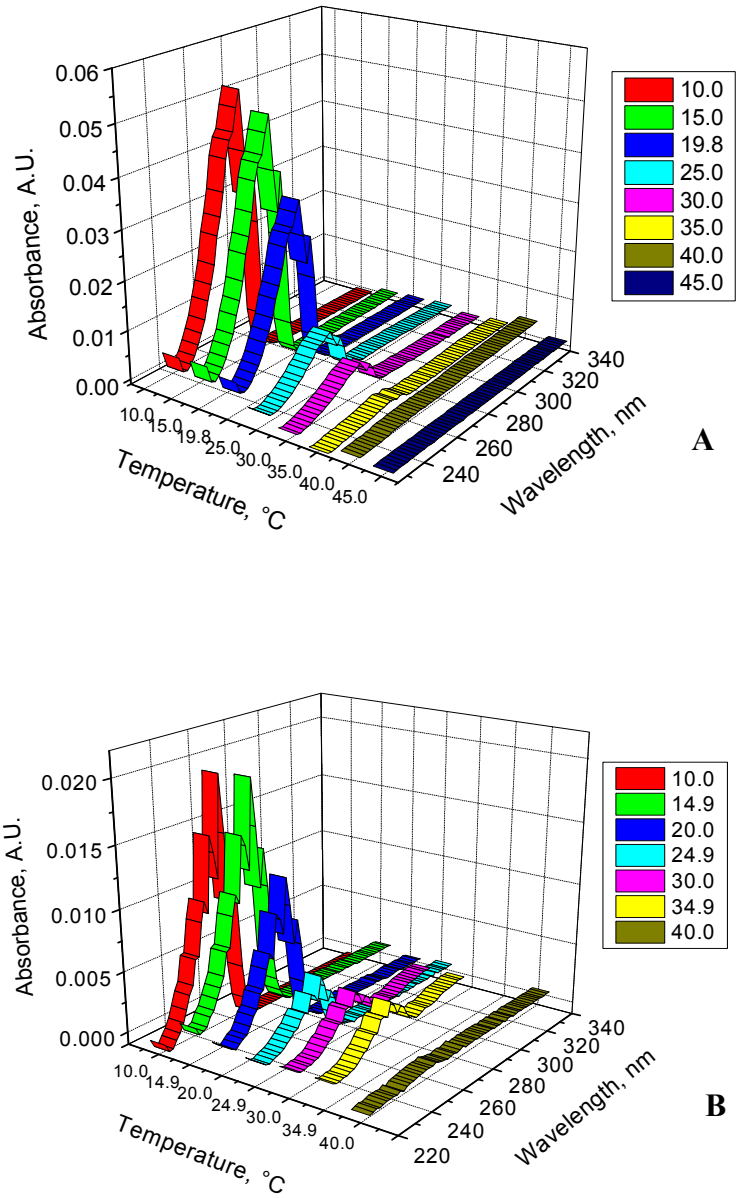

Figure 3.3. UV absorption at the air-water interface as a function of temperature for toluene (**A**) and benzene (**B**).

At this point it is clear that even though the common accepted waiting time period is between 10 and 20 min, toluene and benzene can be detected at longer times exceeding 60 min. In order to clarify the effect of temperature on the evaporation process we decided to investigate this effect by heating the KSV trough to the desired temperature. Pure water subphase was used as blank for the absorption measurements and was measured for each temperature. This was followed by the spreading of the same amount of toluene or benzene (50 μL) on the water subphase. Each of the measurements is taken after a waiting time period of about 10 min. The results obtained for toluene are shown in Figure 3.3A. A similar graph was obtained for benzene (Figure 3.3B).

In order to investigate the dependence on temperature for both toluene and benzene, the peak maxima (262 and 254 nm, respectively) are plotted as a function of temperature as shown in Figure 3.4.

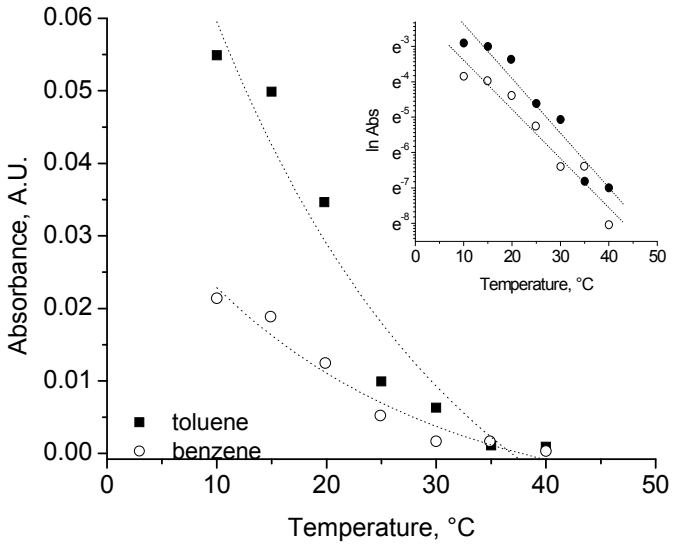

Figure 3.4. Absorbance at the air-water interface as a function of temperature for benzene (○) at 254 nm and toluene (■) at 262 nm. Inset: ln (Abs) vs. time showing the linear dependence. The waiting time period was kept constant at 10 min after spreading for each of the temperatures.

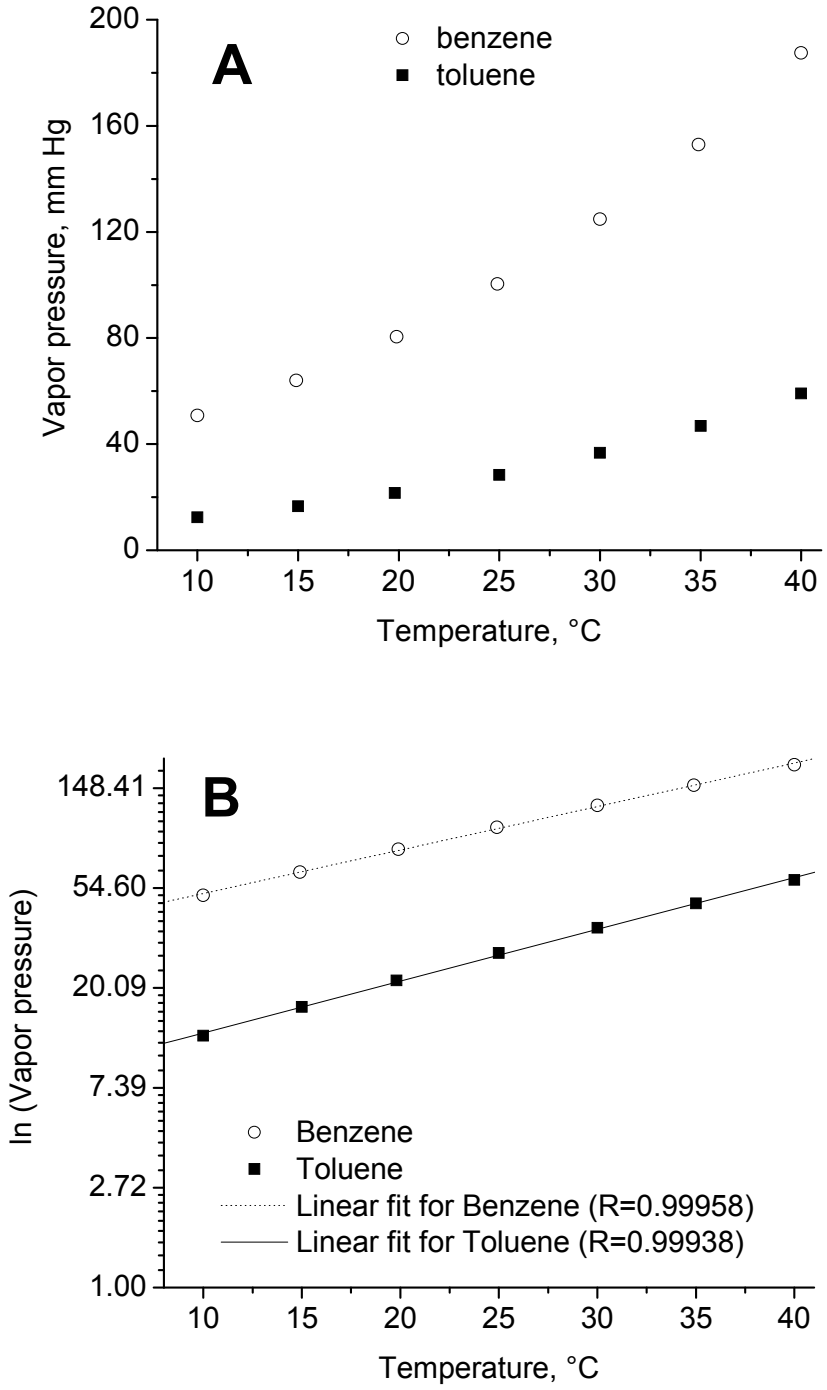

Figure 3.5. Calculated vapour pressures as a function of temperature for benzene (○) and toluene (■) (A) and ln (vapour pressure) as a function of temperature (B). As shown, the vapour pressure has a logarithmic dependence on the temperature.

In the author's view, this behavior can be explained based on the temperature dependence of the vapor pressure of toluene and benzene, respectively. As temperature is increasing the vapor pressure is increasing, which leads to an increase in the evaporation rate. This can be interpreted as a decrease in the amount of spreading solvent remaining at the air-water interface and therefore a decrease in its absorbance (smaller surface density of the spreading solvent at the interface). Figure 3.5 shows the temperature dependence of the vapor pressure for toluene and benzene, respectively calculated using Antoine's equation[41]). The vapor pressures were calculated using the online calculators available for both toluene[42] and benzene.[43]

To test this effect of the aromatic solvents in the presence of a Langmuir monolayer at the air-water interface an amphiphilic molecule was chosen, namely ethyl stearate. The reason for this choice was based on its solubility in toluene, benzene and chloroform. A 10^{-3} M solution of ethyl stearate was prepared in each of the three spreading solvents. A 50 μL solution was spread at the air-water interface. After a waiting time period of 10 min, the initial absorption spectrum was collected. After this measurement the monolayer was compressed and, for different surface pressures, the absorption spectra were collected. Figure 3.6 shows the surface pressure-area isotherms in three different solvents namely benzene, toluene and chloroform. As shown in Figure 3.6 the isotherms are virtually identical, within experimental error. This confirms that the aromatic spreading solvents used do not have a significant surface activity, but these measurements do not detect the presence of the spreading solvent at the air-water interface.

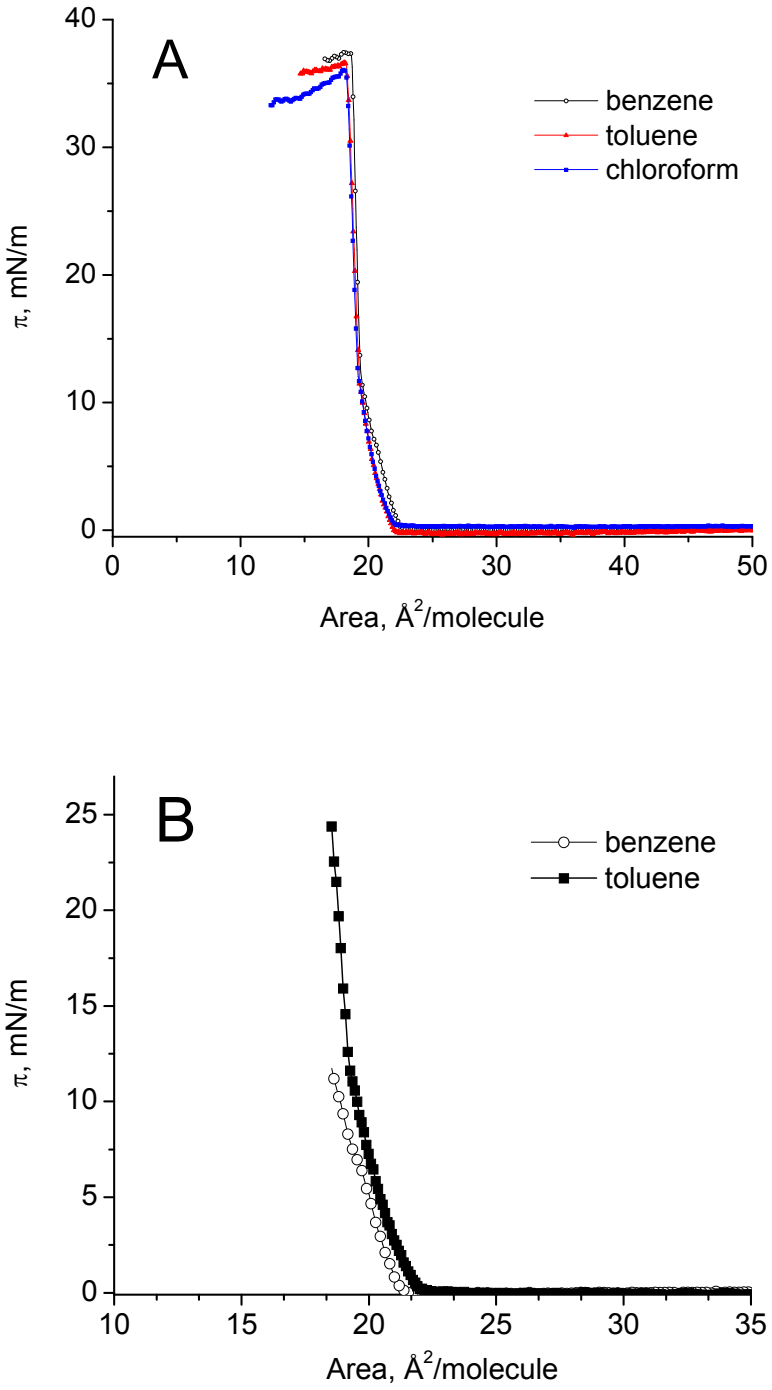

Figure 3.6. Surface pressure-area isotherms, up to the collapse surface pressure, for 10^{-3} M ethyl stearate in benzene, toluene and chloroform (spreading volume: 75 µL) (A) and surface pressure-area isotherms for 50 µL spread (B).

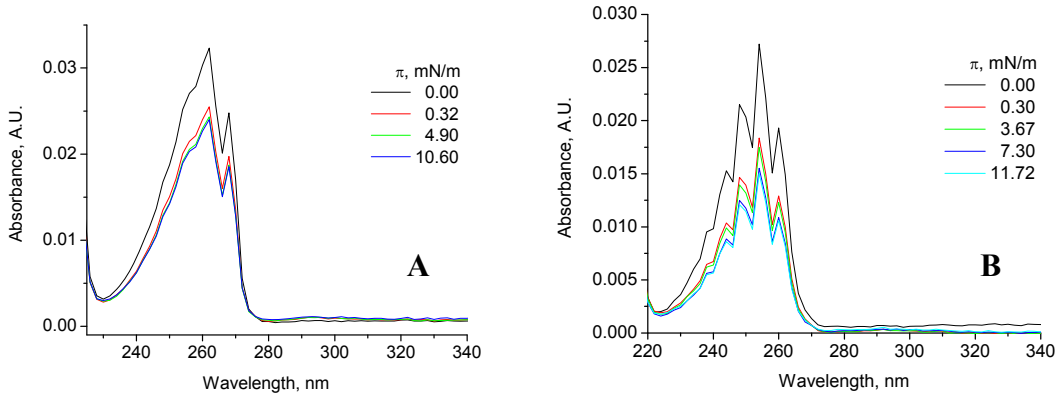

Figure 3.7. UV absorption spectra of 50 µL 10^{-3} M ethyl stearate in toluene (**A**) and benzene (**B**) spread at the air-water interface as a function of surface pressure.

After a waiting time period of 10 min, the initial absorption spectrum was collected. The monolayer was then compressed and, for different surface pressures, the absorption spectra were collected. The total time including the initial waiting period was about 30 min.

Figure 3.7A shows a plot of the measured absorbance as a function of surface pressure for toluene. Similar results were obtained using benzene as spreading solvent and the results are shown in Figure 3.7B. Briefly, the UV absorption was measured after an initial waiting time period of 10 min before compression (0 mN/m) and for different surface pressures during the compression of the monolayer. Even in the presence of the ethyl stearate, the solvent molecules are still present and their UV absorption is decreasing due to evaporation. In our view, the presence of the benzenoid bands with the vibrational fine structure can be explained by the behavior of the aromatic solvents at the air-water interface similar to a gas phase.[1] Toluene and benzene in gaseous phase or dissolved in cyclohexane in very small concentrations are known to show the vibrational fine structure of the benzenoid bands.[44] The UV data described on ethyl stearate are based on Figure

3.6B (50 μL ethyl stearate spreading solution in toluene and benzene, respectively). Figure 3.6A is included to show the complete surface pressure-area isotherms, including the Langmuir monolayer collapse using the three different spreading solvents.

3.3 Conclusions

It was shown that the aromatic spreading solvents commonly used at the air-water interface (toluene and benzene) are present on the water surface much longer than commonly expected. Ethyl stearate was chosen for its solubility in aromatic and non-aromatic solvents and does not have any significant absorption in the UV region. If amphiphiles containing an aromatic moiety are studied as Langmuir monolayers, they cannot be properly characterized if the absorption spectrum contains both the benzenoid bands from the aromatic moiety of the amphiphile and from the spreading solvent.[45] Another case where the aromatic solvent can interfere is the aggregate formation at the air-water interface involving solvent trapping. If a long waiting time period is assured, the bulk spreading solvent should evaporate, while the trapped solvent could be detected spectroscopically. The authors are aware that in some cases there is no other choice but to use these solvents. In this case, a longer waiting time period is recommended to assure that the solvent has no effect on the UV absorption of the amphiphilic compound under study.

Chapter 4. Interfacial Studies on UG8 Asphaltene

4.1 Background

Crude oil is represented by the main fractions called SARA (saturates, aromatics, resins and asphaltenes). The SARA classification is useful for providing a rough description of crude oils.

Asphaltenes are believed to be suspended as colloids in the crude oil consisting of nanometer-sized particles.[46] Each particle consists of one or more aromatic sheets of asphaltene monomers, with adsorbed resins acting as surfactants to stabilize the colloidal suspension. Under specific solvent conditions, resins desorb from the asphaltenes, leading to an increase in asphaltene aggregate size and eventually precipitation of large asphaltene aggregates.

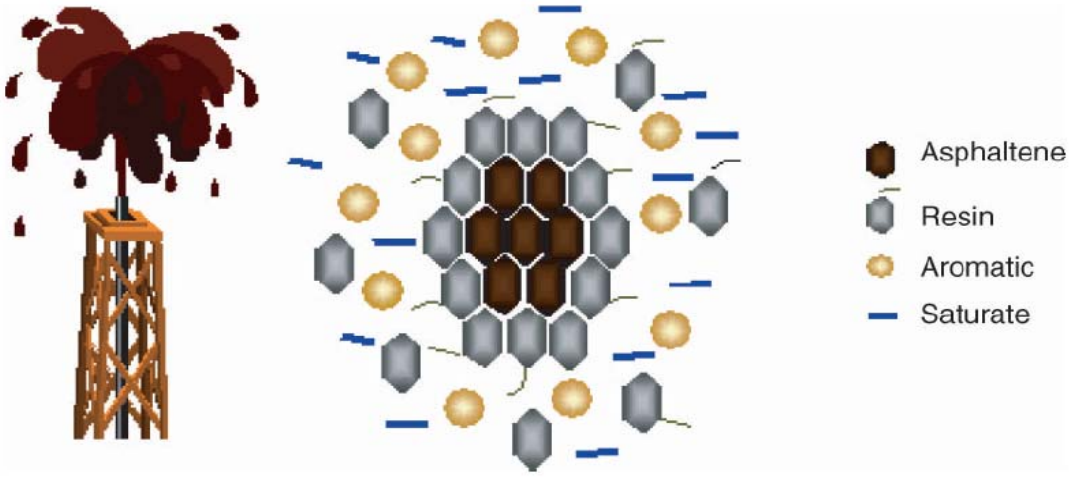

Figure 4.1. Simplified view of petroleum [*Asphaltanes, Heavy Oils, and Petroleomics, Edited by O. C. Mullins, E. Y. Sheu, A. Hammani and A. G. Marshall, Springer, 2007; A.Hammani and J. Ratulowski, Chapter 23, pp. 626]*.

The first definition of the asphaltene was proposed by Boussingault in 1836[47], and more recently, Shaw and coworkers[48] presented an operational definition of an asphaltene as a

material that (i) precipitates from crude oil when diluted 20:1 or more with solvents (n-pentane, n-heptane) but is soluble in toluene; (ii) can be filtered at 1μm; (iii) does not include contributions from resins and waxes. The toluene-soluble/n-heptane-insoluble fraction of crude oil, i.e. asphaltenes, characteristically exhibit fused ring aromaticity with polar heteroatom functionality. The application of X-ray Raman spectroscopy (XRRS) to the local structure of carbonaceous systems, such as asphaltenes, has shown that their structure is dominated by sextet carbon independently of asphaltene source.[49] This result corroborates the previous findings that petroleum asphaltenes consist primarily of polyaromatic systems with 4-10 fused rings.[50,51]

Figure 4.2. Main crude oil component, asphaltene, leading to pipe obstruction.

Asphaltene is the main component of a crude oil and its aggregation leads to pipe obstruction. Because of this fact, it is the main cause for spills caused by pipe bursts that lead to environmental issues. It is estimated that asphaltene causes a loss to the petroleum industry estimated to $250 million dollars per day. Because of these facts asphaltene was the topic of research for several decades.

In order to address the function of asphaltene, its molecular structure needs to be understood.In recent years, much of the controversy regarding asphaltene's molecular weight was resolved using new mass spectral techniques and other analytical techniques such as fluorescence depolarization measurements, which have the necessary resolution required for the complex field of asphaltene research.

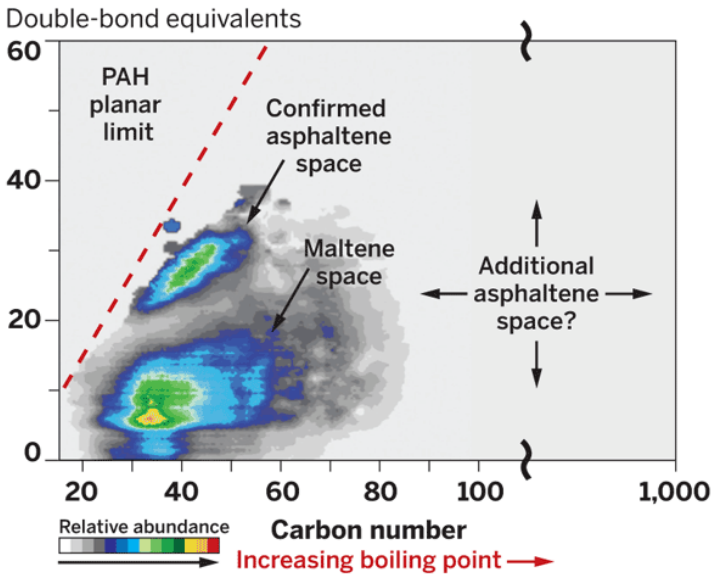

Figure 4.3. Double-bond equivalents (DBE, rings plus double bonds) versus carbon number of compounds containing a single sulfur atom from all fractions of a Middle Eastern crude oil sample.

Petroleum components occupy all the composition space[52,53] between the polycyclic aromatic hydrocarbon (PAH) planar limit and the aliphatic limit (Figure 4.3) which is, where DBE = 0, along the horizontal axis.

The factors that determine whether a newly precipitated solid phase actually forms a deposit, which then grows and occludes pipelines and production facilities, involve not only the oil chemistry but are compounded by interfacial interactions of the organics with oil, water, gas, mineral, and metal surfaces.

Asphaltenes are known to be surface active, as its main component belongs to hydrocarbons. Based on this fact, any questions related to the interfacial science of crude oils will most likely have a component that involves asphaltenes. Issues related to emulsion, stability, deposition or wettability involve interfaces.

4.2 Influence of Spreading Solvents: Toluene and Benzene

4.2.1 Background

This research focuses on a systematic investigation of UG8 asphaltene Langmuir films at the air-water interface using toluene as the spreading solvent. From the surface pressure-area isotherms it was concluded that small size aggregates are spread on the water surface and the compression of the film leads to formation of large aggregates. Our methods provide a stringent test and confirmation for the formation of corresponding asphaltene nanoaggregates that have recently been proposed for bulk solutions. These results were confirmed by compression-decompression isotherms, Brewster Angle Microscopy and p-polarized Infrared Reflection-Absorption Spectroscopy. The transfer of a single layer using both the Langmuir-Schaefer and Langmuir-Blodgett deposition techniques shows different aggregate shapes depending on the technique used as imaged using Atomic Force Microscopy. The films reveal the existence of nanoaggregates spread on the water surface that coexist with large aggregates formed during compression. For the nanoaggregate, the thickness of the Langmuir-Schaefer and Langmuir-Blodgett films determined by AFM is consistent with small aggregation numbers of nanoaggregates determined by Langmuir film compression. In addition to these findings the spreading solvent, toluene, was found to be trapped within the aggregates as confirmed by *in situ*

UV-vis spectroscopy at the air-water interface. This result was possible only after waiting a time period of 1 h to allow the complete evaporation of the spreading solvent. This is the only study that reveals the presence of the *in situ* toluene within the UG8 aggregates directly at the air-water interface.

Asphaltenes constitute a class of polyaromatic hydrocarbons known to be soluble in toluene and insoluble in n-heptane.[54,55] In the latest years the research showed an increase of the focus on asphaltenes. Current research involves the study of the asphaltenes in solution and films at the oil-water[56-60] and air-water interface.[34,61-64] The entire research aims at elucidating the actual structure of asphaltenes, which led to a controversy[65] in the literature regarding the actual molecular weight. Some groups suggest a molecular weight in the range of 8000-10000 Da while others consider the molecular weight between 500-1000 Da with a higher population at 750 Da.[66-72] Techniques based on molecular diffusion confirming the later finding include fluorescence correlation and depolarization spectroscopy and mass spectrometry (MS).[66-72] Measurements using laser desorption ionization (LDI) and other mass spectral techniques also confirm this result.[73-76] This result is generally accepted over the last decade with some exceptions. The elucidation of the molecular weight is extremely important when interpreting Langmuir film characteristics at the air-water interface. Keeping this in mind, the authors are using a molecular weight of 750 Da throughout the measurements and data interpretation. Another key issue is the use of the proper spreading solvent. Throughout the literature the solvent of choice is toluene. It will be shown that the use of toluene as a spreading solvent involves some key factors to be taken into account, e.g. toluene evaporation time.[77] This factor is fundamental to the

elucidation of the molecular species present in the UG8 asphaltene structure that can be studied using UV-vis spectroscopy. Typical absorbance spectra are shown in a region between 300 and 800 nm when the absorbance of asphaltenes is studied in solution. But 300 nm is the UV cut-off wavelength for toluene. Therefore, species absorbing at lower wavelengths cannot be detected. Even though toluene was used in this study we found the proper experimental conditions to obtain the UG8 asphaltene Langmuir film UV-vis spectrum. In this research we studied the interfacial properties of the UG8 asphaltene using techniques that include surface pressure-area isotherms, compression-decompression cycles, UV-vis at the air-water interface, infrared reflection-absorption spectroscopy (IRRAS), Brewster angle microscopy (BAM) and atomic force microscopy (AFM) for the Langmuir film transferred on solid support. It will be shown that some of the results are in disagreement with previously reported data on the possible asphaltene structure. In particular, it is shown that neither single or double aromatic ring systems are present in the UG8 asphaltene structure or their percentage is very low. Other data herein are complementary to the literature on the toluene trapping within the asphaltene aggregates.

To assure a repulsion dominant regime[78], the cantilever frequency was set at 159.75 kHz to image the Langmuir-Schaefer and Langmuir-Blodgett films of UG8 asphaltene transferred onto highly oriented pyrolytic graphite (HOPG) for AFM imaging.

4.2.2 Surface Chemistry

4.2.2.1 Surface Pressure-Area Isotherms

All measurements were performed with freshly prepared solutions. The surface pressure-area isotherm shown in Figure 4.4 was obtained by spreading 50 μL of 1 mg/mL

UG8 asphaltene in toluene on a Langmuir trough with an area of 225 cm^2. The apparent limiting molecular area, obtained from the extrapolation on the x-axis of the linear portion of the plot, is 19 ± 2 $Å^2$/molecule. This result is reproducible even if spreading volumes are varied between 35 and 50 μL. Taking into account that stearic acid (CH_3-$(CH_2)_{16}$-COOH), a C_{17} hydrocarbon chain with a small polar moiety (a carboxylic group) having a molecular weight of 284.48 Da gives a limiting molecular area of 21 $Å^2$/molecule it can be concluded that the UG8 asphaltene, with a higher molecular area (750 Da), more than one hydrocarbon chain and fused benzene rings[2] must be in an aggregated state. This can be explained by the fact that a molecule in monomeric form (i.e., UG8 asphaltene) with a large molecular weight and multiple hydrocarbon chains takes a much larger space. For example, if the molecule has five hydrocarbon chains it should have a limiting molecular area of about 100 $Å^2$/molecule (this is obtained by multiplying the number of hydrocarbon chains with the area obtained for stearic acid). The calculated result (100 $Å^2$/molecule) does not take into account the size of the polyaromatic core. If taken into account, the molecular area should be even higher. For this reason, the term *apparent limiting molecular area* is used.

Based on this example, it is clear that asphaltene must be aggregated. In some cases (Figure 4.5) a slightly higher apparent limiting molecular area is obtained (24 ± 2 $Å^2$/molecule). For a rough idea of the aggregation number, the asphaltene molecular size is on order 15 Å in linear dimension.[66-71] For a molecular dispersion, the area per molecule would be roughly 10 times bigger than what is measured. Consequently, aggregation numbers of about 10 are predicted from this data. Indeed, this is close to asphaltene aggregation numbers as measured by many methods.[79]

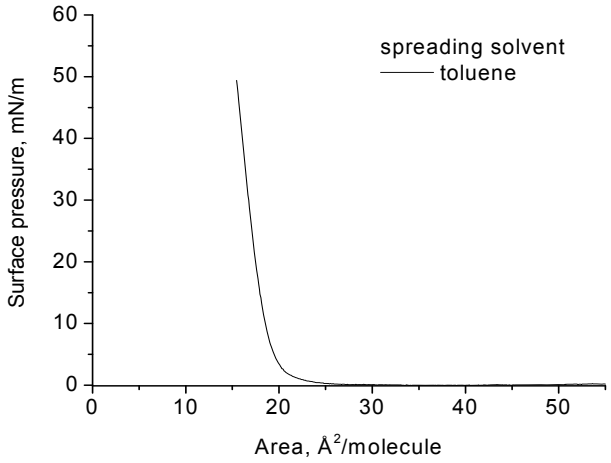

Figure 4.4. Surface pressure−area isotherm for UG8 asphaltene spread at the air−water interface from toluene.

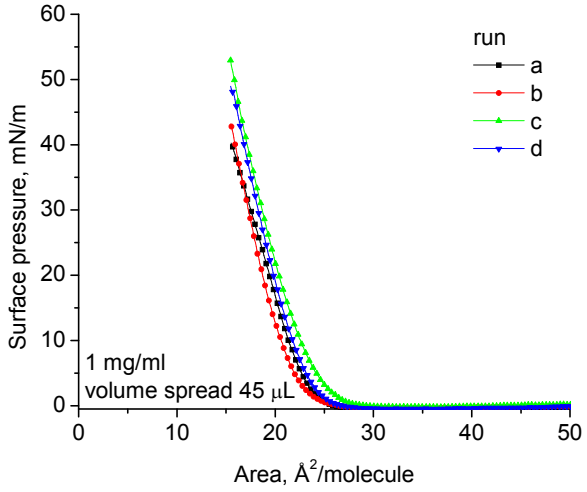

Figure 4.5. Surface pressure-area isotherms for UG8 asphaltene spread from a distilled toluene solution showing slightly a different apparent molecular area.

4.2.2.2 Compression-Decompression Isotherm

Using compression-decompression cycles of the Langmuir film, it was found that the asphaltene does aggregate at the air-water interface. The author chose a target surface pressure of 30 mN/m. As it can be seen from Figure 4.6, the compression isotherm is similar to the one shown in Figure 4.4. The decompression of the Langmuir film reveals a

hysteresis effect which is attributed to large aggregate formation as will be demonstrated from BAM and AFM data. Interestingly, the surface pressure does not decrease to 0 mN/m in the first compression-decompression cycle, or in the second one. In the second cycle, during decompression, a sudden drop in the surface pressure occurs.

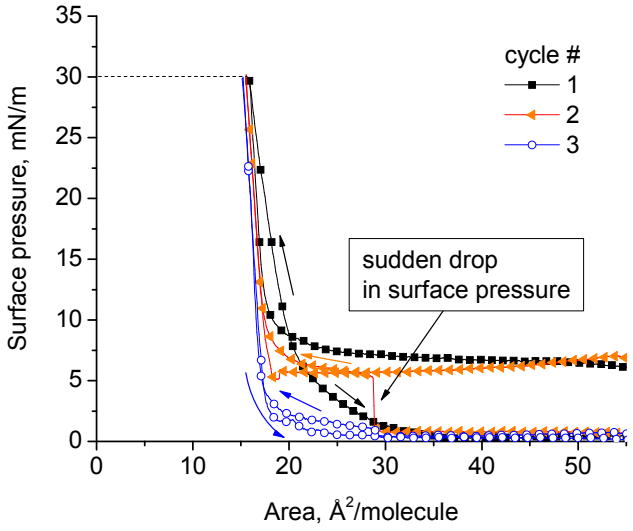

Figure 4.6. Compression−decompression isotherms cycles for UG8 asphaltene at the air−water interface spread from a toluene solution with a target surface pressure of 30 mN/m.

The lack of decrease in the surface pressure can be explained by the formation of rigid aggregates that do not readily expand on the water surface, and the aggregate is in close contact with the Wilhelmy plate. This result is not always reproducible as shown in Figure 4.7. Also, the sudden drop in the surface pressure lacks reproducibility. The sudden drop in the surface pressure during decompression is attributed to the formation of cracks and is in agreement with previously reported data in the literature.[63]

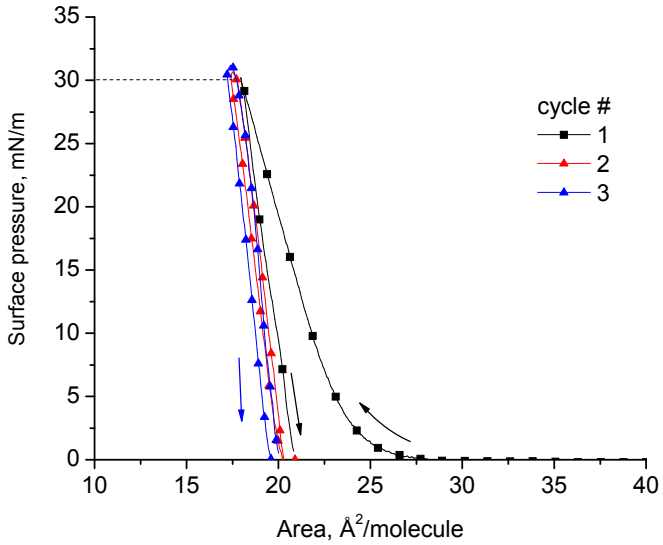

Figure 4.7. Compression-decompression cycles for UG8 asphaltene Langmuir film spread from freshly distilled toluene solution.

4.2.2.3 In situ UV-vis Spectroscopy

Further investigation of the UG8 Langmuir film was carried out using *in situ* UV-vis spectroscopy using an HP diode array spectrophotometer.

In the UV-vis data reported in the literature[62] all the spectra are presented from 300 or 350 to 800 nm. A typical UG8 asphaltene UV-vis spectrum obtained in solution is shown in Figure 4.8. There has been a debate about the relative contribution of single-ring and two-ring aromatics in asphaltenes. One spectroscopy study claimed this population is very small.[80] Nevertheless, these studies did not determine the optical absorption of asphaltenes at the absorption band of single ring aromatics due to solvent interference. Here, in the Langmuir film, solvent interference can be managed.

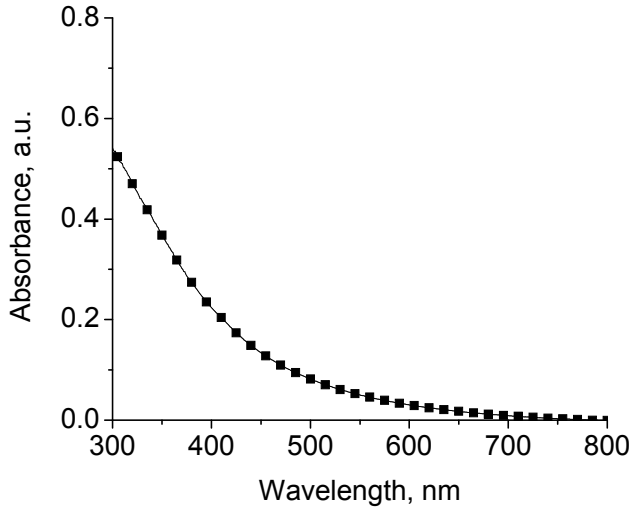

Figure 4.8. UV-vis absorption spectrum of 10^{-4} M UG8 asphaltene in toluene measured in solution using a 0.2 cm optical path quartz cuvette.

In Figure 4.9A, the UV-vis spectra of UG8 asphaltene are presented as a function of surface pressure after a waiting time period of 15 min under which the solvent (toluene) should evaporate. In Figure 4.9B, the UV-vis spectra are shown as a function of surface after an initial waiting time after spreading of 1 h. As seen in this figure most of the toluene bands disappear. As it can be seen, the typical vibronic absorbance spectrum of toluene appears and covers all the features related to asphaltene. A similar result to Figure 4.9A is obtained if, instead of toluene (Figure 4.10A), benzene is used as spreading solvent (Figure 4.10B) showing the vibronic bands characteristic of benzene. We have shown previously[77], the importance of the waiting time period in Langmuir monolayer studies if aromatic solvents are used. In brief, for a constant temperature of 20°C a waiting time period of about 1 h was recommended to ensure that all toluene is evaporated, as measured using *in situ* UV-vis spectroscopy. The alternative was to heat

the water trough up to a temperature of 40°C which can speed up the evaporation process, but aggregation could be influenced by the temperature.

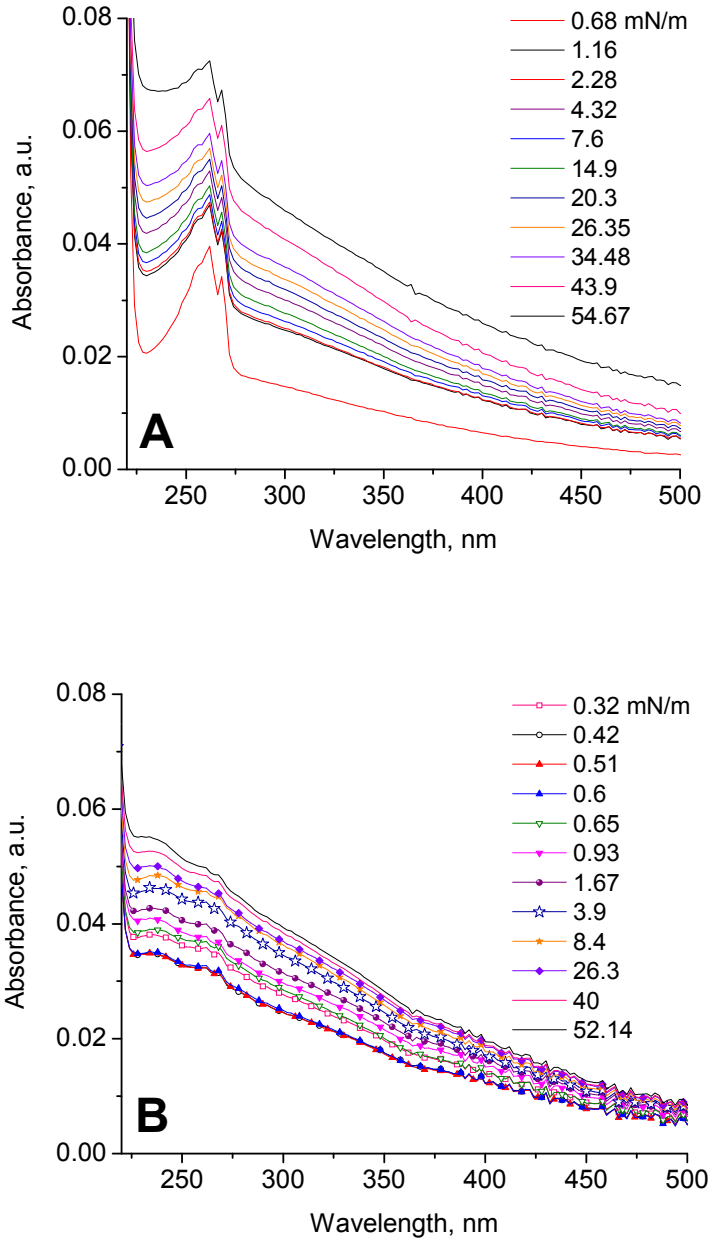

Figure 4.9. UV−vis spectra at the air−water interface for 1 mg/mL UG8 asphaltene in toluene after 15 min (A) and 1 h (B) waiting time period before compression.

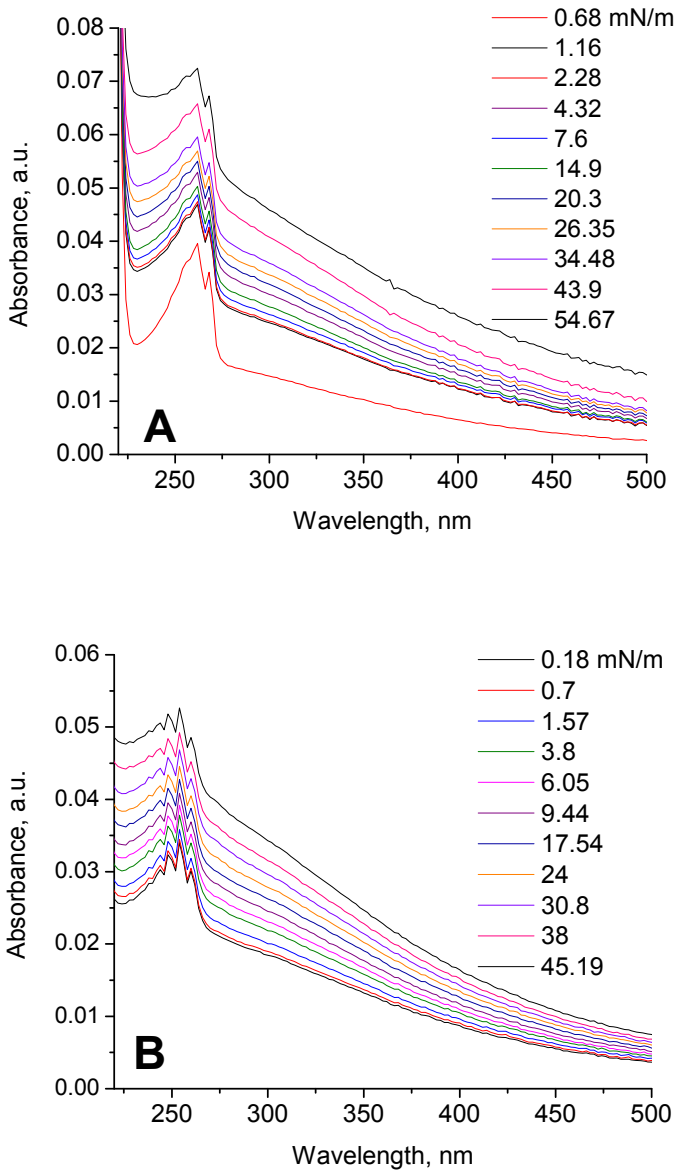

Figure 4.10. Comparison between the *in situ* UV-vis absorption spectra of UG8 asphaltene with a waiting time period of 15 min before compression using toluene (A) and benzene (B) as spreading solvents.

Based on these experimental conditions, the author preferred a waiting time period of 1 h before the film compression to ensure complete evaporation of the spreading solvent under an ambient temperature of 20.0 ± 0.5°C. The effect of temperature on the aggregation process was not investigated in the present work.

As shown in Figure 4.9B, most of the toluene absorbance disappeared as the solvent evaporated, which in turn revealed the absorbance spectrum of UG8 asphaltene. By far, the most prominent feature of the spectra is that they exhibit an increasing absorption at shorter wavelength, almost without any absorption peaks. This is consistent with observations made at longer wavelengths.[79] In general, very small aromatic ring systems have discrete separated bands, in contrast to the overlapping spectra of large PAHs (polycyclic aromatic hydrocarbons). The direct implication from our short wavelength asphaltene spectra is that the asphaltenes have a small fraction of small aromatic ring systems (e.g. one ring systems, two ring systems). This same conclusion was also obtained previously by measuring short wavelength fluorescence spectra;[80] the optical absorption measurements here are more robust than fluorescence emission measurements in terms of molecular architecture. The spectra (Figure 4.9B) contain a shoulder located at 230 nm, which is typical of some polycyclic aromatic hydrocarbons. The second feature of the spectra is the presence of small toluene-like absorption bands. This can be explained in two ways. First, the asphaltene could have in its structure isolated benzene rings in addition to the fused rings sufficient to account for this absorption. The second explanation could be that during aggregation of asphaltene in the toluene solution, solvent trapping occurs. The following supports the second explanation by direct spectral analysis.

Based on the UV-vis data, it can be concluded that the absorbance bands in Figure 4.9B do belong to toluene, and therefore, toluene must be trapped in the aggregates spread at the air-water interface.[81] In particular, this toluene band is absent from asphaltene spectra when chloroform is the spreading solvent, proving this toluene band

here is entrained solvent.[81] This interpretation is supported by previously published results finding trapped solvent in asphaltene aggregates using small-angle neutron scattering (SANS) data.[82] The measurements performed here show that the trapped toluene remains even after exposure of the surface film to air for one hour. The actual values for the absorbance at a given surface pressure cannot be entirely reproduced, as asphaltene is aggregated, but the overall absorbance range for UG8 asphaltene spread from toluene is always between 0.035 and 0.060. To ensure that the Langmuir film is stable at the air-water interface, we performed the stability measurements as a function of time at constant surface pressure while monitoring the change in the area as a function of time (Figure 4.8A) to ensure that no molecules are lost in the subphase. A small decrease in the molecular area over a long time period while keeping the surface pressure constant would mean that the film is stable. On the same token, a large decrease in the molecular area in a short period of time means the film is not stable. The reason for keeping the surface pressure constant and monitoring the area as a function of time (Figure 4.11A) is related to the deposition of the UG8 asphaltene Langmuir film. To warrant a good transfer onto the solid substrate the surface pressure is therefore kept constant during both the Langmuir-Schaefer and Langmuir-Blodgett depositions. As shown in Figure 4.11A the decrease in the area for a constant surface pressure of 30 mN/m is negligible; therefore, the UG8 asphaltene forms a stable Langmuir film. But the surface pressure-area isotherms are obtained through a dynamic process that is the compression. If the barriers are stopped, the relaxation of the surface pressure will occur towards an equilibrium value that is always smaller than the initial surface pressure at which the

barriers were stopped. Figure 4.11B shows the behaviour of the surface pressure as a function of time for a constant area when the molecular area was set 15 Å^2/molecule.

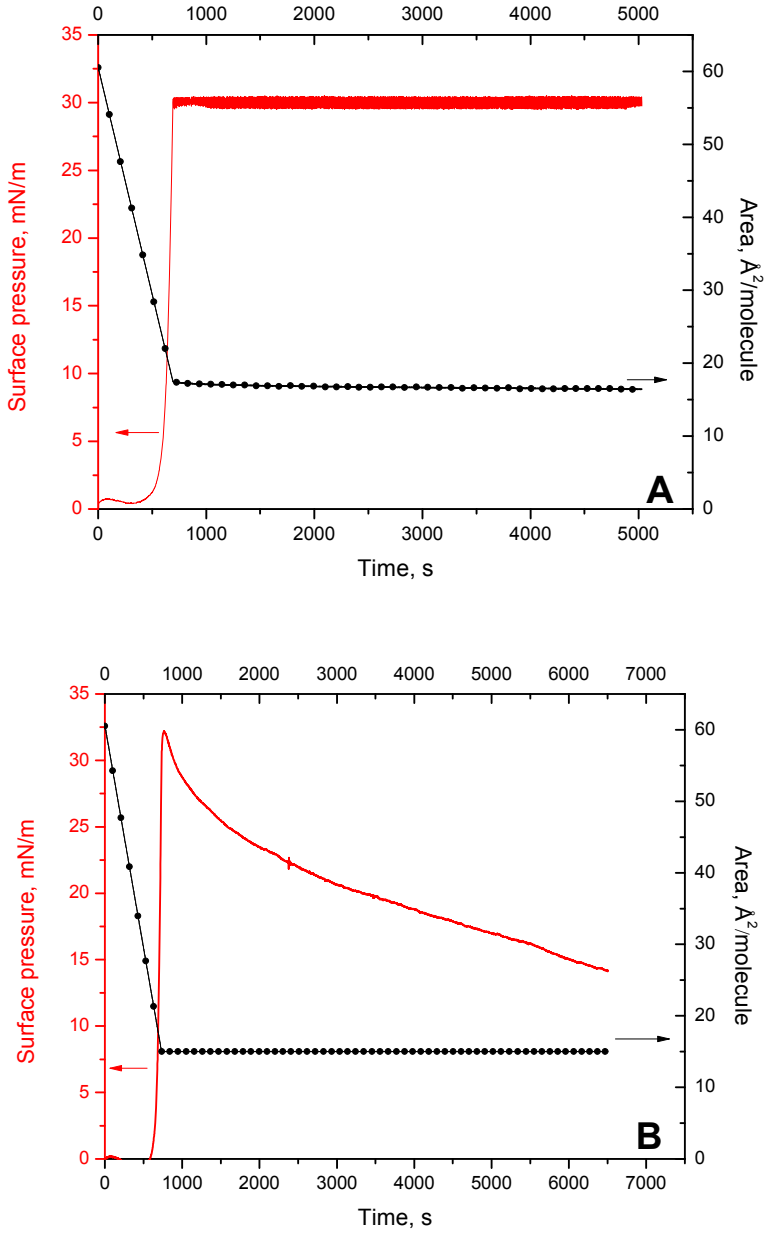

Figure 4.11. Stability for asphaltene Langmuir film spread from freshly distilled toluene at constant surface pressure (30 mN/m, —) and measured area (-●-) vs. time (A); Relaxation surface pressure after target (32 mN/m) is reached: constant area (15 Å^2/molecule, -●-), and surface pressure relaxation (—) vs. time (B).

4.2.2.4 Infrared Spectroscopy

The next method used for the investigation of the UG8 asphaltene Langmuir film was p-polarized IRRAS. The IRRAS measurements took about 45 min. We have shown so far that the apparent limiting molecular area, compression-decompression isotherms and the *in situ* UV-vis spectra suggest that aggregates are spread but also formed during compression of the asphaltene Langmuir film. The use of p-polarised IRRAS could shed more light onto the aggregation process by following the position of both the symmetrical and asymmetrical C-H stretching IR bands that can bring information on whether the hydrocarbon chains from asphaltene are loose or packed. Before performing the IRRAS measurements, let us take a look at the IR spectrum of the asphaltene in solution.

4.2.2.4.1 Bio-ATR Infrared Spectroscopy

The infrared spectra in solution were measured using the Bio-ATR cell II. As shown in Figure 4.12A, when the IR spectrum of UG8 asphaltene (1mg/mL) is compared to pure toluene, no differences can be seen, as both toluene and asphaltene have aromatic rings (3100-3000 cm^{-1}) and hydrocarbon chains (3000-2800 cm^{-1}). In order to visualize the IR bands of UG8 asphaltene, the author decided to use deuterated toluene. By using deuterated toluene, the solvent IR bands will shift to much lower wavenumbers, because the force constant of the C-D vibration is different compared to that of C-H, present in toluene.

The results using deuterated toluene solution are presented in Figure 4.12B. The IR bands of deuterated toluene are not present anymore between 3100-2800 cm^{-1}; therefore, for deuterated toluene, what we observe in the graph for this region is noise.

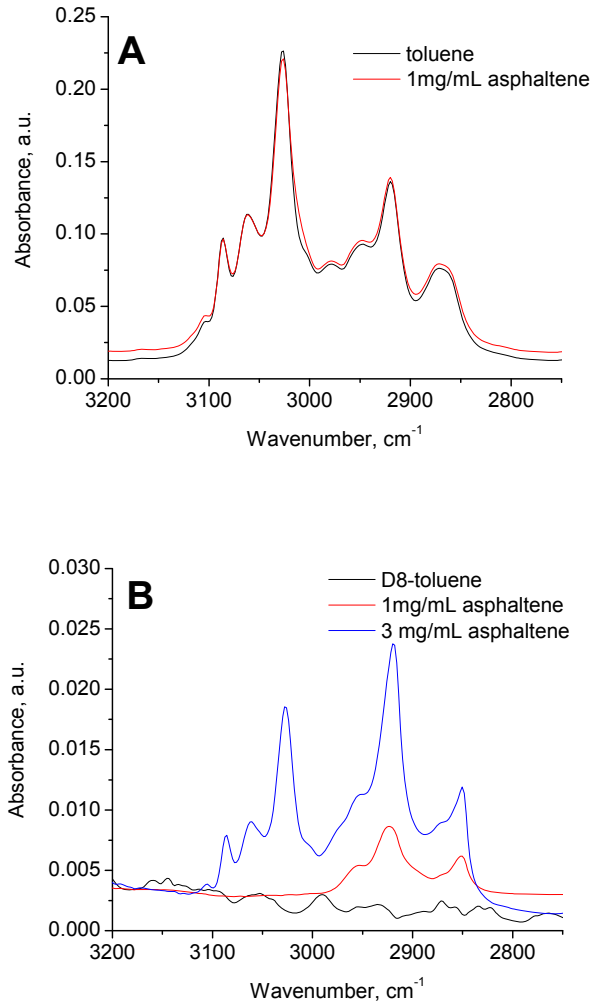

Figure 4.12. Bio-ATR FTIR spectra of UG8 asphaltene in toluene (A) and deuterated toluene (B).

When a concentration of 1 mg/mL UG8 asphaltene in deuterated toluene is used, the only result obtained is related to the stretching bands of aliphatic C-H in asphaltene (aliphatic C-H is known to be a stronger signal compared to the aromatic C-H); also, the concentration used did not ensure a high enough concentration of the asphaltene molecules (aggregates) on top of the ATR crystal. We have repeated the measurements using 3 mg/mL solution of UG8 asphaltene in deuterated toluene. In this case (Figure

4.12B, blue line), the asphaltene concentration was high enough to permit the determination of both aromatic and aliphatic C-H stretching bands of UG8 asphaltene. Based on the Bio-ATR results, we hypothesized that measuring the IRRAS spectra for a Langmuir film of the asphaltene the detection of the aromatic bands of the alphaltene will not be possible, knowing that all Langmuir film measurements are performed using 1 mg/mL UG8 asphaltene.

4.2.2.4.2 Infrared Reflection-Absorption Spectroscopy

Indeed, by performing p-polarized IRRAS at the air-water interface for 1mg/mL UG8 asphaltene in deuterated toluene we were able to obtain the same features as with Bio-ATR FITR for 1mg/mL solution but with a smaller intensity, as Bio-ATR uses un-polarized IR light, as will be shown below.

Initially, we have compressed the asphaltene Langmuir film to a surface pressure of 40 mN/m, and we performed p-polarized IRRAS for different incident angles (Figure 4.13A). It is known that in p-polarized IRRAS the vibration bands parallel to the water surface appear negative at angles below the Brewster angle of water, which is 53.12°. For incident angles larger than the Brewster angle, the bands become positive and at the Brewster angle the signal is nil.[15,83] Due to this fact the IRRAS spectra for angles close to the Brewster angle are not presented. As shown in Figure 4.13A, the intensity of the bands is increasing towards the Brewster angle, for the negative bands, while after the Brewster angle the intensity is decreasing with the increase in the incident angle. The bands observed are typical of symmetric and asymmetric C-H stretching (2850 and 2920 cm^{-1}) and the terminal $–CH_3$ group from the hydrocarbon chains at 2960 cm^{-1}.

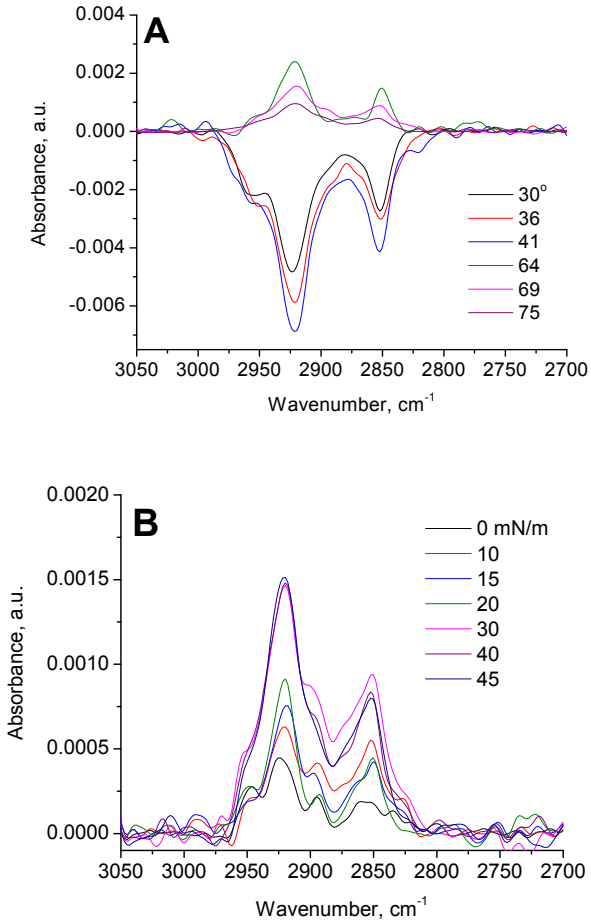

Figure 4.13. Infrared reflection−absorption spectroscopy at the air−water interface of 1 mg/mL UG8 asphaltene in deuterated toluene as a function of incident angle for a surface pressure of 40 mN/m (A) and as a function of surface pressure for a fixed incident angle of 69° (B).

Figure 4.13B shows the increase in the band intensities with the surface pressure at a fixed incident angle of 69°, which is a consequence of the increased molecular density at the interface during compression. Interestingly enough, while we do observe the C-H stretching, both symmetric and asymmetric, and the terminal methyl group, the position of the bands does not change. Usually, during compression the symmetric and asymmetric C-H stretching bands are located at higher wavenumbers (up to 10 cm^{-1}) and shift, upon compression, to 2850 and 2920 cm^{-1}, for the symmetric and asymmetric

stretch, respectively, when the hydrocarbon chains adopt the all-trans conformation. The fact that the IR band positions do not change is direct proof that much of the UG8 asphaltene is already aggregated when it is spread on the water surface. Our data related to the alkyl chains is very much in the line of other works where amphiphilic molecules are spread on the water surface where the hydrophobic chains adopt a rather vertical orientation[15] and not parallel[15,83] to the water surface. Based on this data and the lack of shift upon compression led us to propose a model for the alkyl chain interdigitation of the nanoaggregates.

4.2.2.5 Brewster Angle Microscopy

If our interpretation is correct, we should be able to visualize the aggregates. For this purpose, Brewster Angle Microscopy (BAM) was employed. In brief, the measurements were performed using a 53.15° incident angle, which is known to be the value for the Brewster angle of pure water, basically the angle for which the intensity of the reflected polarized light is minimal. Due to this reason the presence of a film, domain or aggregate should appear as a bright region (the presence of the film changes the refractive index of the interface compared to the one of pure water), compared to the dark (black) region represented by water. The micrographs obtained are shown in Figure 4.11. The *left column* shows the micrographs obtained as a function of the surface pressure during the compression of the asphaltene Langmuir film. Some structures can be seen at 0 mN/m. Upon compression, substantial aggregation takes place that is translated in the appearance of domains. Further compression to higher surface pressures of 10 and 30 mN/m, respectively, leads to the increase in the size of the domains that are formed, and eventually a more homogeneous film (less dark spots observed) appears by further

compression when the domains are brought in contact. To investigate if the structures that are formed are domains or aggregates, we acquired the BAM micrographs during the decompression of the Langmuir film. This was done under the assumption that if domains are formed during compression, by performing a decompression isotherm the domains should disappear or at least slowly relax to a more uniform structure. Domains can be formed during compression, but in the compression-decompression cycles, they could appear during compression and disappear during decompression, their behavior being reversible. This effect is visualized as a small hysteresis in the compression-decompression isotherm. On the other hand, if aggregates are formed, we would expect the structures to remain the same as formed during compression, and with decompression, only the spatial distance between these aggregates to increase, as the aggregates will have a larger space to float at the air-water interface and a great hysteresis effect appears during compression-decompression cycles. The results obtained during decompression of the Langmuir film are shown in Figure 4.14 *right column*. Indeed, what can be observed from the decompression BAM micrographs are the aggregates that were formed during the monolayer compression (surface pressure of 31 mN/m) remain the same, and slight spaces/cracks appear when the barriers are relaxed to produce a decrease in the surface pressure between 31 and 3 mN/m. Based on these results, we can clearly state that the structures formed during compression of the asphaltene Langmuir film are aggregates, and the data are consistent with the results previously reported.[64] Moreover, our interpretation of the compression-decompression cycles shown in Figure 4.4 is confirmed by the BAM data.

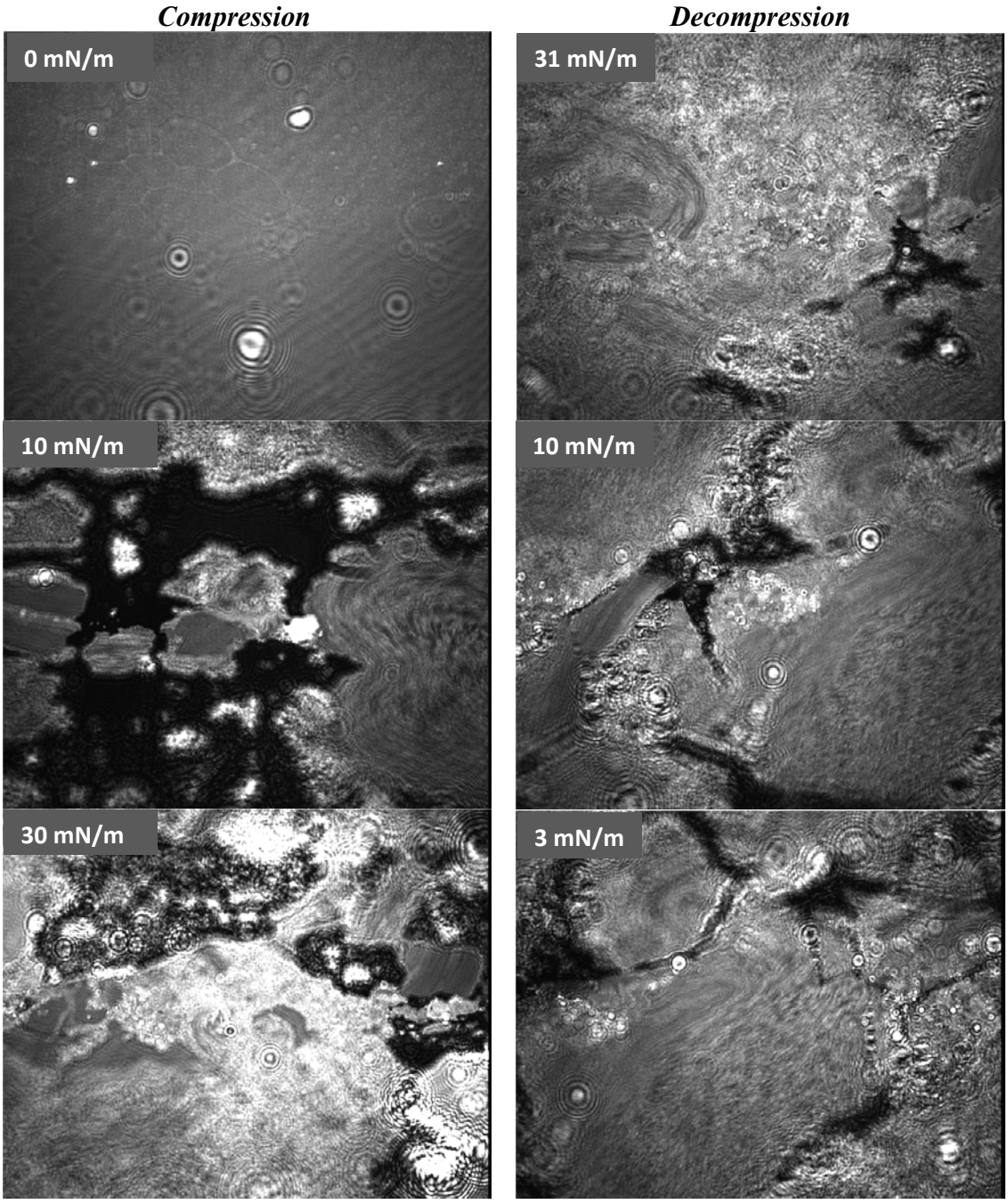

Figure 4.14. Brewster angle microscopy of UG8 asphaltene (1 mg/mL in toluene) Langmuir film during compression (left column) and decompression (right column) as a function of surface pressure (image size: 200 μm × 200 μm).

4.2.2.6 Atomic Force Microscopy

In order to image the aggregates with higher resolution, we have decided to perform AFM measurements. For this purpose, a single Langmuir film of asphaltene was transferred onto HOPG at a surface pressure of 15 mN/m from toluene solution using both Langmuir-Schaefer and Langmuir-Blodgett deposition techniques. HOPG is known to be hydrophobic and therefore is suitable to transfer the asphaltene film.

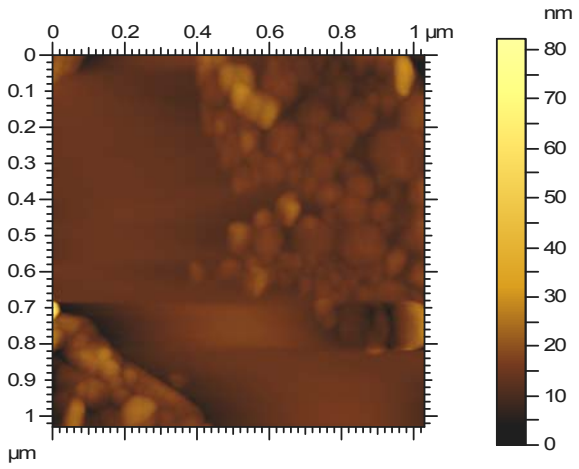

Figure 4.15. Intermittent-contact AFM micrograph of Langmuir−Schaefer film transferred onto HOPG substrate using toluene as spreading solvent. Image size (1 µm × 1 µm).

As it can be seen from Figures 4.15 (Langmuir – Schaefer) and Figure 4.16A (Langmuir – Blodgett), the shape of imaged aggregates is different depending on the deposition technique. Regardless of the deposition technique used it is clear that the aggregate size falls within the same range, i.e. 20 – 70 nm. In Figure 4.16B, a region is shown that on a larger scale does not show any aggregates present. In this case, it can be seen that the average thickness is about 1 – 2 nm, which corresponds closely to a nanoaggregated state of asphaltene in toluene for 1 mg/mL concentration, as previously reported in literature using other techniques (High-Q Ultrasonics) showing that the

critical nanoaggregate concentration (CNAC) is about 0.1 mg/mL.[84,85] The possible explanation for this effect is that initially small aggregates (about 1-2 nm) are formed in solution and this is what is spread at the air-water interface. Upon compression, the nanoaggregates interact and lead to the formation of large-sized aggregates as shown by BAM and AFM; see Figures 4.14, 4.15 and 4.16.

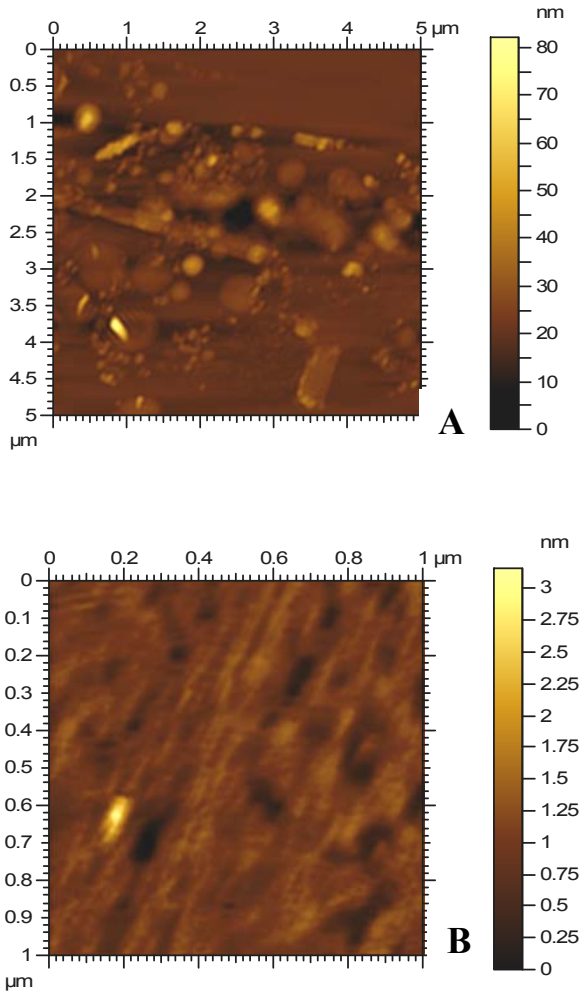

Figure 4.16. Intermittent-contact AFM micrographs of Langmuir−Blodgett film transferred on HOPG formed using toluene as spreading solvent, showing large aggregates (5 µm × 5 µm) (A) and small aggregates (1 µm × 1 µm) (B).

Therefore, during compression, the Langmuir film consists of a binary mixture of small and large aggregates. The compression-decompression isotherms also confirm this experimental result as well as the author's interpretation, because each compression-decompression cycle leads to the formation of large aggregates from the portion of the small aggregates still present in the Langmuir film. Using benzene as spreading solvent (Figure 4.17) and performing compression-decompression cycles (Figure 4.18A and 4.18B), the hysteresis effect that is observed is very similar to the one observed when toluene is used as a spreading solvent.

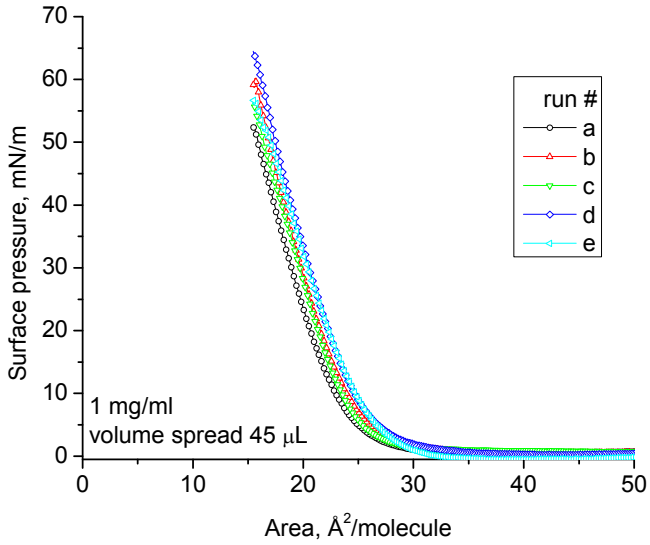

Figure 4.17. Surface pressure-area isotherms for UG8 asphaltene spread from benzene at the air-water interface.

The larger apparent limiting molecular area observed when benzene is used can be attributed to smaller aggregates formed compared to those in toluene, which can be correlated with the smaller absorbance values (Figure 4.10B vs. 4.10A). The second explanation for the smaller aggregates could be the lack of the methyl group in the benzene chemical structure but present in toluene. When benzene in trapped within the

nanoaggregates it would make sense that the overall size would be smaller since there is no methyl group present.

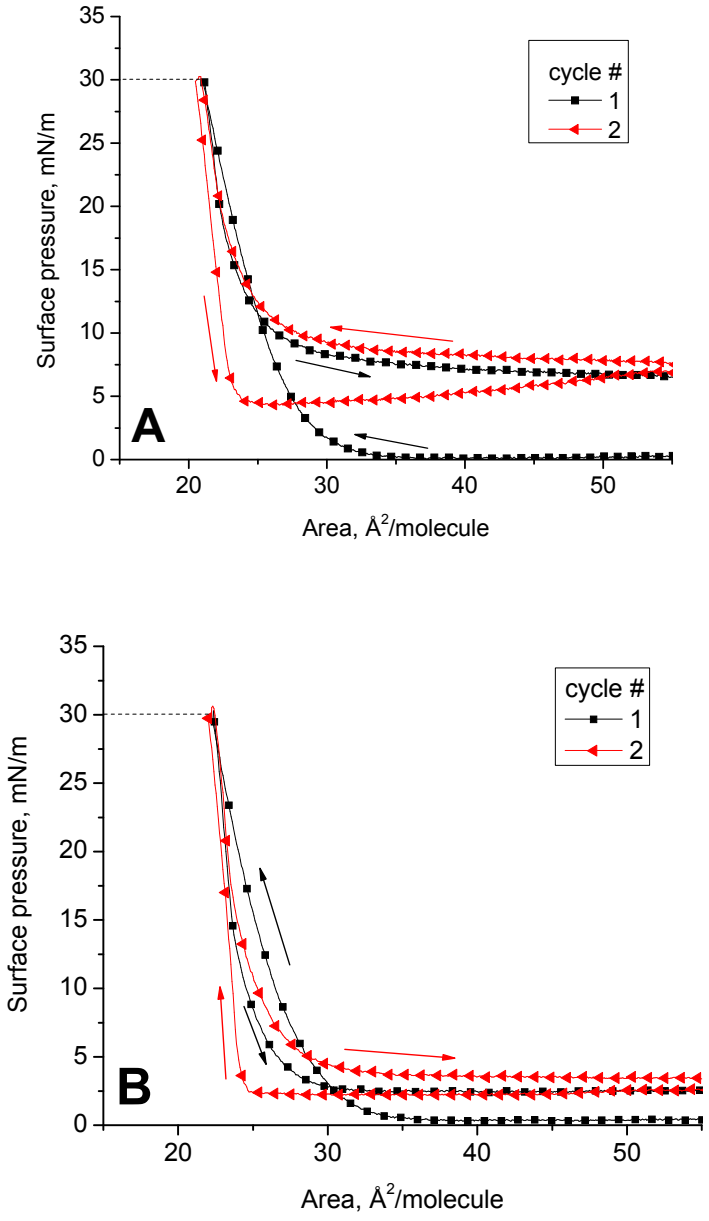

Figure 4.18. Compression-decompression isotherm cycles of UG8 asphaltene Langmuir film spread from benzene, run 1 (A) and at run 2 (B).

4.2.2.7 Implications on Molecular Architecture

The first model regarding the molecular architecture of asphaltenes was developed by Dr. T. F. Yen, and it is recognized as the so-called Yen model.[86] Over time, the model was continuously refined along with the development of the proper techniques[14-20] to better assess the molecular architecture and nowadays is adopted as the modified Yen model, with an outstanding review recently published.[79]

Our results can be correlated to the modified Yen model, based on the surface pressure-area isotherms (aggregation number), UV-vis (solvent trapping) and IRRAS spectroscopy (alkyl chain orientation), and AFM data (nanoaggregate height). The fact that we are using a concentration of 1 mg/mL of UG8 asphaltene in toluene, as explained before, falls well in the category of nanoagggregates that are formed in solution based on the previous results.[84,85] During compression, it was shown from UV-vis data that toluene is trapped within the aggregates, which also is confirmed by previous SANS results. We have also shown using BAM and AFM that the nanoaggregates are spread at the air-water interface from solution and their compression leads to significant aggregation.[81] Our IRRAS data show that the aliphatic C-H stretching from the asphaltene does not shift during compression and the IR bands position corresponds to a packed structure. Based on these experimental facts, the author concluded that the alkyl chains in nanoaggregates are subject to steric repulsion and consequently have restricted diffusion; a conclusion that has been obtained by NMR relaxation rate studies of asphaltenes.[87] The proposed orientation of the alkyl chains (a rather vertical orientation) comes from the fact that at a surface pressure of 40 mN/m, using deuterated toluene for different incident angles (Figure 4.13A), the nanoagregates do not show a random alkyl chain orientation. The

increase in surface pressure (Figure 4.13B) for the same incident angle shows an increase in the intensities of the IR bands due to compression, which means higher density of nanoaggregates per unit area. It can be seen from Figure 4.10B that the IRRAS spectrum acquired at 0 mN/m shows the band located at 2925 cm^{-1} shifts, for higher surface pressures, to 2920 cm^{-1} and remains unchanged throughout the measurements. This shift could be attributed to the interdigitation of the alkyl chains. In our view this results could be summarized as shown in Figure 4.19A, where in blue color trapped toluene is shown.

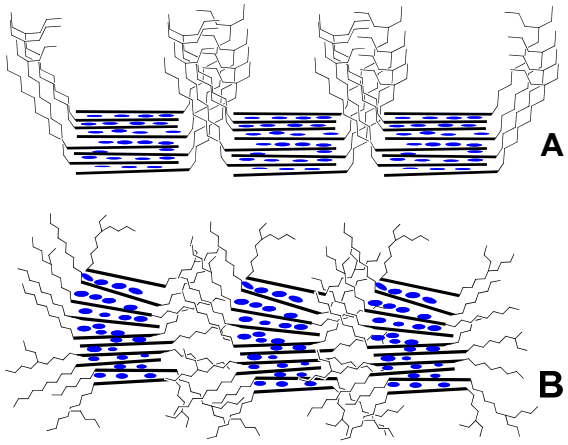

Figure 4.19. Proposed model of molecular architecture based on UG8 asphaltene Langmuir film (A). Proposed modified Yen model for asphaltene Langmuir film (B).

A view of the modified Yen model when molecules are compressed is proposed in Figure 4.19B. The modified Yen model can also be explained with the same results, but having a closer look at the BAM data. The presence of large aggregates can be readily seen at low surface pressures (Figure 4.14, *left column*, 10 mN/m), and these are further compressed to 30 mN/m (Figure 4.14, *left column*), but in IRRAS (Figure 4.13B) we can compress the monolayer to a much higher surface pressure, e.g., 45 mN/m. From the decompression data (Figure 4.14, *right column*) it can be seen that the Langmuir film presents cracks; therefore, the asphaltene film should be rigid. It is presumed that the

rigidity is related to the nanoaggregates interaction, which leads to the high reflectivity observed in the BAM micrographs. In IRRAS, the IR light should reflect from the water surface, thus penetrating the Langmuir film. If the large aggregates are very rigid, the IR light should only reflect from the top of the film and the light that penetrates the aggregates should be scattered, which would mean that cannot go in the MCT detector. The shift of the IR band from 2925 to 2920 cm^{-1} could account for the interdigitation of the nanoaggregates. This effect could account for the vertical orientation of the alkyl chains as determined by IRRAS with the bottom alkyl chains undetectable, as drawn in Figure 4.16B.

4.2.3 Conclusions

It was found that using *in situ* UV-vis spectroscopy at the air-water interface toluene is present for a longer time period than previously believed. Waiting 1 h after spreading allows the toluene to evaporate to reveal the trapped toluene within the asphaltene nanoaggregates. It was shown using surface pressure-area and compression-decompression isotherms that nanoaggregates are spread at the air-water interface using toluene as solvent. These results were also confirmed using p-polarized IRRAS and the thickness corresponding to the nanoaggregates was revealed using intermittent contact AFM of a single Langmuir film transferred onto HOPG using both Langmuir-Schaefer and Langmuir-Blodgett deposition techniques. Direct UV spectral measurement of asphaltene Langmuir films shows that small aromatic ring systems are not common in asphaltenes. Many of these findings could not have been obtained if the measurements had been performed at the toluene-water interface due to the presence of toluene. From

the additional data performed using benzene as spreading solvent, it can be inferred that aromatic solvents would lead to similar trapping within the asphaltene nanoaggregates.

4.3 Influence of Spreading Solvent: Chloroform

4.3.1 Background

While there has been much focus on asphaltenes in toluene, there has been much less focus on asphaltenes in other solvents. It is important to quantify characteristics of asphaltenes in solvents besides toluene in order to better assess their molecular architecture as well as their fundamental aggregation characteristics. The present work focuses on the investigation of UG8 asphaltene Langmuir film at the air-water interface using chloroform as spreading solvent. The results are compared to the results recently obtained using toluene as spreading solvent.

Additional measurements using Fourier transform ion cyclotron resonance (FT-ICR) mass spectrometry[88-91] are also confirming the result on the molecular weight of asphaltene. It is key to establish solvent-invariant properties of asphaltenes in particular in order to understand asphaltenes in their natural setting, crude oil. Important relationships have been established between asphaltene structures in toluene versus in crude oil, so extending asphaltene analysis in other solvents will put these findings into context. In addition, crude oil is difficult to work with as the maltene fraction is complex and not easy to characterize. Thus, it is important to quantify characteristics of asphaltenes in solvents besides toluene. A key issue is the use of the proper spreading solvent. It was previously shown that the use of toluene as a spreading solvent involves some key factors to be taken into account, e.g., toluene evaporation time.[77,92] This factor is fundamental to the elucidation of the molecular species present in the UG8 asphaltene

structure that can be studied using UV-vis spectroscopy. Typical absorbance spectra are shown in a region between 300 and 800 nm when the absorbance of asphaltenes is studied in solution, but 300 nm is UV cut-off wavelength for toluene; therefore, species absorbing at lower wavelengths cannot be quantified or possibly even detected. We have shown recently the implications regarding the use of toluene on the UG8 asphaltene Langmuir film UV-vis spectrum.[92] In this work we studied the interfacial properties of the UG8 asphaltene using specific techniques that include surface pressure-area isotherms, compression-decompression cycles, UV-vis and infrared reflection-absorption spectroscopy (IRRAS), Brewster angle microscopy (BAM) at the air-water interface and atomic force microscopy (AFM) for the Langmuir film transferred on solid support. It is shown here that the use of chloroform for generating asphaltene Langmuir film studies yields overall similarities with results from toluene; nevertheless, there are specific differences when using these two solvents. Chloroform presents major advantages over the use of toluene for interfacial studies of asphaltenes and most of the results exhibit some differences from those in toluene, like aggregate size. Nevertheless, one key general result is found: asphaltenes form nanoaggregates of very small aggregation numbers in chloroform as they do in toluene. This same conclusion has been obtained for crude oil. Consequently, this appears to be an intrinsic property of asphaltenes. The use of chloroform in the study of asphaltenes was previously reported in a single article[93] related to asphaltenes' fluorescence in solution, but interfacial work using chloroform as spreading solvent is virtually nonexistent in asphaltene research. The use of chloroform, as spreading solvent, was reported recently in the study at the air-water interface of a Brazilian crude oil[94] that contains 5% asphaltene.

4.3.2 Surface Chemistry

4.3.2.1 Surface Pressure-Area Isotherm

All measurements were performed with freshly prepared solutions. The surface pressure-area isotherm shown in Figure 4.20 (red dotted line) was obtained by spreading 35 µL of 1 mg/mL UG8 asphaltene prepared in chloroform. The experiments show good reproducibility with each measurement being repeated between three and five times. The apparent limiting molecular area, obtained by extrapolating the linear portion of the plot onto the x-axis, is 40 ± 2 $Å^2$/molecule. This area is much higher compared to the apparent limiting molecular area obtained for asphaltene when toluene is used (Figure 4.20, black line) as a spreading solvent (19 ±2 $Å^2$/molecule). The molecular diameter has been determined to be ~ 15 Å[66-72] in toluene.

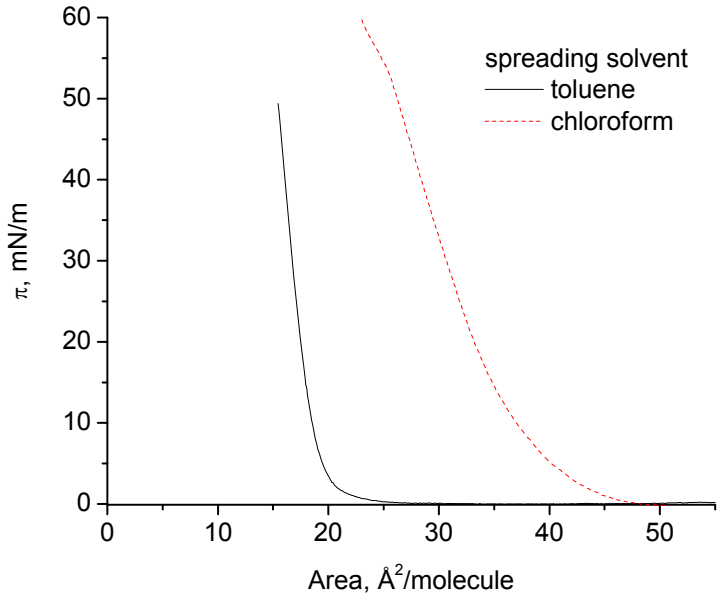

Figure 4.20. Surface pressure−area isotherms for UG8 asphaltene spread at the air−water interface from chloroform (····) and toluene **(—).**

The area per molecule determined here is much smaller than expected for molecular coverage (200-240 $Å^2$/molecule). The larger area per molecule for asphaltenes in chloroform compared to asphaltenes in toluene indicates that the aggregation numbers in chloroform are smaller than estimated in toluene (about 5-6), thus less than 10.[92] Consequently, the critical nanoaggregate concentration for asphaltenes in chloroform is found to be less than 1 mg/mL. We use the label *critical nanoaggregate concentration* but we note that with such small aggregation numbers, the formation of nanoaggregates should occur over a range of concentration. Since it is difficult to determine aggregation number by almost any technique when the numbers are very small, we have an estimate that turns out to be very consistent with aggregation numbers determined for asphaltene nanoaggregates in the bulk toluene.

4.3.2.2 Compression-Decompression Isotherm

Using compression-decompression cycles of the Langmuir film, it was found that UG8 asphaltene aggregates at the air-water interface. We have chosen two target surface pressures, 30 and 60 mN/m, respectively, for the compression-decompression cycles. As it can be seen from Figure 4.21, the decompression of the Langmuir film reveals a hysteresis effect attributed to the formation of larger aggregate structures. As expected, the degree of aggregation (hysteresis) increases with the surface pressure and with the number of compression-decompression cycles. The surface pressure decreases to 0 mN/m in the decompression cycles, which is not the case when toluene is used as a spreading solvent. Further investigation of the UG8 Langmuir film was carried out using *in situ* UV-vis spectroscopy using an HP diode array spectrophotometer.

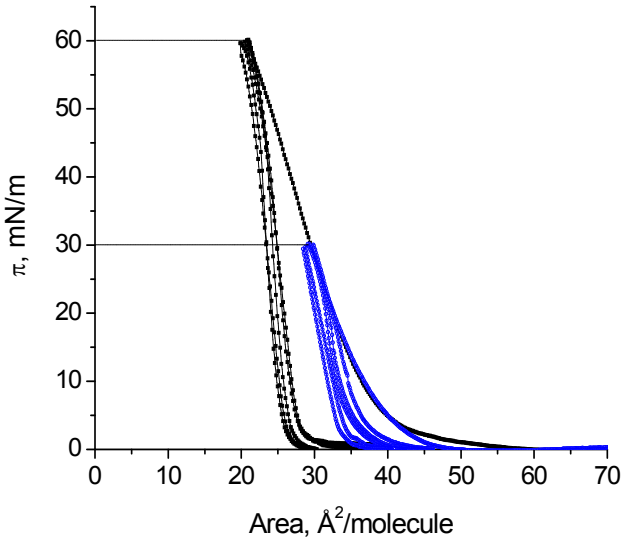

Figure 4.21. Compression−decompression cycles for UG8 asphaltene at the air−water interface spread from a chloroform solution with two target surface pressures of 60 mN/m (—) and 30 mN/m (—).

4.3.2.3 In situ UV-vis Spectroscopy

In the UV-vis data reported in the literature[62] all the spectra are presented from 300 or 350 to 800 nm. We have shown recently[92] that the absorption bands observed after 15 min waiting time period for asphaltene spread from a toluene solution belong to the spreading solvent and 1 h waiting time period is needed to allow the complete evaporation of the toluene. In Figure 4.22A, the UV-vis spectra of UG8 asphaltene are presented as a function of surface pressure after a waiting time period of 15 min is enough for the spreading solvent (chloroform) to evaporate. A similar result is obtained if, instead of 15 min time period for evaporation, the spreading solvent is allowed to evaporate for 1 h (Figure 4.22B). From these results, we can conclude that for *in situ* UV-vis spectroscopic analysis chloroform is a better spreading solvent compared to toluene, because it does not overlap with the spectral features of asphaltene, and there is no need

to wait 1 h to allow complete spreading solvent evaporation as when toluene is used. The most prominent feature of the UV-vis spectra of asphaltenes is that they exhibit a largely monotonically increasing absorption at shorter wavelengths. In a general sense, this indicates that there is a small population of small aromatic ring systems in asphaltenes.

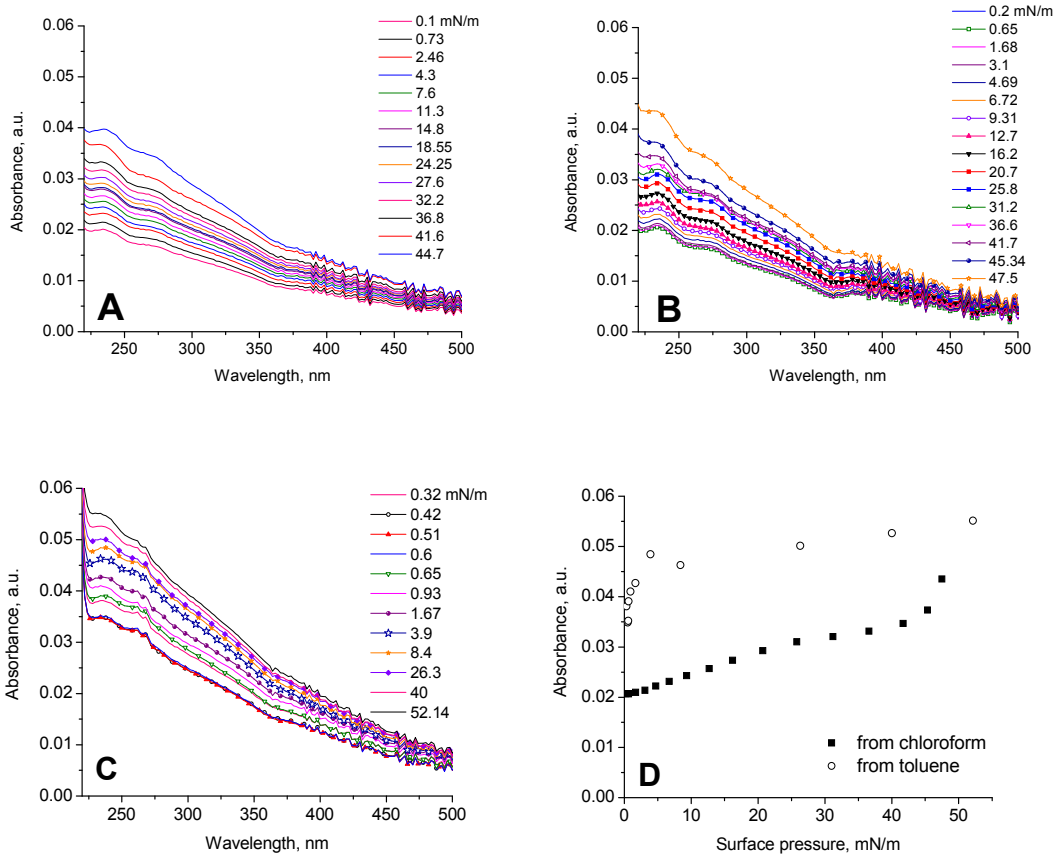

Figure 4.22. UV−vis spectra at the air−water interface for 1 mg/mL UG8 asphaltene in chloroform after solvent time of 15 min (A) and 1 h (B). Spectra obtained using toluene as spreading solvent after 1 h evaporation time period are presented (C), and absorption maxima from panels (B) and (C) at 234 nm as a function of surface pressure (D) are presented for comparison purposes.

Unlike larger polycyclic aromatic hydrocarbons (PAHs) the small aromatics have readily identifiable absorption regions. Consequently, the overall shape of the absorption spectra indicates there is at most a small population of small aromatic ring systems. The asphaltene spectral features include two absorption shoulders. The first, with the

maximum located at 234 nm, which is typical of some PAHs and the second shoulder is at 274 nm typical of isolated two-ring aromatics. This weak feature indicates there is some small fraction of asphaltenes with two fused rings. There is no peak evident where single-ring aromatics absorb at ~254 nm. This means that the contribution of single ring aromatics in asphaltenes is undetectable by direct spectral interrogation. This is in accord with previous results that there is a very small fraction of isolated single ring aromatics in asphaltene. Moreover, because single ring aromatics have an isolated absorption feature that is quite distinct from other aromatics, the occurrence of single ring aromatics in asphaltene would be readily detected. For example trapped toluene is readily detected (Figure 4.22C) when toluene is used as the spreading solvent. In addition, in Figure 4.22, there is only a small absorption peak at ~274 nm in the spectra; consequently, two-ring aromatics are also at most a small fraction of asphaltene aromatics. The direct determination here about the lack one-ring and two-ring aromatics in asphaltenes is consistent with previous findings.[80]

If toluene is used, in addition to these two spectral features, the vibronic spectrum of the trapped toluene overlaps the isolated benzene rings that are due to asphaltene. This is the third reason why chloroform is a better solvent to be used in the UV-vis investigation of UG8 asphaltene. When comparing the absorption spectra after 1 h obtained from chloroform (Figure 4.22B) and toluene (Figure 4.22C), it can be seen that the absorbance values are consistently higher in toluene compared to chloroform regardless of the surface pressure used. When the absorbance values at 234 nm are plotted against the surface pressure for the spectra obtained in Figures 4.22B and 4.22C,

it can be seen (Figure 4.22D) that the values are higher when asphaltene was spread from toluene compared to chloroform. Since the absorbance is defined as:

$$A = \varepsilon \times b \times c \qquad (4.1)$$

where A is the absorbance; ε is the molar absorptivity; b is the optical path and c is the concentration, for the air-water interface the concentration can be converted to surface density (ρ) (section 8.2.2 for the mathematical treatment). Since the molar absorptivity (ε) is constant for a given wavelength, the only way the absorbance in toluene can be higher compared to chloroform is if the surface density is higher ($A = \varepsilon \times \rho$). In our view, the only way the surface density could be higher is if the aggregate size is larger, therefore containing more asphaltene molecules per unit area. This interpretation is in agreement with the surface pressure-area isotherms presented in Figure 4.20, which shows a smaller apparent limiting molecular area for toluene therefore more molecules per unit area. Based on this interpretation, the concentration (c) would have a higher value, but based on the molecular weight of the asphaltene which is fairly large (750 Da), the sample is aggregated, which means that also the optical path (b) has to be higher (higher b would mean thicker Langmuir film). Taking all these factors into account, the combination ($b \times c = \rho$) should be higher, which in turn gives a higher value for the observed absorbance (A). From the shape of the plots in Figure 4.22D, it can be seen that there is no continuous or linear increase in the absorbance values as a function of surface pressure, which is an indication that aggregates are formed. Smaller or larger aggregates get in the path of the UV light and therefore the intensity is expected to vary from one surface pressure to another. Chloroform could be intercalated within the aggregates but the fact that it does not have UV absorption, in the region where asphaltene does, allows the

identification of the absorbance features of asphaltene. Regardless if chloroform is intercalated within the aggregates or not, it is clear that the *in situ* absorbance of the Langmuir film for asphaltene is always higher when spread from toluene compared to chloroform when similar surface pressures are compared. Based on these experimental facts, the author imply that toluene could be intimately involved in the aggregation process due to possible π-π interactions that could stabilize the asphaltene aggregates while chloroform cannot form π-π interactions with the aromatic core of asphaltene. This does not mean that chloroform could not be intercalated within the aggregates but could explain the smaller aggregate size.

4.3.2.4 Stability Measurements

To assure that the Langmuir film is stable at the air-water interface (no molecules are lost in the subphase), we have performed stability measurements as a function of time at constant surface pressure and monitored the change in the molecular area (Figure 4.23A). For a surface pressure set at 30 mN/m, the change in the molecular area is negligible over a time period of more than 4500 s. Based on this data, the UG8 asphaltene Langmuir film can be considered as being stable. The second reason for keeping the surface pressure constant and monitoring the area as a function of time (Figure 4.23A) is related to the deposition of the UG8 asphaltene Langmuir film. To ensure a good transfer onto the solid substrate, the surface pressure is therefore kept constant during both the Langmuir-Schaefer and Langmuir-Blodgett depositions. The surface pressure relaxation as a function of time is shown in Figure 4.23B after a target surface pressure of 30 mN/m is reached and is measured over a time period greater than 6000 s.

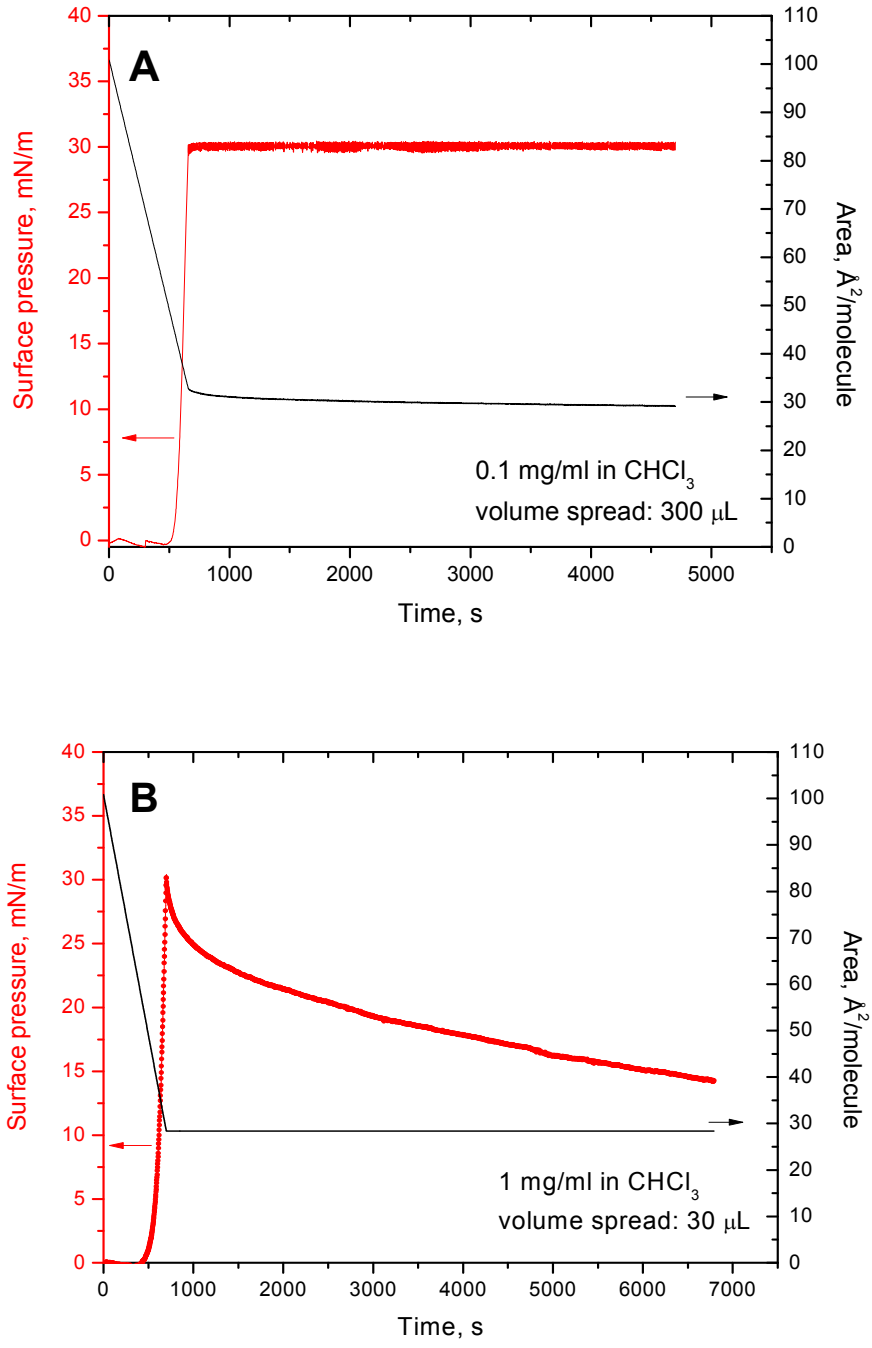

Figure 4.23. Stability for UG8 asphaltene Langmuir film spread from chloroform (molecular area as a function of time (—) under constant surface pressure (—) of 30 mN/m) (A) and surface pressure relaxation as a function of time (—) under constant area (—) (target surface pressure was 30 mN/m) (B).

4.3.3 Infrared Reflection-Absorption Spectroscopy

The next method used for the investigation of the UG8 asphaltene Langmuir was p-polarized IRRAS.

Initially, we have compressed the asphaltene Langmuir film to a surface pressure of 10 mN/m and we performed p-polarized IRRAS for different incident angles (Figure 4.24A). It is known that in p-polarized IRRAS the vibration bands parallel to the water surface appear negative at angles below the Brewster angle of water, which is 53.12°. For incident angles larger than the Brewster angle, the bands become positive and at the Brewster angle the signal is nil.[15,83] As shown in Figure 4.24A, the intensity of the bands is increasing towards the Brewster angle, for the negative bands, while after the Brewster angle the intensity is decreasing with the increase in the incident angle. Based on this fact, the observed bands, typical of symmetric and asymmetric C-H stretching (2850 and 2920 cm^{-1}) and the terminal $–CH_3$ group from the hydrocarbon chains at 2960 cm^{-1} are not parallel to the water surface but have a rather oblique orientation.

Figure 4.24B shows the increase in the band intensities with the surface pressure at a fixed incident angle of 69°, which is a consequence of the increased molecular density at the interface during compression. Interestingly enough, while we do observe the C-H stretching, both symmetric and asymmetric, and the terminal methyl group, the position of the bands does not change except at a surface pressure of 5 mN/m. Usually, during compression the symmetric and asymmetric C-H stretching bands are located at higher wavenumbers (up to 10 cm^{-1}) and shift, upon compression, to 2850 and 2920 cm^{-1}, for the symmetric and asymmetric stretch respectively, when the hydrocarbon chains adopt the all-trans conformation.

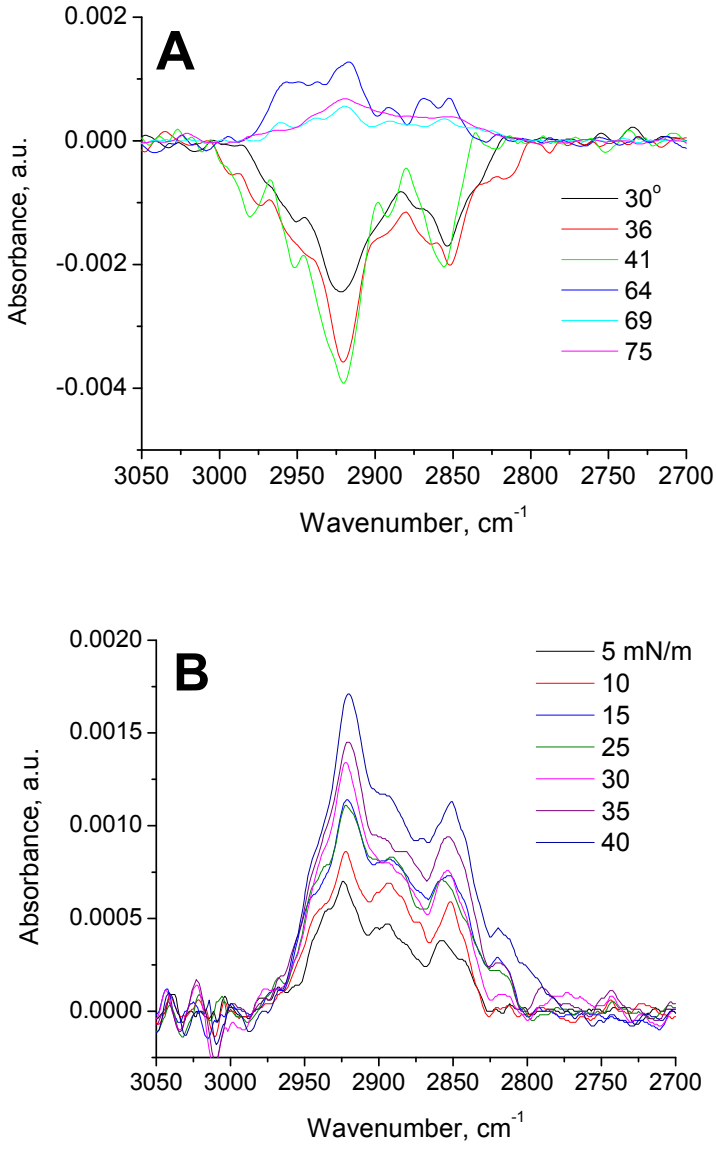

Figure 4.24. p-polarized IRRAS at the air−water interface of 1 mg/mL UG8 asphaltene in chloroform at a fixed surface pressure (10 mN/m) as a function of the incident angle (A) and at a fixed incident angle of 69° as a function of surface pressure (B).

Due to the fact that the IR band positions do not change is a direct proof that the UG8 asphaltene is already aggregated when it is spread on the water surface. The small shift from 5 mN/m to higher surface pressures is assigned to the interaction between the aggregated UG8 asphaltene domains.

4.3.4 Brewster Angle Microscopy

Brewster Angle Microscopy (BAM) was employed to visualize the aggregates *in situ*. In brief, the measurements were performed using a 53.15° incident angle, which is known to be the value for the Brewster angle of pure water. The micrographs obtained are shown in Figure 4.25. The *left column* shows the micrographs obtained as a function of the surface pressure during the compression of the asphaltene Langmuir film. Some structures can be seen at low surface pressures (1.3 mN/m). Upon compression, the aggregation of the asphaltene occurs which is translated in the appearance of domains. Some homogeneous regions appear (5 mN/m), but compression to high surface pressures (45 mN/m), leads to the increase in the size of the domains and dark spots (water) are visible. The results obtained during decompression of the Langmuir film are shown in Figure 4.25 *right column*. What it can be observed from the BAM micrographs is that the aggregates that were formed during the monolayer compression (surface pressure of 63 mN/m) remain the same, and large spaces (dark region consisting of the water surface) appear when the barriers are relaxed to produce a decrease in the surface pressure between 63 and 0 mN/m (micrographs at 17 and 8 mN/m are shown as examples). Based on these results, the author can clearly state that the structures formed by compression of the asphaltene Langmuir film are truly aggregates and the data are consistent with the results previously reported.[62] Moreover, our interpretation of the compression-decompression cycles shown in Figure 4.18 is confirmed by the BAM data. Recent data using BAM were reported on the topography of the asphaltene Langmuir film[95-97], but the literature data[94,96,97] using BAM provides low resolution micrographs.

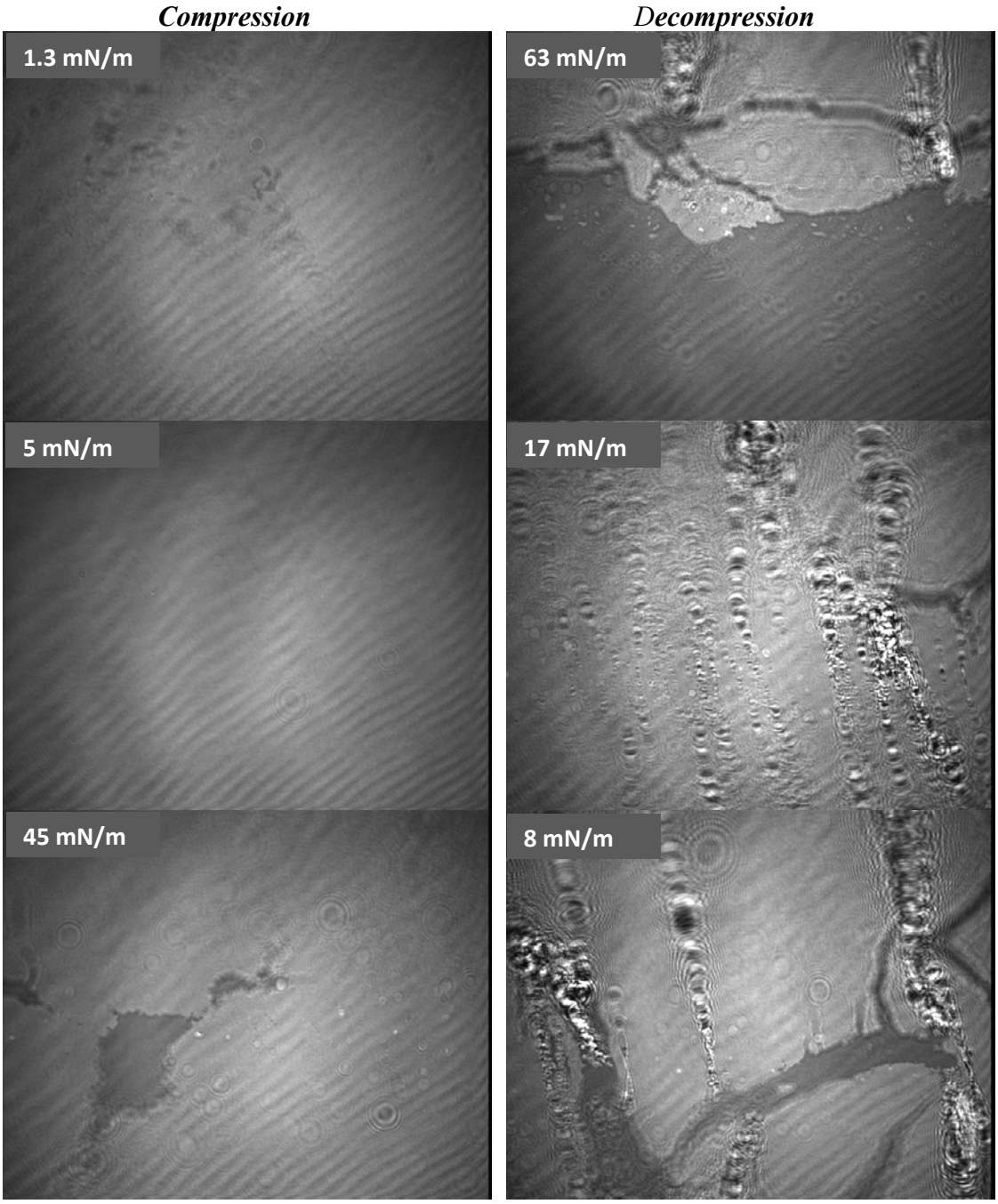

Figure 4.25. Brewster angle microscopy of UG8 asphaltene (1 mg/mL in chloroform) Langmuir film during compression (left column) and decompression (right column). Image size is 200 μm × 200 μm.

4.3.5 Atomic Force Microscopy

AFM measurements were performed in order to have a closer look at the topography of the aggregates.

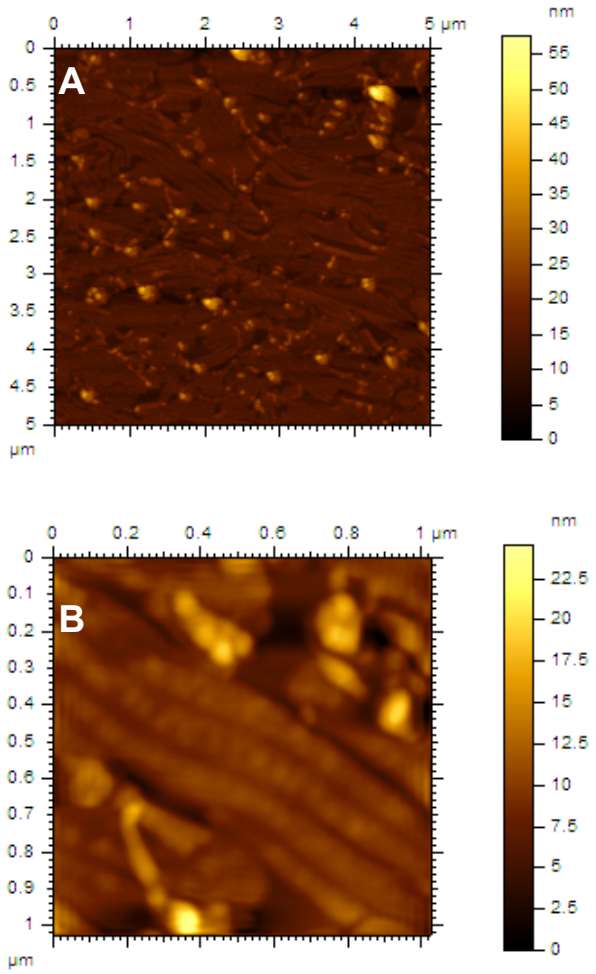

Figure 4.26. Intermittent contact AFM micrographs of Langmuir−Schaefer film transferred on HOPG substrate using chloroform as spreading solvent at a surface pressure of 15 mN/m for different scan areas of 5 × 5 µm (A) and 1 × 1 µm (B).

HOPG is known to be hydrophobic and therefore is suitable to transfer the asphaltene For this purpose, a single Langmuir film of asphaltene was transferred onto HOPG at a surface pressure of 15 mN/m from chloroform solution using both Langmuir-Schaefer (Figure 4.26) and Langmuir-Blodgett (Figure 4.27) deposition techniques. film.

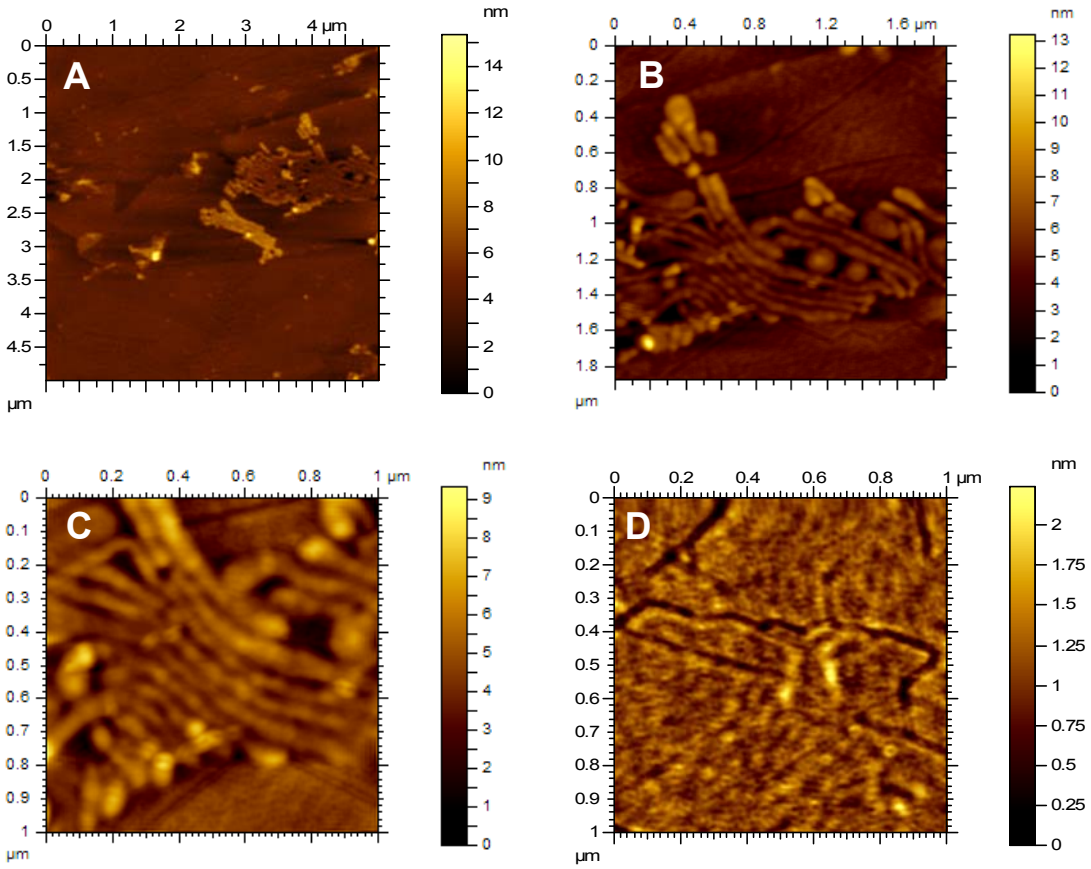

Figure 4.27. Intermittent contact AFM micrographs of Langmuir−Blodgett film transferred on HOPG substrate using chloroform as spreading solvent at a surface pressure of 15 mN/m for different scan areas of 5 × 5 µm (A), 1.8 × 1.8 µm (B), and 1 × 1 µm (C) showing large aggregates and a scan area 1 × 1 µm showing nanoaggregates (D).

As it can be seen from Figures 4.26 and 4.27, the shape of imaged aggregates is different depending on the deposition technique. Regardless of the deposition technique used it is clear that the average aggregate size is about 15 – 20 nm. Figure 4.26 shows an image with the Langmuir-Schaefer (horizontal deposition) at two different area sizes. In Figure 4.26A, a region of 5 µm × 5 µm is imaged and shows very good deposition of the asphaltene Langmuir film with an average film thickness of 15-20 nm. A second scan on a smaller area (1 µm × 1 µm) confirms the same average thickness of the film, but in

addition to the thickness provides a better film topography of the asphaltene aggregates (Figure 4.26B). In Figure 4.27, different area sizes and regions are presented for a Langmuir-Blodgett film. Figure 4.27A (5 μm × 5 μm) shows regions with large aggregates and regions that appear as having no aggregates present. Smaller regions containing the large aggregates are presented in Figure 4.27B (1.8 μm × 1.8 μm) and 4.27C (1 μm × 1 μm).

In Figure 4.27D is presented a region that on a larger scale (Figure 4.27A) appears as having no aggregates, but it can be seen that the average thickness is about 1.5 – 1.75 nm, which corresponds closely to a nanoaggregated state of asphaltene in toluene for 1 mg/mL concentration as previously reported in literature using other techniques (High-Q Ultrasonics) which show that the critical nanoaggregate concentration (CNAC) is about 0.1 mg/mL.[84,85] Our AFM data is compared to the results obtained in toluene using the techniques mentioned above in the literature because no data in chloroform was reported until today. The explanation for this effect relies on the initially formed small aggregates (about 1-2 nm) in solution and that are spread at the air-water interface. This result appears to be similar in both chloroform and toluene. However, the large aggregates formed during compression have different sizes (20-70 nm from toluene vs 15-20 nm from chloroform) and shapes (globular for toluene and rod-like for chloroform). Upon compression ,the nanoaggregates interact and lead to the formation of large-sized aggregates as shown by BAM and AFM. Therefore, during compression, the Langmuir film consists of a binary mixture of small and large aggregates. The compression-decompression isotherms also confirm this experimental result as well as the author's interpretation due to the fact that each compression-decompression cycle leads to the

formation of large aggregates from the portion of the small aggregates still present in the Langmuir film.

4.3.6 Conclusions

In large part, because asphaltenes are defined to be toluene soluble, most solution studies of asphaltenes have involved toluene. In particular, nanoaggregates of small aggregation number have been observed in toluene. However, little is known about the behavior of asphaltenes in other good solvents. Here, we show that similar yet somewhat smaller asphaltene nanoaggregates are found here in chloroform. This is an indication that asphaltene nanoaggregate formation is an intrinsic property of asphaltenes as is likely related to their molecular structure. That is, the attractive molecular component (aromatic ring system) is in the molecular interior while repulsive molecular component (alkane chains) are in the molecular exterior; this asphaltene molecular architecture naturally gives rise to small nanoaggregates. Moreover, UV-vis spectroscopy herein confirms that asphaltene aromatics are not dominated by single-ring and two-ring aromatics. This direct spectral determination is consistent with this corresponding asphaltene molecular architecture. Using *in* situ UV-vis spectroscopy at the air-water interface, it was found that using chloroform as a spreading solvent there is no need to wait 1 h to allow the solvent to evaporate as in the case of toluene. It was shown using surface pressure-area and compression-decompression isotherms that nanoaggregates of asphaltene are spread at the air-water interface regardless if chloroform or toluene are used as solvents. These results were also confirmed using p-polarized IRRAS and the thickness corresponding to the nanoaggregates was revealed using intermittent contact AFM of a single Langmuir film transferred onto HOPG using both Langmuir-Schaefer and Langmuir-Blodgett

deposition techniques. The size of the aggregates and nanoaggregates is smaller when UG8 asphaltene solution is prepared in chloroform compared to toluene, presumably due to the lack of solvent trapping that is present when toluene is used. The shape of the aggregates formed by the compression of the nanoaggregates varies from globular (obtained from toluene)[92] to rod-likestructures (present work). The previously proposed model of architectural structure[92] based on the modified Yen model[79] is also applicable and supported by the present work.

Chapter 5. Characterization of Antibodies and Human Cardiac Troponin I

5.1 Background

The basic structure of an IgG antibody has been elucidated as a symmetric monomer consisting of two identical heavy chains and two identical light chains, connected via disulfide bonds[98,99] (Figure 5.1A).

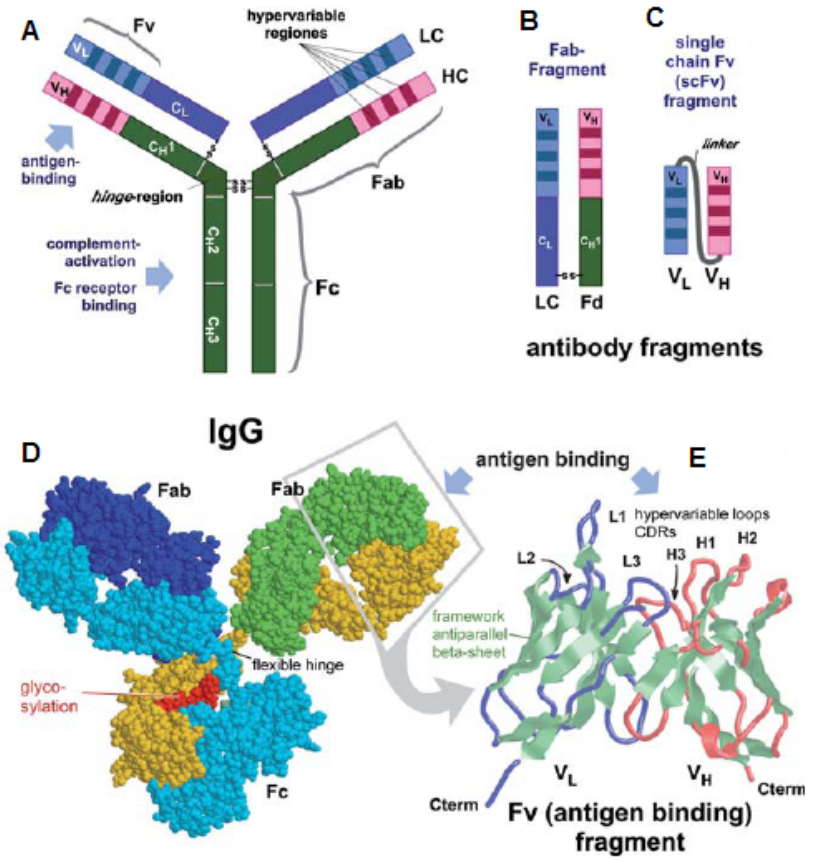

Figure 5.1. Structural components of an IgG antibody showing the Y-shaped geometry (A), the antibody fragments (B and C), an X-ray crystallography-based space filling model (D) and the antigen binding site at the N-terminus variable region with 110 amino acids (E).

According to the distinct heavy chains, five classes of immunoglobulins can be distinguished, namely IgG, IgM, IgD, IgA, and IgE. Each antibody contains one type of light chain, kappa or lambda. (Figure 5.1B, 5.1C). Both, heavy and light chains posses a

variable region of 110 amino acids at the N-terminus with three hypervariable segments called complementarity determining regions (CDRs) (Figure 5.1E). The hypervariable loops form the two antigen binding (or antigen-combining) sites of an IgG molecule and determine its specificity. In contrast, the constant part of the immunoglobulin (Fc region) is responsible for secondary effects like activation of the complement system or binding to cellular Fc receptors. A space filling model based on X-ray crystallographic data of an antibody is shown in Figure 5.1D.

Immunoglobulin G (IgG, 150 kDa) is the most abundant immunoglobulin in serum, accounting for up to 80% of all secreted antibodies. There are four different IgG isotypes in humans (IgG1, IgG2, IgG3, and IgG4) and mouse (IgG1, IgG2a, IgG2b, and IgG3). Isotypes show differences in their heavy chain constant domains but not in the light chain constant domain.[100]

Immunoglobulin M (IgM, 900 kDa) accounts for approximately 10% of serum antibodies and it is expressed as monomer on B lymphocyte as antigen receptor, whereas the secreted form consists of a pentamer held together by a J (joining) chain.

Immunoglobulin D (IgD, 180 kDa) is only found in fairly low amounts in the serum but is the major membrane-bound form expressed on mature B cells.

Immunoglobulin A (IgA, 160 kDa) constitutes about 10–15% of serum antibodies. It represents the major antibody class due to its secretion in tears, saliva, and mucus of the bronchial, genitourinary, and digestive tracts. Whereas the prevalent form in the serum is a monomer, the secretory IgA usually consists of dimers.

Immunoglobulin E (IgE, 180 kDa) is found in the serum only in trace amounts. IgE antibodies are responsible for immediate hypersensitivity and cause the symptoms of fever, asthma and anaphylactic shock.

5.1.1 Monoclonal Antibodies

The key feature of an mAb is its unique specificity. It recognizes only one particular antigenic determinant (called epitope) on a given molecule – that means it is monospecific. All antibodies secreted by an individual hybridoma represent identical immunoglobulin molecules that display identical binding strengths to its antigen (referred to as affinity) and have identical physicochemical properties (isotype, stability). This homogeneity will give rise to the same immunological effector functions. In principle, mAbs can be produced in unlimited quantities; the hybridoma cell itself survives after cryopreservation at least for decades. The majority of mabs are directed against conformational epitopes of an antigen.

5.1.1.1 Production of Monoclonal Antibodies

For mab production, most commonly mice and rats, and less frequently hamsters, and rabbits are immunized with antigen by distinct routes of administration. Antigen may consist of cellular components, purified proteins, peptides, carbohydrates, lipids, or nucleic acids and for each of these specific immunization protocols are available.[101-103] The mouse monoclonal antibodies used in the current work were produced using hybridoma clones that were derived by hybridizing Sp2/0 myeloma cells with spleen cells of Balb/c mice immunized with free human cardiac troponin I. The Balb/c mouse is a popular strain of mice used in many research applications but most popular to the

production of monoclonal antibodies. It is an albino, small-sized mouse obtained by 20 or more repeated inbred brother-sister matting.[104] The first mouse antibody (mab) used in the current research is mab 560, an IgG1 isotype, that binds to the amino acid sequence 83 – 93 from the human cardiac troponin I (cTnI).

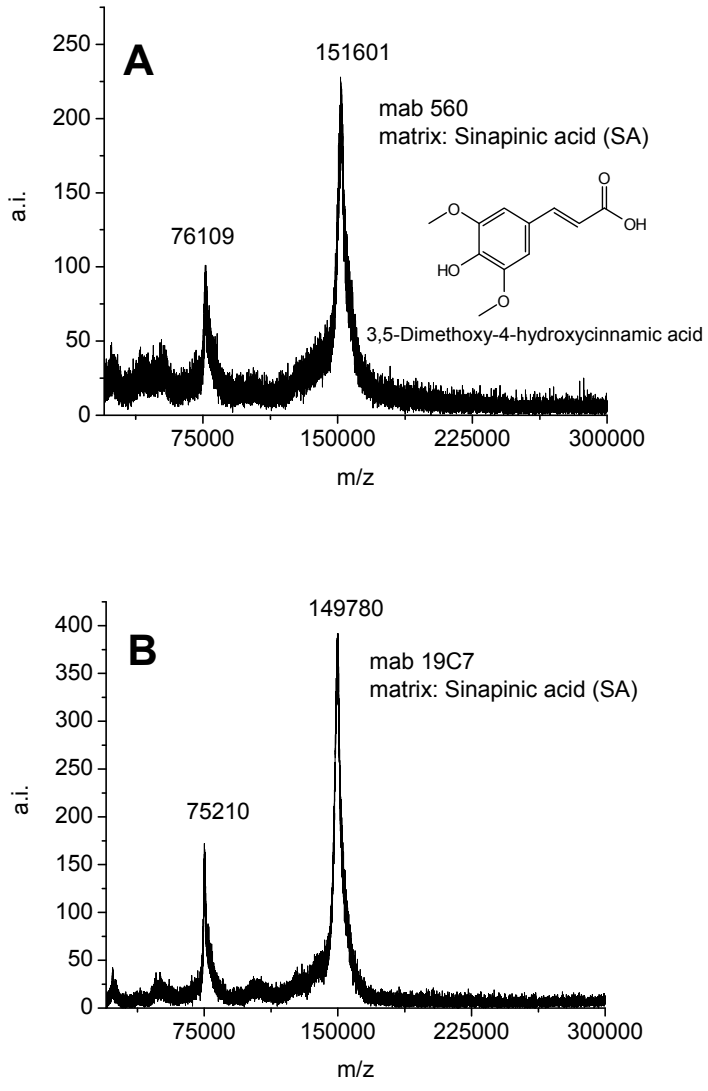

Figure 5.2. MALDI-TOF spectrum of mabs 560 (**A**) and 19C7 (**B**) using sinapininc acid as matrix.

The second antibody used was mab 19C7, an IgG2b isotype that binds specifically to the amino acid sequence 41 – 49 from cTnI, according to the manufacturer's (Hytest, Turku, Finland) data sheet (catalog #: 4T21).[105]The molecular weights were obtained using a Bruker BiFlex IV matrix-assisted laser desorption/ionization coupled with the time-of-flight (Maldi-TOF) mass spectrometer available in the Department of Chemistry at University of Miami using sinapinic acid as matrix (Figure 5.2A and 5.2B).

The choice for mab 560 is based on its main use as capture antibody on surfaces when a sandwich immunoassay is used for cTnI detection. From six antibody combinations recommended by the manufacturer (Hytest, Finland), four include mab 560 as capture antibody.Therefore, the binding of cTnI from the subphase with an antibody at the air-solution interface makes mab 560 a perfect candidate.

5.2 Surface Chemistry of Mutant Antibody (mab) 560

5.2.1 Surface Pressure – Area Isotherm

Figure 5.3 shows the effect of salt (KCl) concentration on the surface pressure – area isotherm of mab 560. To obtain the surface pressure – area isotherm, 50 μL solution in mab 560 1 mg/mL in phosphase saline buffer (PBS, pH = 7.4) was initially spread on the water surface with an area of 225 cm^2. After 15 min waiting time the monolayer was compressed. As shown in Figure 5.3, when the subphase is pure water, no surface pressure – area isotherm can be obtained. This is due to the solubilization of the protein in the subphase. To avoid this drawback and to obtain the best conditions for a stable monolayer different concentrations between 0.2 and 3 M KCl are used as subphase to favor the protein salting-out effect as was previously explained in section 2.3. It is clearly

visible that an increased concentration of salt in the subphase causes an increase in the surface molecular area of the monolayer. From a closer look at Figure 5.3 it seems that a 3 M KCl subphase should be the one that gives the best result in terms highest surface molecular area.

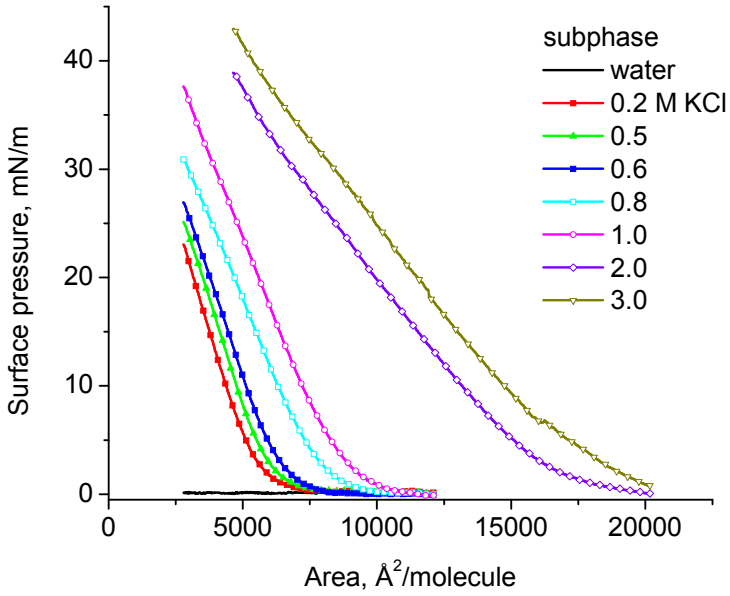

Figure 5.3. Surface pressure – area isotherm for mab 560 on subphases having different KCl concentrations.

If a subphase containing 3M KCl gives the best monolayer stability, when different spreading volumes are used, the limiting molecular area should stay the same regardless of the volume spread at the air-solution interface. The limiting molecular area is a property of the amphiphile for which the interfacial properties are determined. When different volumes are spread on the air-solution interface, the number of molecules is different, and therefore the total total number of molecules per unit area is changing. This is reflected in the starting point of the surface pressure – area isotherm, for example if the spreading volume is doubled, the area should be half compared to the one obtained

initially before doubling the spreading volume. Equation (5.1) can be used to explain this effect[1].

$$Area = \frac{A \times M}{C \times N_A \times V} \qquad (5.1)$$

Here, A is the monolayer area, M is the molecular weight of the compound forming the monolayer, N_A is Avogadro's number, C is the concentration of the spreading solution in mass per unit volume, and V is the volume of the spreading solvent.

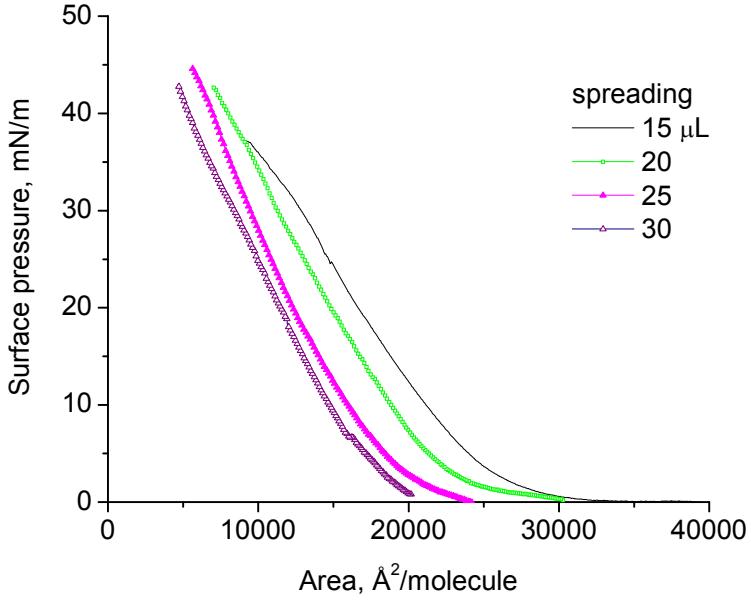

Figure 5.4. Effect of spreading volume on the surface pressure – area isotherm of mab 560.

As shown in Figure 5.4, the use of different spread volumes does not lead to a reproducible surface pressure – area isotherm. Actually, with an increased volume that is spread, the molecular surface area seems to decrease. This can be explained by the high salt concentration available in the subphase. When an increased volume of mab 560 is

spread at the air-solution interface, some of the salt ions (K^+ and Cl^-) could interact with the mab 560 molecules leading to protein unfolding and/or solubilization.

In order to test this hypothesis we have performed stability measurements where the surface pressure is held constant and the decrease of the molecular area is followed as a function of time.

5.2.2 Stability Measurements

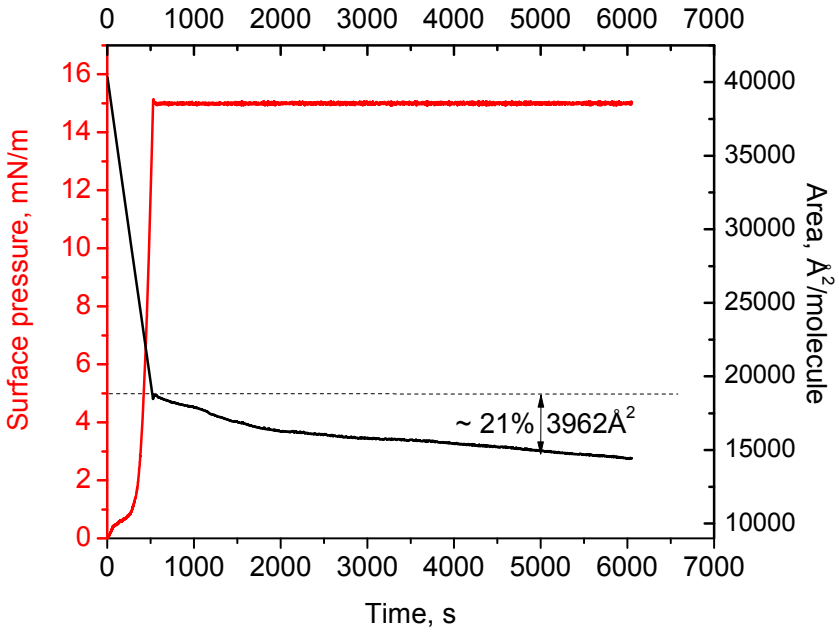

Figure 5.5. Stability isotherm for mab 560 spread at the air-solution interface (—) on a subphase containing 3M KCl and compressed to 15 mN/m (—).

A volume of 20 µL mab 560, 1mg/mL in PBS buffer was spread on the surface of a 3 M KCl solution used as subphase. After 15 min waiting time for monolayer equilibration, the monolayer was compressed to a target surface pressure of 15 mN/m and the surface pressure was kept constant for over 6000 s. Figure 5.5 shows the constant surface pressure as a function of time (red line) and the evolution of the molecular area as a function of time (black line). In order to maintain the surface pressure constant the

barriers will slowly move and eventually decrease the molecular area. For an insoluble monolayer, for example asphaltene, the decrease of the molecular area is insignificant (Figure 4.8A). For mab 560, the decrease was calculated at about 21% after a time period of 5000 s.

If this decrease is due to unfolding or solubilization, the decrease in the molecular area should be higher than the one obtained on a subphase containing 2M KCl. Figure 5.6 shows the stability measurement for the same monolayer but instead of 3M KCl the subphase contains 2 M KCl.

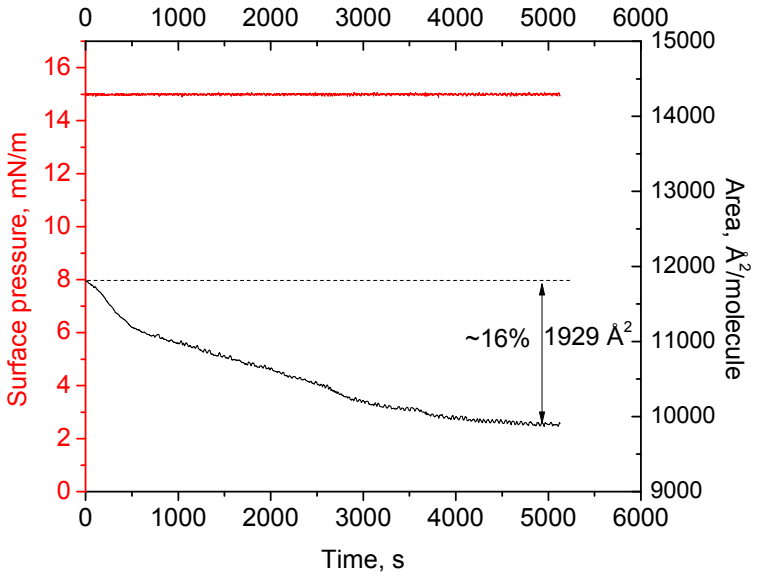

Figure 5.6. Stability isotherm for mab 560 spread at the air-solution interface **(—)** on a subphase containing 2M KCl and compressed to 15 mN/m **(—)**.

While the surface pressure is held constant at 15 mM/m, the molecular area is decreasing in a similar fashion as when 3M KCl was used. However, in this case, the decrease measured after 5000 s, (the time was kept the same to be able to compare the molecular areas) is only 16%.

The initial assumption was that at higher salt concentrations, more mab 560 molecules are going to be found at the interface. This would lead to increased stability and should reflect a smaller decrease in the molecular area with increased salt concentration. This was initially true up to the point where the salt concentration was too high (3M KCl) and started to affect the interfacial properties of the mab 560 molecules.

5.2.3 Compression – Decompression Isotherm

To further test the hypothesis of unfolding/solubilization, the author performed compression – decompression cycles of the mab 560 monolayer on both 3 and 2M KCl subphases, respectively, for the same target surface pressure of 15 mN/m.

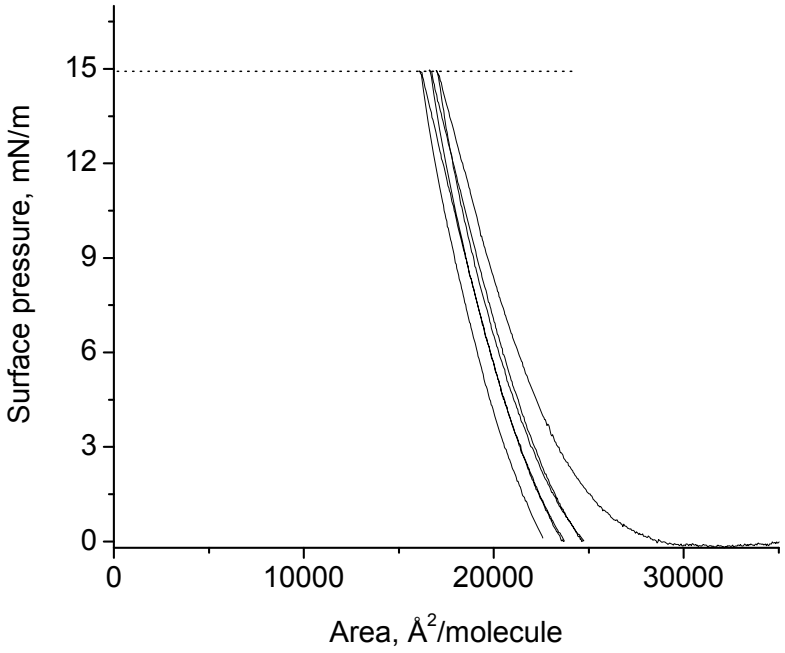

Figure 5.7. Four compression – decompression cycles of mab 560 monolayer spread on 3M KCl at a target surface pressure of 15 mN/m.

Figure 5.7 shows the compression – decompression cycles on 3M KCl. It can be seen that with each compression – decompression cycle, the molecular area decreases. This could

mean that more molecules are possibly solubilized in the subphase due to the interaction with the K^+ and Cl^- ions. When the measurement is repeated on a subphase containing 2M KCl (Figure 5.8), the same effect is not present.

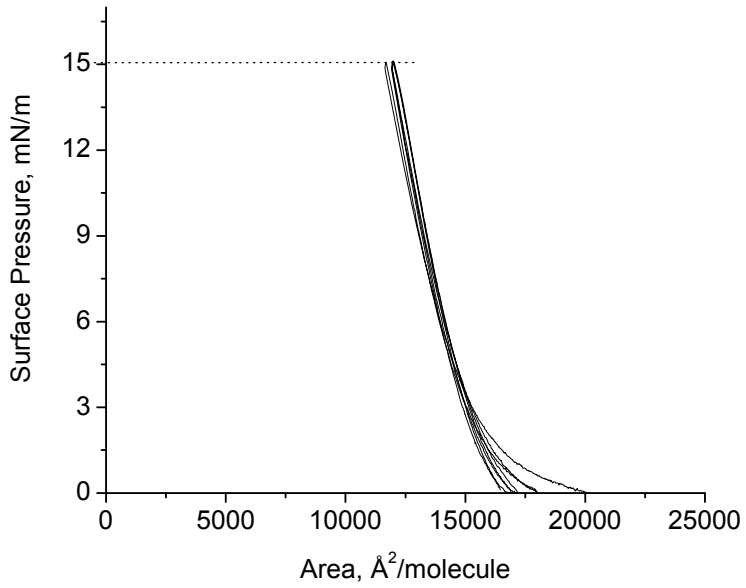

Figure 5.8. Four compression – decompression cycles of mab 560 monolayer spread on 2M KCl at a target surface pressure of 15 mN/m.

The lack of decrease in the molecular area when mab 560 is spread on 2M KCl means that no mab molecules are solubilized during the compression – decompression cycles, as seen in the case when 3M KCl is used, which in turn means that 2M KCl is a better subphase to use for the interfacial characterization of mab 560. Based on these findings, all additional measurements were performed on 2M KCl subphase.

These measurements were performed with the purpose to detect human cardiac troponin I when is is injected in the subphase. In brief, we intend to form a monolayer of mab 560, compress it at surface pressures of 5 mN/m or higher and keep the molecular area constant. The next step would be to inject human cardiac troponin I in the subphase

and follow the increase in the surface pressure after the injection. If cTnI binds to mab 560, there should be an increase in the surface pressure caused by the presence of the cTnI molecules that are bound to mab 560. As more cTnI would diffuse to the interface until most mab 560 molecules are binding cTnI, a saturation-type of curve should be obtained. It is not desired that the unbound cTnI molecules should be present at the interface.

5.2.4 Surface Pressure – Area Isotherm

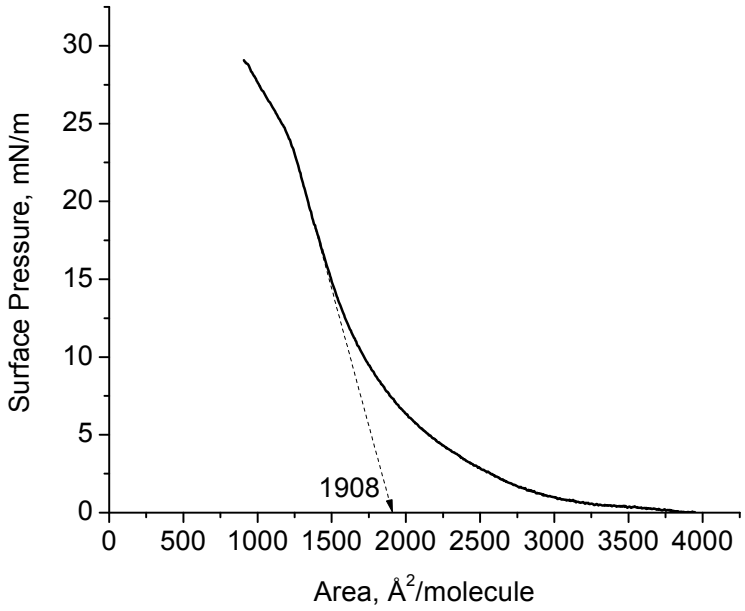

Figure 5.9. Surface pressure – area isotherm of cTnI, 0.7 mg/mL in PBS spread on 2M KCl.

To investigate the binding of cTnI to mab 560, we first performed a surface pressure – area isotherm for cTnI on 2M KCl. As a reminder, 2M KCl was the best performing subphase for mab 560 monolayer stability.

When cTnI is spread on the air-solution interface with a subphase containing 2M KCl, the monolayer was compressed after 10 min waiting time for equilibration. A limiting

molecular area of 1908 $Å^2$/molecule was obtained for cTnI. In addition, the monolayer showed a collapse surface pressure at 23.5 mN/m (Figure 5.9).

5.2.5 Stability Measurements

In order to perform the stability measurements, the cTnI monolayer was compressed to a target surface pressure of 15 mN/m and was kept constant while monitoring the decrease in the surface molecular area over time. A decrease of about 9% was obtained over a time period of over 4000 s (Figure 5.10), which is acceptable for a protein monolayer.

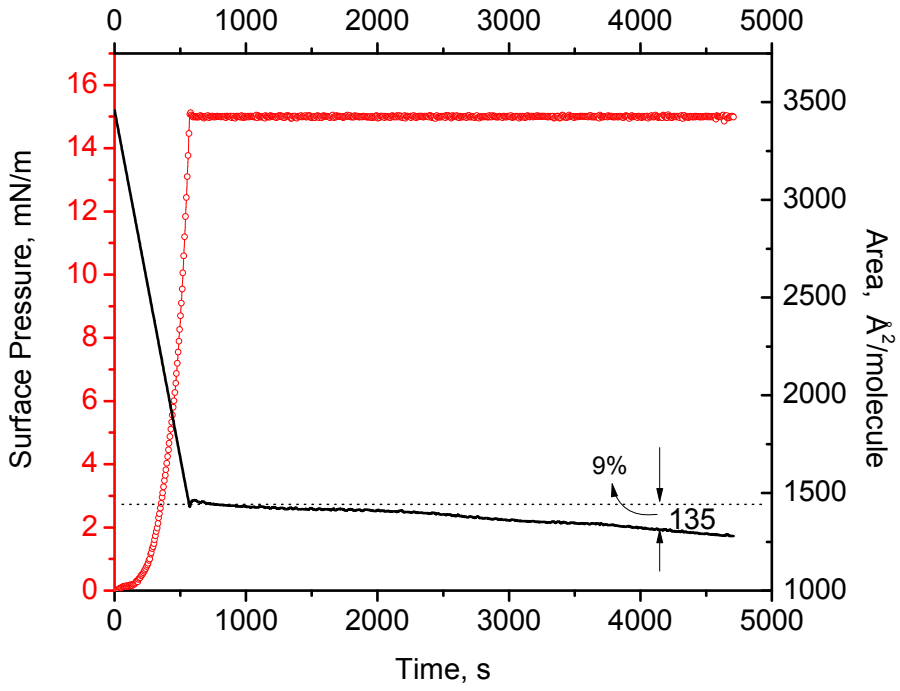

Figure 5.10. Stability isotherm for cTnI spread at the air-solution interface (—) on a subphase containing 2M KCl and compressed to 15 mN/m (—) .

5.2.6 Surface Pressure–Area Isotherm

The next step was to mix mab 560 with cTnI and obtain the surface pressure – area isotherm. For this purpose, a mixture was obtained in which mab 560 had a concentration

of 0.5 mg/mL and cTnI had a concentration of 0.63 mg/mL. In order to be able to compare the surface pressure – area isotherms, the input in the software was related only to the presence of mab 560. Therefore knowing the limiting molecular area and the surface pressure – area isotherm for mab 560, any increase in the molecular area should be due to the presence of cTnI. The three surface pressure – area isotherms for pure cTnI and mab 560 as well as the mixture are shown in Figure 5.11.

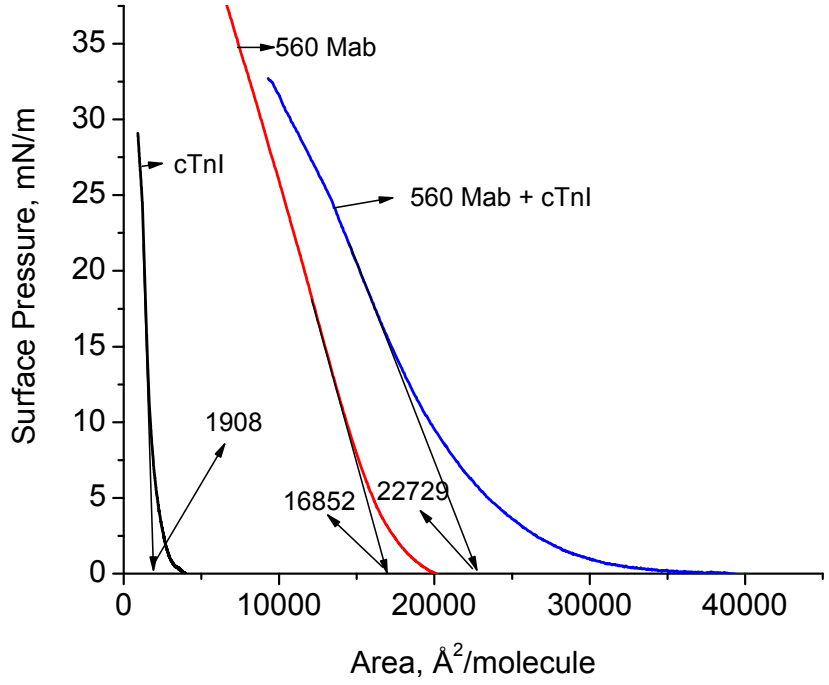

Figure 5.11. Surface pressure – area isotherm for cTnI (—), mab 560 (—) and their mixture (—) on 2M KCl.

As can be seen from Figure 5.11, the molecular area obtained for the mixture of mab 560 and cTnI is much higher than for two components. The limiting molecular area for cTnI and mab 560 is 1,908 and 16,852 Å^2/molecule, respectively. Their calculated sum is 18,760 Å^2/molecule while the experimental value is 22,729 Å^2/molecule. The increase

could be explained by a reorientation of the mab 560 molecules in the mixed monolayer, to accommodate the bound cTnI, compared to the pure mab 560 monolayer.

But the surface pressure – area isotherm for the mixture cannot account or monitor the binding between mab 560 and cTnI, as the two proteins were mixed in solution, prior to spreading.

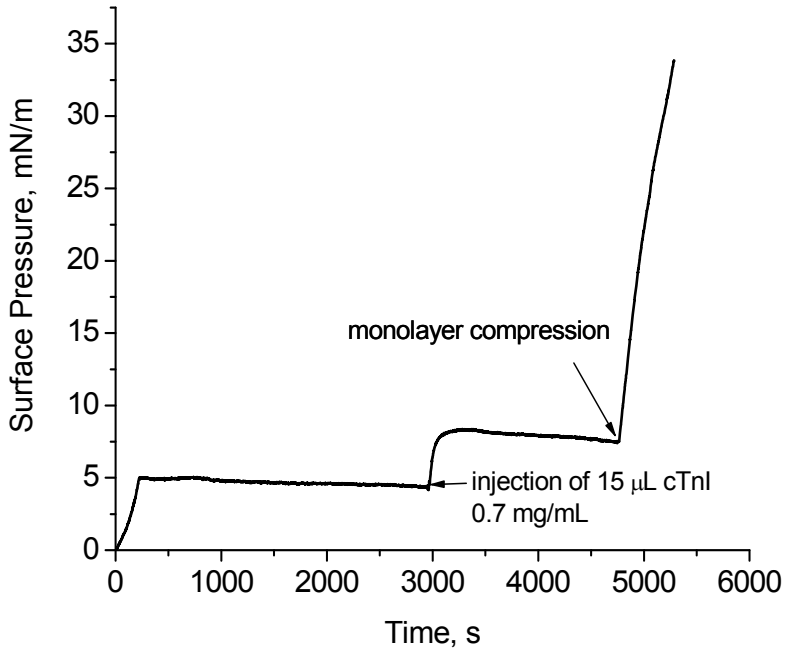

Figure 5.12. Surface pressure vs. time for mab 560 Langmuir film prior and after injection of 15 μL 0.7 mg/mL cTnI in 2 M KCl subphase.

A more appropriate way to study the interaction between mab 560 and cTnI is to form a monolayer of mab 560 and inject underneath a certain amount of cTnI. As the molecular area is kept constant an increase in the surface pressure could account for the binding of cTnI from solution to mab 560 at the interface. Figure 5.12 shows the result of such an experiment. A monolayer of mab 560 was formed and compressed to 5 mN/m on 2M KCl, and the surface pressure was kept constant for about 2700 s before injecting the

cTnI. The target surface pressure of 5 mN/m was chosen because it offers sufficient packing of the mab 560 monolayer. But also, the monolayer is loose enough to allow its penentration by cTnI molecules to bind to mab 560. Literature data suggests that if the surface pressure is too high, the additional increase upon binding could limit the amount of protein bound, as above a certain limit (15 to 30 mN/m) the rest of the bound proteins could be squeezed out from the monolayer.[106]

As soon as 15 μL of cTnI 0.7 mg/mL in PBS was injected underneath the mab 560 monolayer, the surface pressure started to rise. After 150 s the monolayer reached a saturation surface pressure of 8.3 mN/m. At first glance, 150 s seems too short to allow all cTnI molecules to reach the mab 560 monolayer.

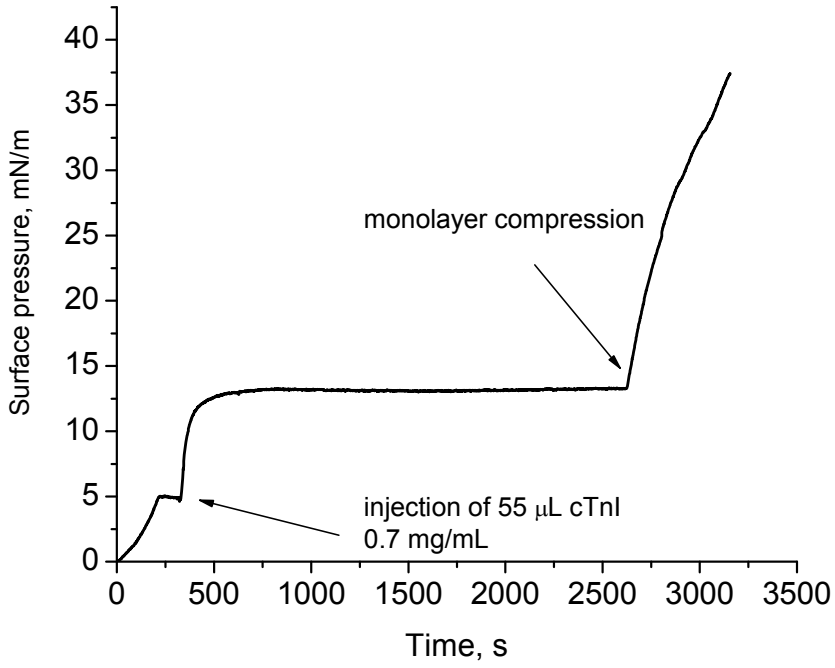

Figure 5.13. Surface pressure vs. time for mab 560 Langmuir film prior and after injection of 55 μL 0.7 mg/mL cTnI in 2 M KCl subphase.

The measurement was repeated using 55 μL 0.7 mg/mL cTnI. The result is shown in Figure 5.13. Compared to the first measurement (Figure 5.12), the time at which the surface pressure was kept at 5 mN/m was reduced from 2700 to 100 s. The surface pressure started to increase as soon as cTnI was injected. The saturation surface pressure was reached for this case in about 400 s compared to 150 s needed when only 15 μL were injected. Also the saturation surface pressure was 13.25 mN/m compared to the previous case of 8.3 mN/m. After the saturation surface pressure was reached, the surface pressure stayed constant over a period of about 2000 s (Figure 5.13). Whereas in the previous case (Figure 5.12), the saturation surface pressure started to decrease monotonically in a similar manner as before cTnI injection.

From these two measurements, two observations can be made: (i) An increased amount of cTnI injected leads to an increase in the surface pressure and stabilizes the mab 560 monolayer. (ii) based on the literature the time needed for a protein to saturate a phospholipid monolayer is anywhere between 40 min and a few hours, depending on the size of the protein and the type of phospholipid.[107]

This approach was shown not to be feasible. All cTnI molecules go to the interface and is practically impossible to quantify any binding between mab 560 and cTnI due to the high salt concentration (2M KCl) in the subphase. Therefore, the author decided to have a closer look at the surface chemistry of cTnI. Obtaining all the surface chemistry and spectroscopy data for the cTnI monolayer, which could prove to be useful in eventually detecting it. This investigation is described in the pages that follow.

5.3 Surface Chemistry of cTnI

5.3.1 Background

One of the *holy grails* of the modern diagnostics is the search for an early biomarker capable of predicting and confirming the hearth attact (i.e., myocardial infarction). Since the redefinition of the diagnostic criteria of myocardial infarction (MI) in 2000, the cardiac troponins (cTns) have been regarded as the preferred biomarkers in the diagnosis of MI[108]. The new universal redefinition of MI strongly prefers cTn as a marker of choice in the diagnosis of MI[109]. The highly specific cardiac troponins also have prognostic value, and they have been given a central therapy-driving role in the management of acute coronary syndromes (ACSs)[110]. It is widely known that measurable cTn levels only appear in the bloodstream 3 – 6 h after the initiation of the MI process[111]. It was shown previously that the detection of the human cardiac troponin I (cTnI) is sufficient in the diagnosis of MI[112]. In muscle tissue, cTnI forms a complex with two proteins, which are components of the troponin complex – troponin T and troponin C[113,114]. Troponin I, in normal cells, is non-covalently attached with actin as a part of the myofilaments. During cell damage and death during an MI episode, cTnI is released and its concentration increases in the circulating blood plasma. By detecting its presence we can detect the onset of the MI. Whereas cTnI in normal cells functions as a surface bound protein and in the disease state (MI) is found in solution, its surface chemistry properties have been, as of today, largely unknown.

One of the best ways to understand the interactions of surface proteins with their membrane and subphase environment is to study their air-water behavior by using the Langmuir film technique[1,115]. This well established technique allows us to produce the

one molecule thick monolayer of proteins and to study its transformation on the air-water interface from gaseous phase, through the liquid expanded and finally liquid condensed phase where usually a protein monolayer collapses. Much useful information can be derived from measurements of the average molecular area and surface potential, such as protein packing and preliminary conformation studies by controlling the surface pressure. Further information can be obtained by performing additional spectroscopic and microscopic studies of the monolayer at different surface pressures.

Because the cTnI protein is mainly found complexed with actin in the myofilaments (with much smaller concentration in a cytoplasm),[116,117] it is expected that its function is greatly influenced by surface interactions between hydrophobic and hydrophilic areas of the complex filament and other cytoplasmic components and that during the process of muscular contraction the troponin is exposed to a range of different surface pressures. This fact makes cTnI a surface protein, which lead the author to investigate its interfacial properties in terms of surface chemistry and spectroscopy.

In this work, the author utilizes the Langmuir monolayer film technique to learn basic surface chemistry properties and to investigate the behavior of cTnI at the air-water interface at various surface pressures that correspond to different states, ranging from gaseous to liquid compressed phase. Another reason to study the Langmuir film properties of cTnI is to explore its stability and to set fundamental assumptions for future development of a thin-film based competitive binding cTnI biosensor.

5.3.2 Surface Pressure-Area Isotherm

In order to obtain the optimal conditions for a stable Langmuir monolayer of cTnI, we first used ultrapure water as subphase. For this purpose, a solution of 0.7

mg/mL cTnI in PBS buffer (pH 7.4) was spread on the water surface. After allowing 10 min for equilibration, the monolayer was compressed at a rate of 10 mm/min.

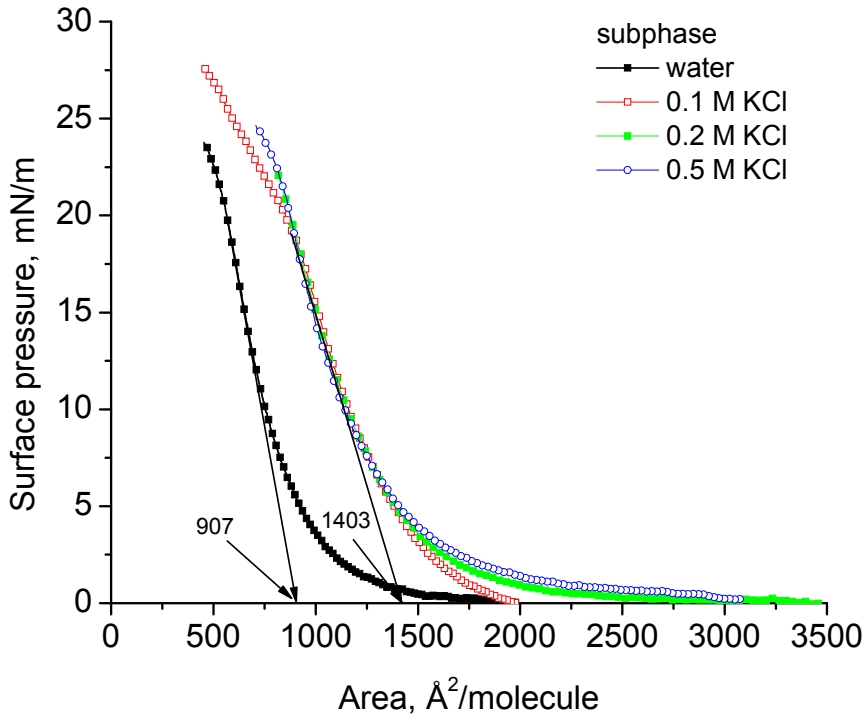

Figure 5.14. Surface pressure−area isotherms for 0.7 mg/mL cTnI as a function of KCl concentration in the subphase.

As shown in Figure 5.14, the surface pressure had a lift point around 1750 $Å^2$/molecule on pure water subphase. Further compression allows the acquisition of the complete surface pressure-area isotherm. The extrapolation of the linear portion of the plot gives a limiting molecular area of about 907 $Å^2$/molecule. The monolayer collapse is not very clear but can be estimated from the change in curvature after the linear portion of the plot to be at around 22-23 mN/m. Because the cTnI protein is water soluble we decided to change the ionic strength of the subphase in order to maximize the number of cTnI

molecules at the air-water interface. For this purpose, the author prepared a set of KCl solutions with concentrations of 0.1, 0.2 and 0.5 M.

As it can be seen from Figure 5.14, all three concentrations of KCl present in the subphase show a shift in the surface pressure-area isotherm towards higher molecular area compared to the pure water subphase, which means that more cTnI molecules are present at the air-water interface. Even though the surface pressure-area isotherms on KCl subphases show different lift points, their limiting molecular area was virtually the same and had a value around 1403 $Å^2$/molecule. The monolayer collapse can be estimated to be between 20 and 25 mN/m.

From the significant increase in the limiting molecular area, it is clear that in the case of the water subphase a large amount of the cTnI molecules were solubilized in the subphase due to the low ionic strength of the subphase.

Due to the fact that all three different concentrations of KCl give similar limiting molecular areas, we decided to perform the rest of the measurements using as subphase a 0.2 M KCl solution. The choice of this concentration was solely based on the author's decision.

5.3.3 Surface Potential-Area Isotherm

The surface pressure-area isotherm was correlated with the surface potential-area isotherm by measuring both isotherms simultaneously. In Figure 5.15, we show the surface pressure- and surface potential-area isotherms of cTnI spread on 0.2 M KCl. Whereas the surface pressure-area isotherm is similar to the one shown in Figure 5.14, more information can be extracted from the surface potential measurements. It is well known that surface pressure measures mainly the interactions between molecules in close

contact (usually van der Waals interactions), whereas the surface potential measures interactions at much longer distances (i.e. dipole-dipole interactions). As expected, the surface potential-area isotherm shows an increase in the surface potential as soon as the compression of the monolayer is started (Figure 5.15).

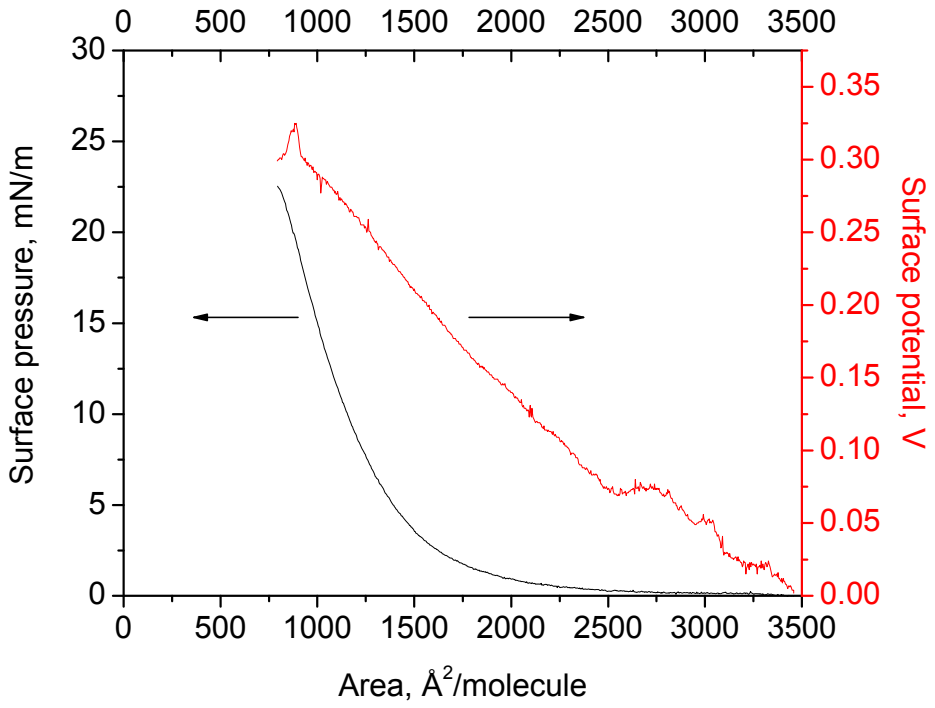

Figure 5.15. Surface pressure−area (—) and surface potential−area (—) isotherms for 0.7 mg/L cTnI spread on the 0.2 M KCl subphase.

This can be explained by the charges present on the cTnI protein. When the surface pressure is still nil we can see an increase in the surface potential. The small bumps are due to cTnI molecules moving rapidly on the subphase surface under the vibrating electrode at nil or very low surface pressures. When the surface pressure starts to increase, an increase in the surface potential can be seen. This increase is smooth until the monolayer collapses. Although, from the surface pressure-area isotherm, the monolayer collapse cannot be readily determined, the surface potential-area isotherm is more

sensitive and the collapse can be estimated to be from the abrupt change observed in the surface potential about 20 mN/m.The theoretical pI of 9.87, was predicted from its amino acid sequence[118] and calculated using the *compute pI/MW* tool available on the ExPASy server.[119] From the calculation it is shown that cTnI has an excess of positive charges, a total of 48 positively charged residues (Arg + Lys) compared to 34 negatively charged residues (Asp + Glu). Due to this fact, the cTnI molecules should repel each other when the monolayer is compressed. If our assumption is correct, then the cTnI monolayer should not form aggregates based on the coulombic repulsion between the molecules.

5.3.4 Compression-Decompression Isotherm

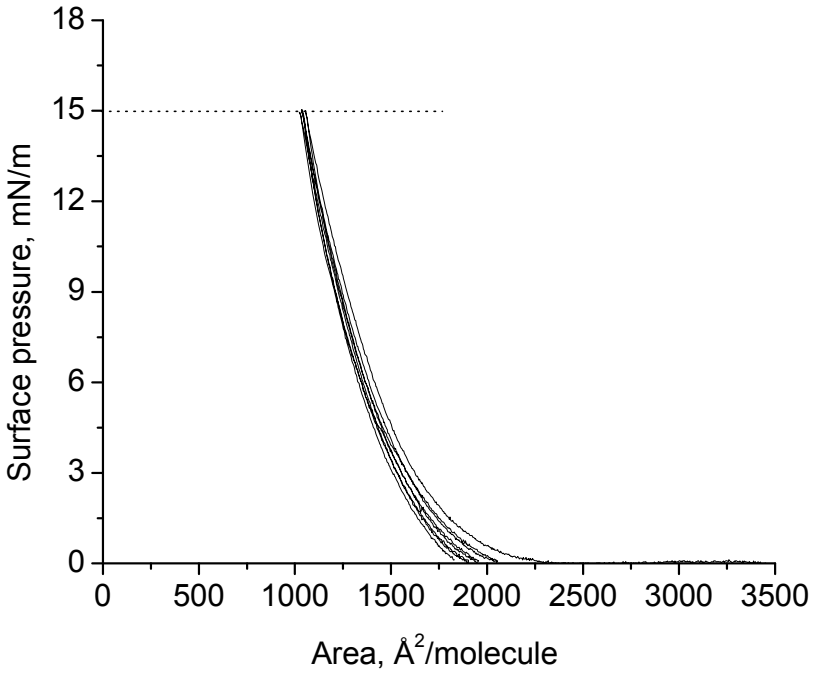

Figure 5.16. Compression−decompression cycles for the 0.7 mg/mL cTnI Langmuir monolayer between 0 and 15 mN/m on the 0.2 M KCl subphase.

Figure 5.16 shows that the cTnI monolayer was compressed four times, up to a surface pressure of 15 mN/m, but no significant changes in the surface pressure-area

isotherm were observed. The lack of hysteresis in the compression-decompression cycles is direct proof that the monolayer does not form aggregates at the air-subphase interface. So far, we have shown that the Langmuir monolayer was more stable when cTnI was spread on KCl subphase than when the subphase was pure water, and the reproducibility of the surface pressure-area isotherms was excellent even if different concentrations of KCl solution were used as subphase. To further investigate this effect, we decided to compress the cTnI monolayer to a surface pressure of 15 mN/m, keep the surface pressure constant over an extended period of time, and follow the decrease in the molecular area.

The result of this experiment is presented in Figure 5.17. When the cTnI Langmuir monolayer was compressed from 0 to 15 mN/m, the area decreased similarly to the surface pressure-area isotherm. The surface pressure was then kept constant after it reached the value of 15 mN/m. As can be seen from Figure 5.17, over a time period of 5,000 s, the molecular area decreased only 170 $Å^2$/molecule (a decrease of about 10%). The small decrease in the molecular area is a proof that cTnI forms a very stable monolayer when spread on the surface of a 0.2 M KCl solution. The results presented in Figures 5.16 and 5.17 are important for two reasons: (i) to make sure that the monolayer was not aggregating and did not solubilize in the subphase; (ii) to make sure that the monolayer did not denaturate during the experiment.

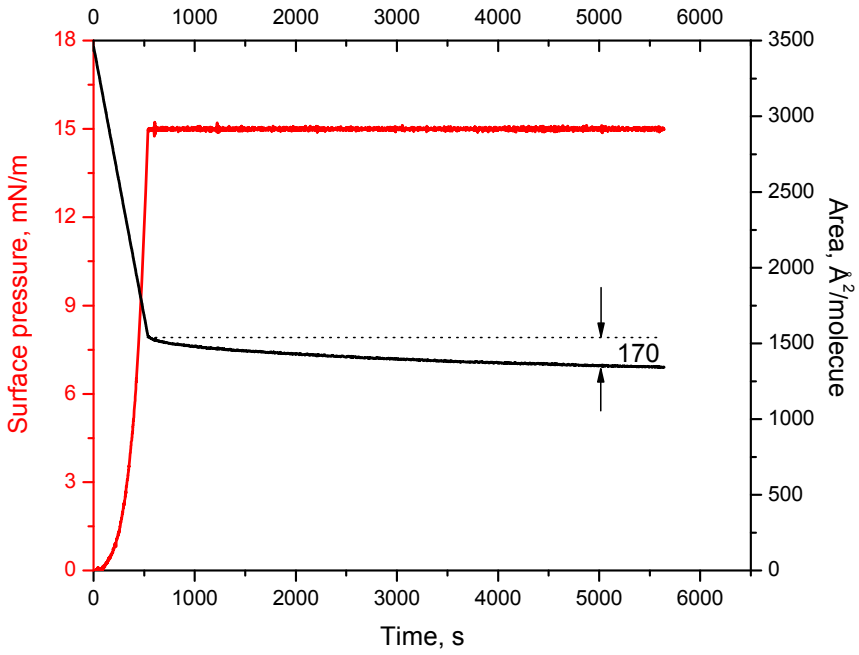

Figure 5.17. Stability measurement showing the decrease in area (—) when the Langmuir monolayer of 0.7 mg/mL cTnI was compressed up to 15 mN/m and kept constant (—) for more than 5500 s on the 0.2 M KCl subphase.

To further confirm the stability of the monolayer and to verify the integrity of cTnI secondary structure (lack of denaturation), we have performed infrared reflection-absorption spectroscopy directly at the air-subphase interface.

5.3.5 Infrared Spectroscopy

5.3.5.1 Infrared Reflection-Absorption Spectroscopy

The infrared reflection-absorption spectra (IRRAS) are presented in Figure 5.18. Different spectra were collected as a function of incident angle at a surface pressure of 20 mN/m. As shown, at angles below the Brewster angle of water (53.12°) the amide I (1600-1700 cm^{-1}) and amide II bands were negative (1500-1600 cm^{-1}), whereas at angles above the Brewster angle of water, the bands became positive[15,83]. This behavior is typical for molecules lying flat on the subphase (parallel to the air-subphase interface).

For each spectrum the background was taken as the 0.2 M KCl solution subphase in the absence of the monolayer. There was no change in the secondary structure of cTnI during monolayer compression. All bands maintain their positions and were increasing in intensity under increased surface pressure.This is due to an increase of the surface density of cTnI molecules per unit area when the monolayer was compressed, which translated to a higher signal.

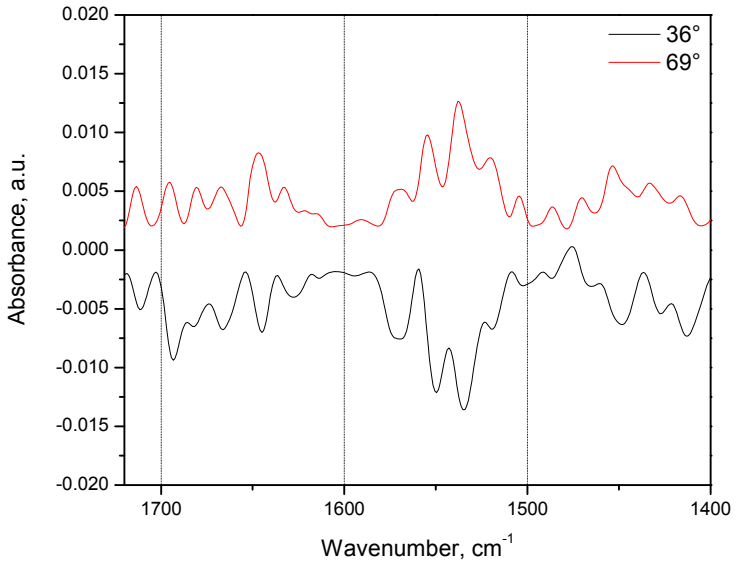

Figure 5.18. IRRAS spectra for 0.7 mg/mL cTnI spread at the air−subphase interface as a function of the incident angle (surface pressure fixed at 20 mN/m). Spectra were acquired using p-polarized light on the 0.2 M KCl subphase.

The spectral region shown can be divided into three main regions as follows: (i) amide I between 1700 and 1600 cm^{-1}; (ii) amide II between 1600 and 1500 cm^{-1}; and (iii) 1500 and 1400 cm^{-1} where the bending modes of the aliphatic C-H bands appear. Methylene (CH_2) bands are present in the side chains of the amino acids constituting cTnI.

As it can be seen from Figures 5.18, in the amide I region the most prominent band is centered at 1647 cm^{-1} assigned to α-helix (band assignments in Table 1). There are some

shoulders present around 1634 and 1621 cm^{-1} that correspond to anti-parallel and parallel β-sheets and the band at 1681 and 1667 cm^{-1} typical of β-turn and β-sheet, respectively. The secondary structure obtained at the air-subphase interface was in good agreement with the published results on the solution secondary structure of cTnI, which confirms that the main structure of cTnI is formed of 4 α-helices and a small amount of β-sheets or turns. It must be noted that at the air-solution interface, by compression, we generated a certain amount of β-sheets that are not present in solution due to side interactions between the α-helices and β-turns or coils of the cTnI molecules. A detailed description of all bands between 1700 and 1400 cm^{-1} is given in Table 1. The assignment for the amide I bands was straightforward, while the amide II raised problems in band assignments due to a strong interaction with the side chains of the amino acids. The side chain region shows an overlap of multiple different vibrations bands that are mainly due to bending and scissoring modes of C-H, CH_2 and to a lesser extent to C-C and C-N bending modes.

Amide I (1700-1600)		**Amide II (1600-1500)**		**Side chains (1500-1400)**	
Assignment	*Band position (cm^{-1})*	*Assignment*	*Band position (cm^{-1})*	*Assignment*	*Band position (cm^{-1})*
ν(CO)	1695	Hard to properly assign bands due to a strong interaction with the side chains	1569	Mainly due to δ(CH) present in the side chains. Some ν(CC) and ν(CN) appear, which further complicates the spectrum	1487
β-turn	1681		1555		1471
β-sheet	1667		1537		1453
α-helix	1647		1521		1453
anti-parallel β-sheet	1634		1505		1433
parallel β-sheet	1621				1417

Table 1. Secondary structure assignment for cTnI.

5.3.5.2 Bio-ATR Infrared Spectroscopy

Using a Bio-ATR accessory to determine the solution ATR-FTIR spectrum of cTnI, we were also able to correlate the secondary structure of the cTnI monolayer with the solution ATR as shown in Figure 5.19. This result confirms, by using a different technique, that the secondary structure of cTnI was mainly α-helical. The main differences are that in the amide I region a major band centered at 1651 cm^{-1} characteristic of α-helix, the amide II region has a single band centered at 1547 cm^{-1}. For the side chain region, a single combination band centered at 1454 cm^{-1} is due to the overlap in the spectrum of the different bending and scissoring modes.

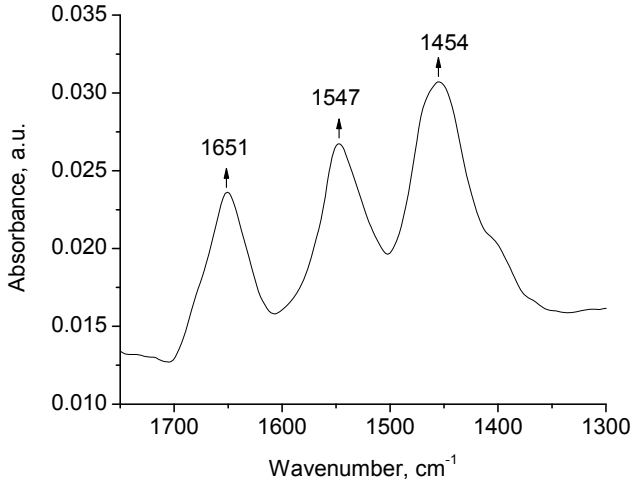

Figure 5.19. Bio-ATR of cTnI (0.7 mg/mL) in PBS buffer.

5.3.6 Brewster Angle Microscopy

The lack of hysteresis was interpreted as a lack of aggregate formation. In order to visually investigate this finding, we decided to use Brewster Angle Microscopy. In Figure 5.20 are shown the micrographs obtained during compression and decompression of the cTnI Langmuir monolayer. Figure 5.20A shows a micrograph obtained at a surface pressure of 1 mN/m that does not show any aggregate or domain formation. This is

interpreted based on the homogeneity of the BAM micrograph. Further compression of the monolayer up to a surface pressure of 15 mN/m (Figure 5.20B) showed a very similar micrograph to the one obtained in Figure 5.20A without any domain formation. The BAM micrograph obtained during decompression of the Langmuir monolayer to a surface pressure of 2.5 mN/m is shown in Figure 5.20C. These micrographs support the conclusion drawn previously that cTnI does not aggregate during compression-decompression cycles of the Langmuir monolayer. The lack of contrast in the BAM micrographs, as well as the very low intensities in the IRRAS spectra, are indicative of a molecular orientation in which the α-helices are lying flat on the water surface, which provide a low reflectivity related to the monolayer thickness and refractive index.

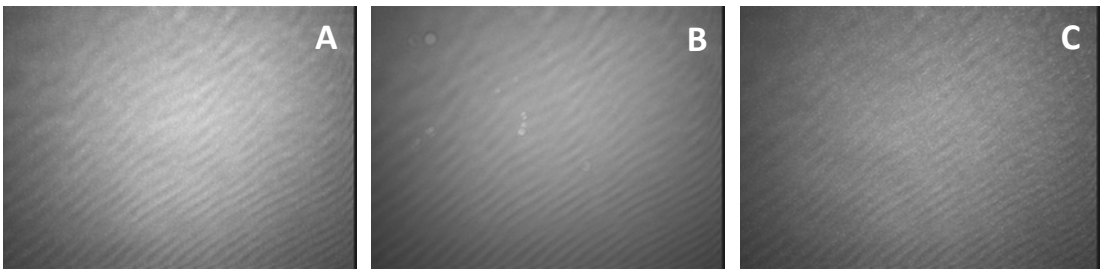

Figure 5.20. Brewster angle micrographs for cTnI spread on the 0.2 M KCl subphase for different surface pressures during compression, (A) 1 and (B) 15 mN/m, and decompression, (C) 2.5 mN/m (image size 200 μm × 200 μm).

To further confirm these findings, we have labeled the cTnI protein with fluorescein isothiocyanate, a commonly used fluorescent label for proteins.

5.3.7 Protein Labeling with FITC

5.3.7.1 Surface Pressure-Area Isotherm

The first observation arises from the surface pressure-area isotherm of cTnI-FITC. The new limiting molecular area is 1680 $Å^2$/molecule for cTnI-FITC compared to 1403 $Å^2$/molecule obtained for cTnI without the fluorescent label (as shown in Figure 5.21).

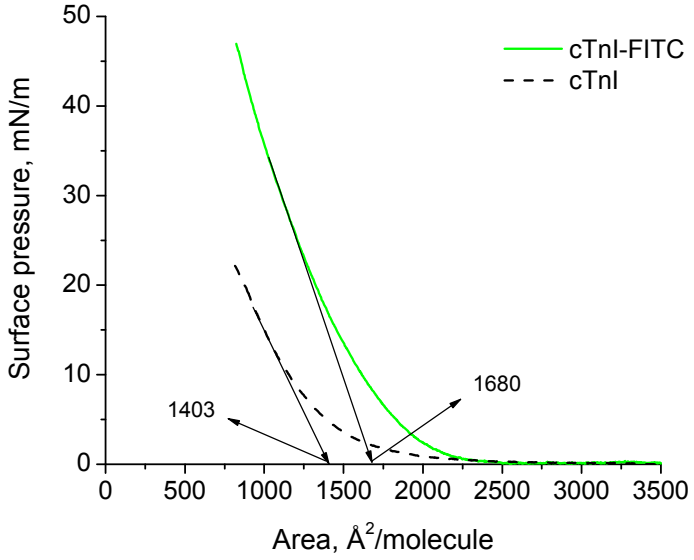

Figure 5.21. Surface pressure−area isotherm of 0.6 mg/mL cTnI-FITC spread on 0.2 M KCl.

Because the limiting molecular area is independent of the concentration used for spreading or the volume spread, we can confidently state that the increase in the limiting molecular area is due to the presence of the fluorescent label. Previously, we have determined the limiting molecular area of an FITC derivative, namely 5-octadecanoyl aminofluorescein (ODFL)[4], and we have obtained a limiting molecular area for this derivative of 64 $Å^2$/molecule. The difference in the limiting molecular areas is 277 $Å^2$/molecule, which allows the determination of the number of FITC moieties per cTnI molecule. Based on this calculation the average number of FITC groups is 4.33 for each cTnI molecule. The *classical* approach to calculate the number of FITC groups per protein is not applicable because the number of amino acids present in the structure of cTnI that are responsible for the absorption band at 280 nm are scarce. Due to this reason the calculation of the ratio of A_{495}: A_{280}, is practically undeterminable at the air-subphase

interface as will be shown in the next results concerning UV-vis absorption at the air-subphase interface.

5.3.7.2 In situ UV-vis at the Air-water Interface

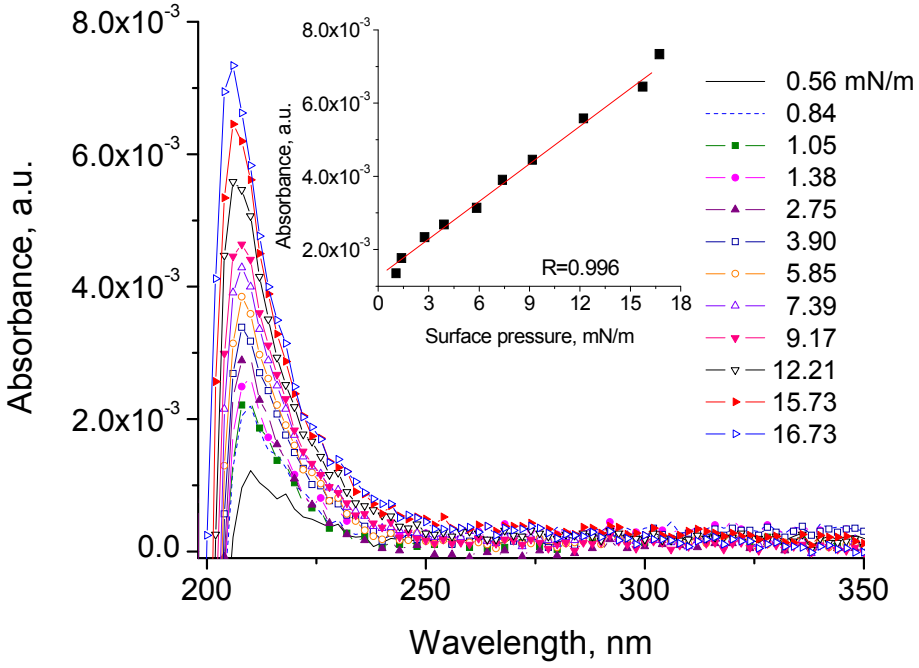

Figure 5.22. Absorbance at the air−subphase interface for 0.6 mg/mL cTnI spread on 0.2 M KCl as a function of surface pressure. (Inset) Absorbance maxima at 206 nm as a function of surface pressure.

As shown in Figure 5.22, the cTnI does not present any significant absorbance other than the peptide bonds present in the protein located at 206 nm. The inset shows the linear relationship between the absorbance peak at 206 nm and the surface pressure. The linear dependence is a proof that during compression the surface density is increasing linearly, which in turn means that no aggregation is occurring. The first point on the inset deviates from linearity due to the fast movement of the cTnI molecules on the subphase surface, whereas the deviation from linearity of the highest two points are due to the

Langmuir monolayer collapse. To have other proof than the peptide absorption peak, we have used the FITC labeled cTnI. Figure 5.23 shows the major absorption bands consequently assigned to FITC. The absorption bands are located at 460 and 484 nm, respectively. Based on the absorption spectra at the air-subphase interface, an excitation wavelength of 484 nm was selected for the fluorescence measurements of cTnI-FITC. The inset in Figure 5.23 shows the linearity of the absorption band at 484 nm as a function of surface pressure. Based on the linearity of the plot, it is clear that cTnI-FITC does not aggregate at the air-subphase interface.

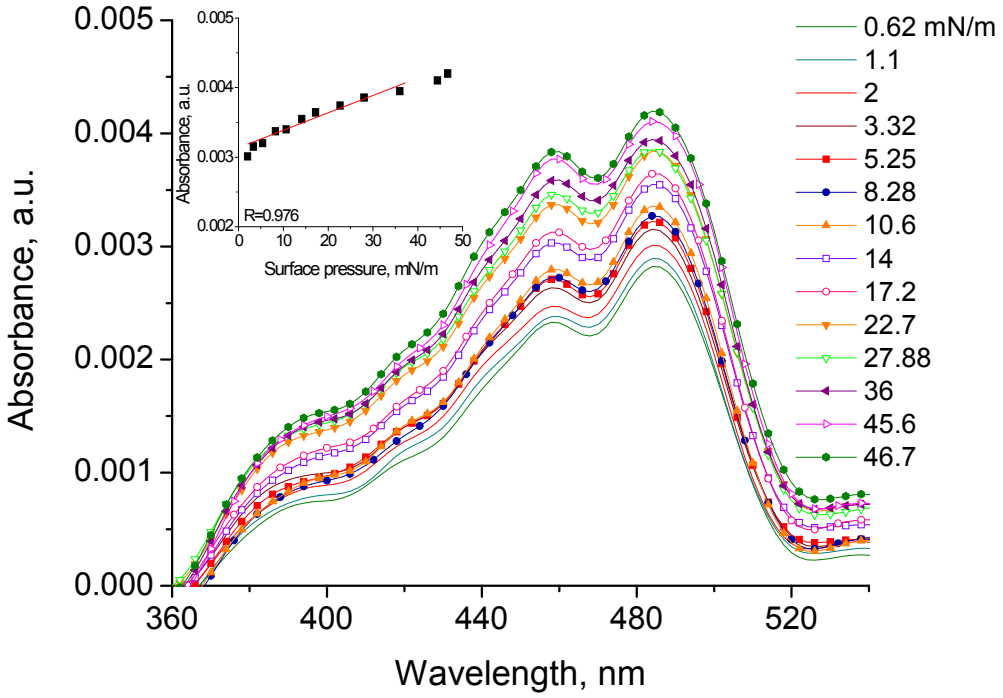

Figure 5.23. Absorbance at the air-subphase interface of cTnI-FITC spread on 0.2 M KCl as a function of surface pressure. (Inset) Absorbance at λ_{max} = 484 nm as a function of surface pressure.

5.3.7.3 In situ Fluorescence at the Air-water Interface

The fluorescence spectra obtained as a function of surface pressure at the air-subphase interface when cTnI-FITC was spread on the surface on a 0.2 M KCl solution is shown in Figure 5.24. The fluorescence maximum is located at 515 nm, which is the proper emission position taking into account the polarity of FITC. Plotting the emission maxima as a function of surface pressure reveals that the fluorescence is increasing as a function of surface pressure up to 15 mN/m (increased surface density during compression), followed by self-quenching of the FITC fluorescence (inset in Figure 5.24). This occurs when the cTnI-FITC intermolecular distances are reduced during compression.

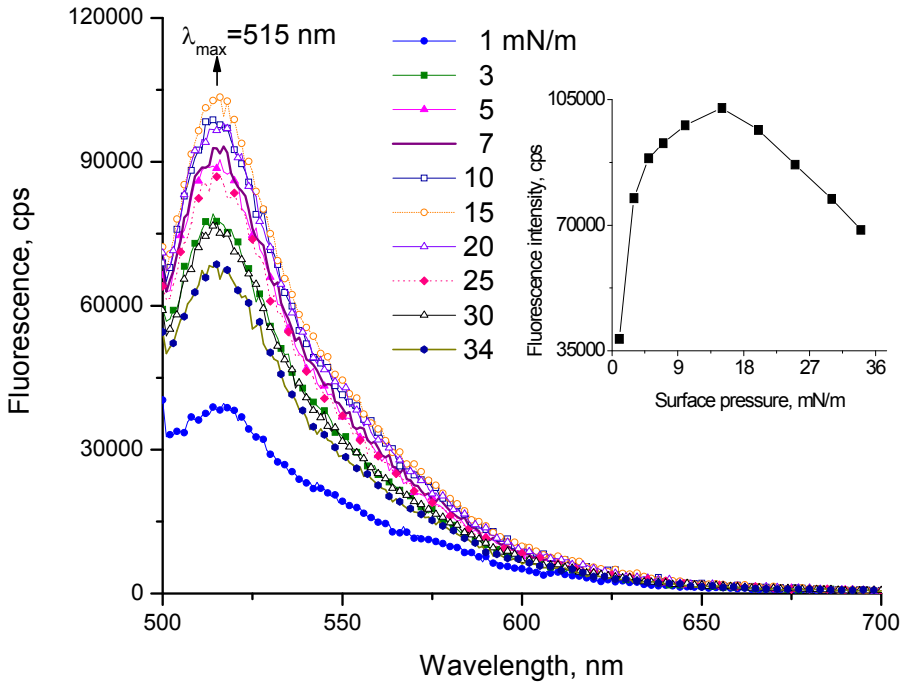

Figure 5.24. Fluorescence spectra of cTnI-FITC spread at the air-subphase interface on 0.2 M KCl as a function of surface pressure. (Inset) Fluorescence intensity at λ_{max} = 515 nm as a function of surface pressure.

5.3.8 Epifluorescence Microscopy

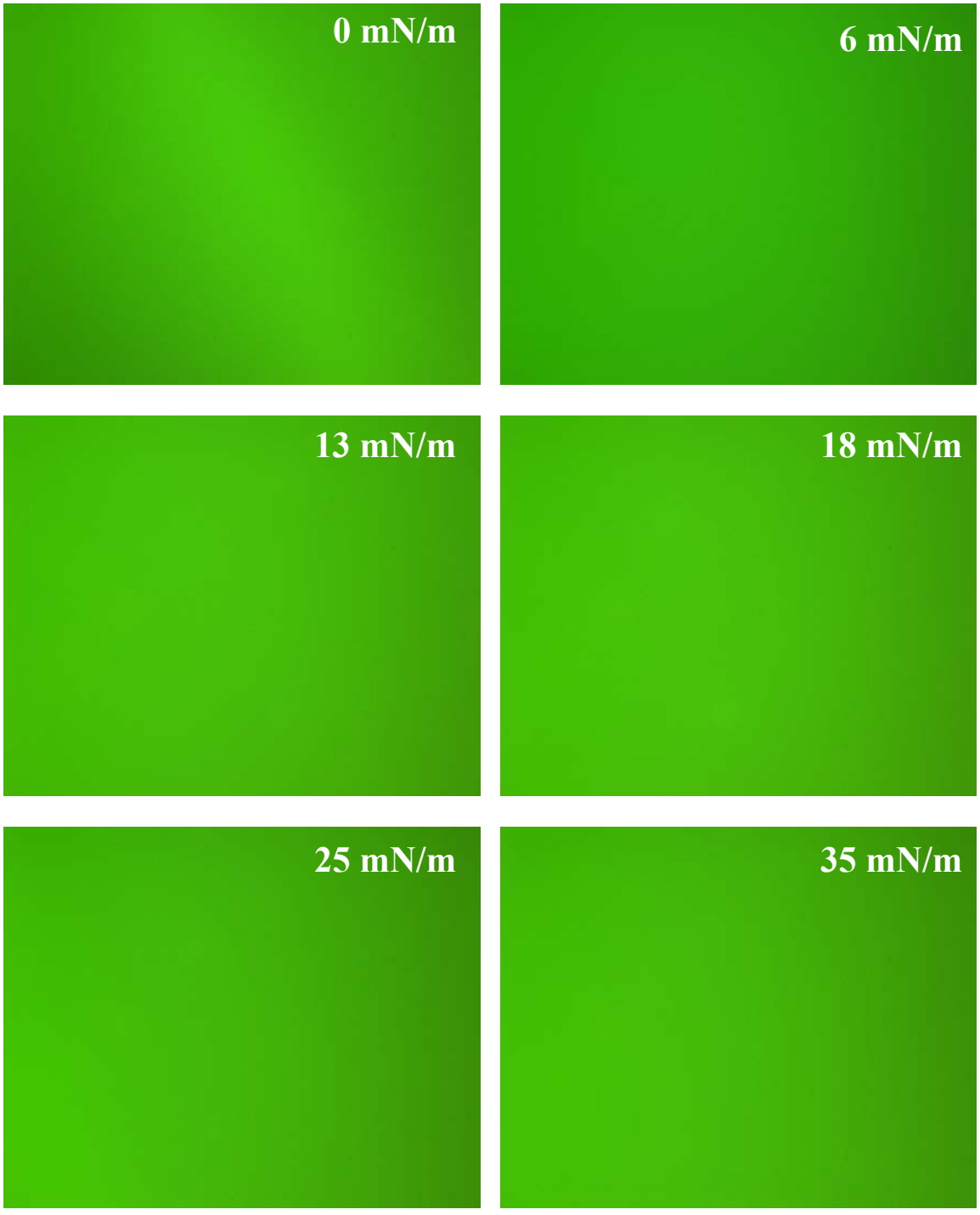

Figure 5.25. Epifluorescence micrographs of cTnI-FITC spread at the air−subphase interface. The micrographs were taken during compression for different surface pressures (image size, 895 μm × 713 μm).

Epifluorescence microscopy was performed directly at the air-subphase interface for 0.6 mg/mL cTnI-FITC on 0.2 KCl solution in order to directly visualize the aggregate formation. As shown in Figure 5.25, regardless of the surface pressure used no visible aggregation can be seen. If aggregates had formed they would have appeared as dark spots[120] surrounded by green areas where no aggregation took place. Even though in Figure 5.24 there is self-quenching of the FITC moieties between cTnI-FITC molecules, this phenomenon is possible without actual aggregation of the FITC labeled protein due to possible dimer formation at high surface density of cTnI-FITC (high surface pressures) that cannot be detected on the μ-scale of the epifluorescence measurements.

These measurements support the results explained in the chapter regarding the lack of aggregation during cTnI monolayer compression.

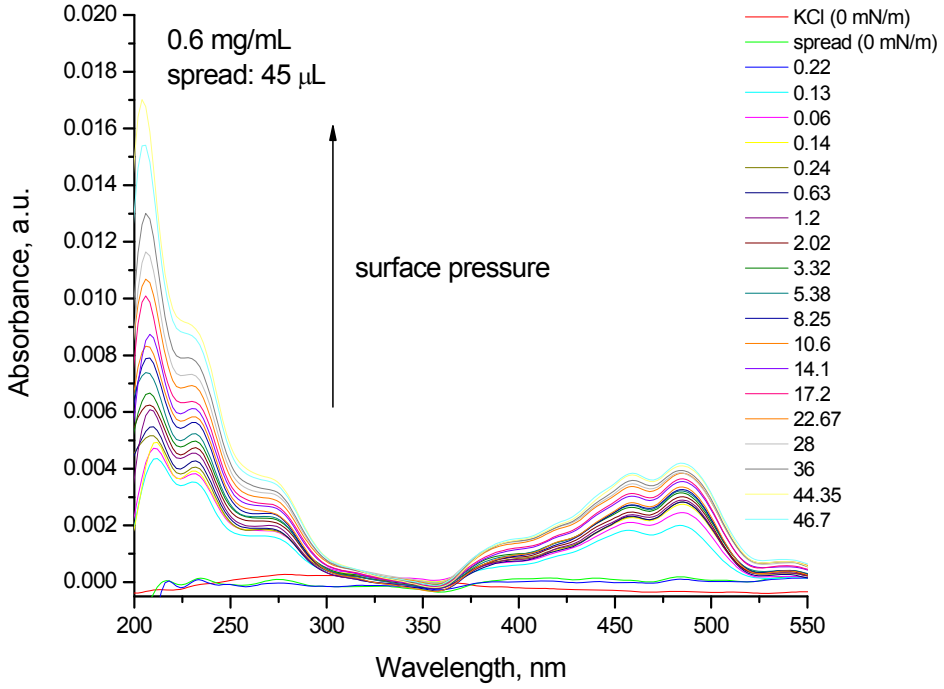

Figure 5.26. Absorbance at the air-subphase interface of cTnI-FITC spread on 0.2 M KCl as a function of surface pressure.

Based on the absorption spectra at the air-subphase interface (Figure 5.26), an excitation wavelength of 484 nm was selected for the fluorescence measurements of cTnI-FITC.

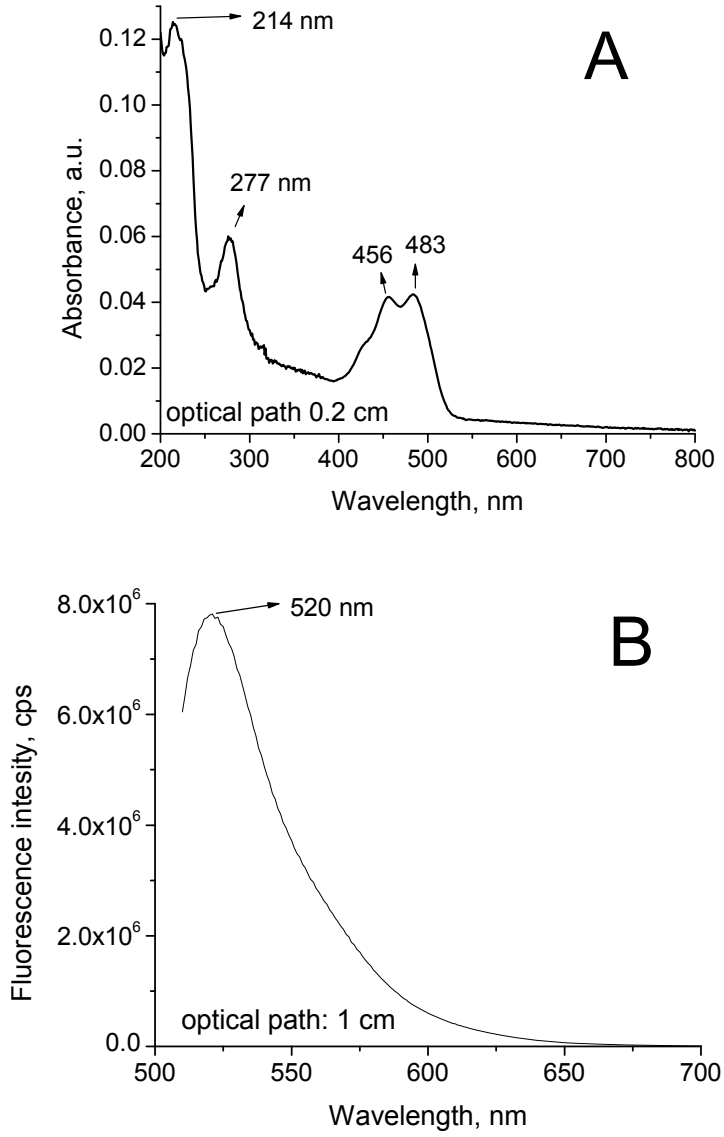

Figure 5.27. Absorbance for FITC (10^{-5} M) (A) and fluorescence for FITC (10^{-7} M) in methanol (B). Optical path length used was 0.2 cm.

Figures 5.27A and 5.27B show the solution absorbance and fluorescence of FITC in methanol. The small differences in absorbance and fluorescence band positions are due to the solvent polarity and changes in microenvironment. It is well known that the more

polar the environment, the more red shifted the bands will appear. In Figure 5.24, the fluorescence maximum is located at 515 nm (less polar microenvironment due to the hydrophobic side chains in cTnI) and in Figure 5.27B is located at 520 nm (in methanol). Comparing Figures 5.23 and 5.27A in terms of absorption on cTnI-FITC at the air-water interface and FITC in methanol, the two spectra look similar. This can be explained by the lack of sensitivity in terms of microenvironment for absorption studies compared to fluorescence studies.

The reason for the difference in the concentration is due to the low absorbance using a 0.2 cm optical path length cuvette. When a 10^{-7} M solution was used, the absorbance was too small to be detected (within noise level). When a concentration of 10^{-5} M FITC was used for fluorescence measurements, this concentration was too high and saturated the detector.

5.4 Bio-ATR spectroscopy of mab 560 and cTnI mixture

We then had a look at the secondary structure of mab 560 and cTnI and their mixture studied by Bio-ATR FTIR.

As shown in Figure 5.28, the measurement of buffer Bio-ATR against buffer yields a flat line. The purpose of this measurement is to assure that the Bio-ATR crystal is clean, but also the single channel buffer spectrum was used as reference for the rest of the measurements. The Bio-ATR spectrum of cTnI (Figure 5.28, red line) shows the typical protein features, amide I (1600 – 1700 cm^{-1}) and amide II (1500 and 1600 cm^{-1}) while the band centered around 1454 cm^{-1} is a combination of the amino acids side chains present in the primary structure of cTnI. In the same figure (blue line) is presented the amide I and II region of mab 560. The main difference compared to cTnI is the lack of

the band attributed to the side chains (1454 cm^{-1}). In the top panel (orange line) is presented the Bio-ATR spectrum of the mixture mab 560 (0.5 mg/mL) : cTnI (0.63 mg/mL). We can clearly see the band at 1454 cm^{-1} attributed to the side chains of cTnI. The amide II band of the mixture is unchanged, as it is present in both proteins.

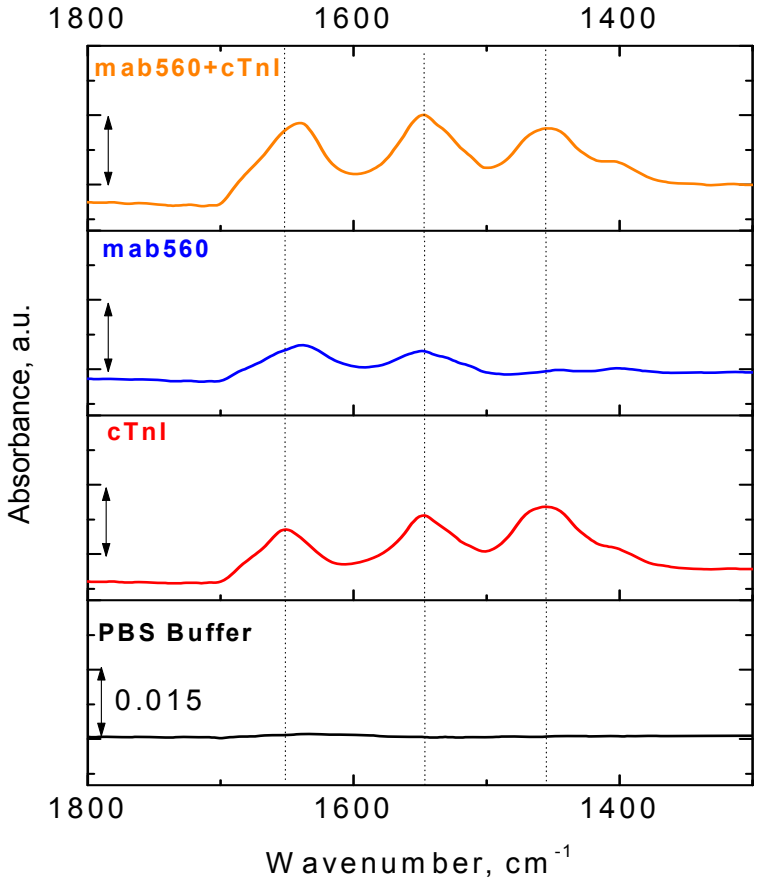

Figure 5.28. Bio-ATR FTIR spectra for the PBS buffer (—), cTnI (—), mab 560 (—) and the mixture (mab 560: cTnI) (—).

There is, however, a small change in the amide I band. For cTnI (red line), the band is centered at 1651 cm^{-1}, typical of an α-helix while for the mab 560, the amide I band (blue line) is centered at 1638 cm^{-1}, which is most probably due to a combination of α-helix (1650 cm^{-1}) and the anti-parallel β-sheet (1630-1640 cm^{-1}) present in the hypervariable

region of the mab 560 binding site. In the mixture (mab 560 : cTnI) the amide I band is centered at 1644 $cm^{-1.}$ This band is simply due to the overlap of the two amide I bands for cTnI and mab560. This was verified by substracting the Bio-ATR spectrum of mab 560 from the mixture. The subtracted graph has the exact band positions as found by measuring the Bio-ATR spectrum of cTnI.

Because of these findings, it can be stated that the binding between cTnI and mab 560 cannot be studied by IR techniques as the conformational changes, if any, are too subtle and small to be detected by IR.

5.5 Conclusions

It was shown that detection of cTnI injected in the subphase by mab 560 spread on the air-solution interface is not possible due to the ionic strength required to obtained a stable Langmuir monolayer of mab 560.

It was shown that cTnI forms a very stable Langmuir monolayer if the ionic strength of the water subphase is increased by addition of KCl. The Langmuir monolayer formed does not lead to domain or aggregate formation, and the secondary structure of cTnI is similar to the one obtained in solution using Bio-ATR FTIR. Based on the limiting molecular area, BAM micrographs and the infrared intensities obtained with p-polarized IRRAS, the molecular orientation is one in which the main component of the secondary structure (i.e. α-helices) lies parallel to the air-subphase interface.

Chapter 6. Detection of cTnI Using Mutant Antibodies

As was discussed in the background section 5.1, monoclonal antibodies show the greatest potential in the detection of cTnI. Whereas the measurements discussed in subchapter 5.1 related to the surface chemistry approach using mab 560, the current approach using a chemically-immobilized antibody involve mab 19C7. The use of mab 19C7 is based on its main used as secondary antibody in a sandwich immunoassay. Whereas mab 19C7 is often used for signaling purposes, there are two immunoassay combinations in which mab 19C7 is actually used as a capture antibody. This exchange of antibodies can be made since each of them binds to a different epitope of cTnI.

6.1 Immobilization Strategies

Surface modification is the most important step in the immobilization of proteins. Encapsulation techniques (sol-gel processes)[121,122] have an advantage in that they allow high loading compared to the flat surfaces.[123,124] The drawbacks are that related to the activity of these types of layers , which depend greatly on the diffusion of analytes to receptors inside the gel.[125] This is reflected in a long response time.[126,127] The surroundings of the biomolecules are important towards adsorption but also denaturation, and nevertheless the film stability and/or leaching. To avoid these inconveniences, chemical attachment on a flat surface emerged as the main choice in surface modification. The chemical attachment should provide (i) immobilized receptors (biomolecules) while their activity is maintained; (ii) the receptors should face the solution; (iii) a low non-specific adsorption of other analytes than the desired one. One other important factor is the stability of the modified surface; therefore covalent bonds are the perfect candidate. The first techniques related to modified surface and

immobilization of a biomolecule that binds a specific recognized molecule from solution was enzyme-linked immunosorbent assay (ELISA).[128]

Most surfaces are initially modified with a linker that posses a suitable group for coupling such as carboxylic (-COOH), hydroxylic (-OH), primary amines ($-NH_2$), thiols (-SH) or epoxides. Between these strategies, the most commonly used is the surface modification with primary amines due to their high reactivity in water and ability to react with isothiocyanates, aldehydes, and activated esters. Whereas the main group to react with the solid substrate, is alkoxysilane. The reaction involves a first step of hydrolysis followed by condensation to form alkylsilanol that can next react with the surface activated hydroxyl groups and release of water molecules.[129-131] Characterization of such derivatized surfaces mainly involves infrared spectroscopy.[130,132-136]

The choice in the silane compound and the concentration used is important but also the solvent used and reaction time,[129,130,134] the nature of the solvent and its water content,[137-139] temperature[129] and time[134,140] are the most important parameters.

Substrate cleaning is extremely important, then choice is a Piranha solution ($H_2SO_{4\ conc}$: H_2O_2 (30% soln), 50:50 v/v) that in addition to cleaning the surface (glass or quartz) increases the surface density of hydroxyl groups. These hydroxyl groups react with the ones from the silanol derivative and high silanol concentration or extensive reaction time could lead to formation of multilayers[141] therefore the solvent, temperature and user expertise are extremely important factors.

In the current research, two of the most common methods for surface modification are investigated using primary amines and thiols.

6.1.1 Isothiocyanate-modified Surface

As shown in Figure 6.1, the first step for immobilization is the surface modification using 3-amino propyl trimethoxysilane. Prior to the surface modification, the quartz slide needs to be cleaned. The quartz slide was placed in a 50 mL beaker containing 20 mL H_2O_2 (30% v/v) and 20 mL concentrated H_2SO_4. The slide was kept in the mixture until no more bubbles (O_2) were formed and the solution cooled down. After this step, the slide was rinsed copiously and then sonicated for 30 min in ultrapure water. The rinsing and sonication steps were repeated three times. In order to have the slide ready for the surface modification, it was dried in oven at 110ºC. The dried slide, cleaned using the Piranha solution, had an increased amount of hydroxyl groups necessary for the reaction with the 3-amino propyl trimethoxysilane. In order to limit the polycondensation of the silane derivative, 0.5 mL of 3-amino propyl silane were dissolved in 40 mL of anhydrous toluene thus giving a 1.25 % (v/v) concentration. In order for the reaction with the surface hydroxyl groups to occur the trimethoxysilane needs to be converted to trihydroxysilanol, therefore water molecules are needed for the hydrolysis of the methoxy groups. The water molecules are provided by the adsorbed water molecules on the hydrophilic glass slide. The hydrophilic slide was placed in the beaker containing 1.25% 3-amino propyl silane in toluene and sonicated for 30 min. After the step, the slide was placed in a beaker containing pure anhydrous toluene and sonicated for another 30 min to remove any physisorbed compound. The sonication step in anhydrous toluene was repeated two more times, and then the slide was placed in the oven for drying and curing at 80ºC.

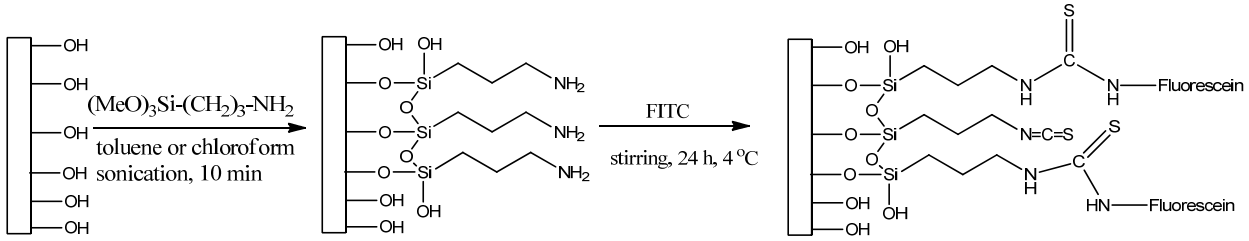

Figure 6.1. Surface modification with 3-amino propyl trimethoxysilane and FITC labeling.

In order to check the presence of the 3-amino propyl group on the surface FTIR (Figure 6.2) that shows the symmetric (2852 cm^{-1}) and asymmetric (2922 cm^{-1}) stretching bands for CH, can be used. The amino group is too weak to be seen in a single monolayer therefore an alternative method was developed.

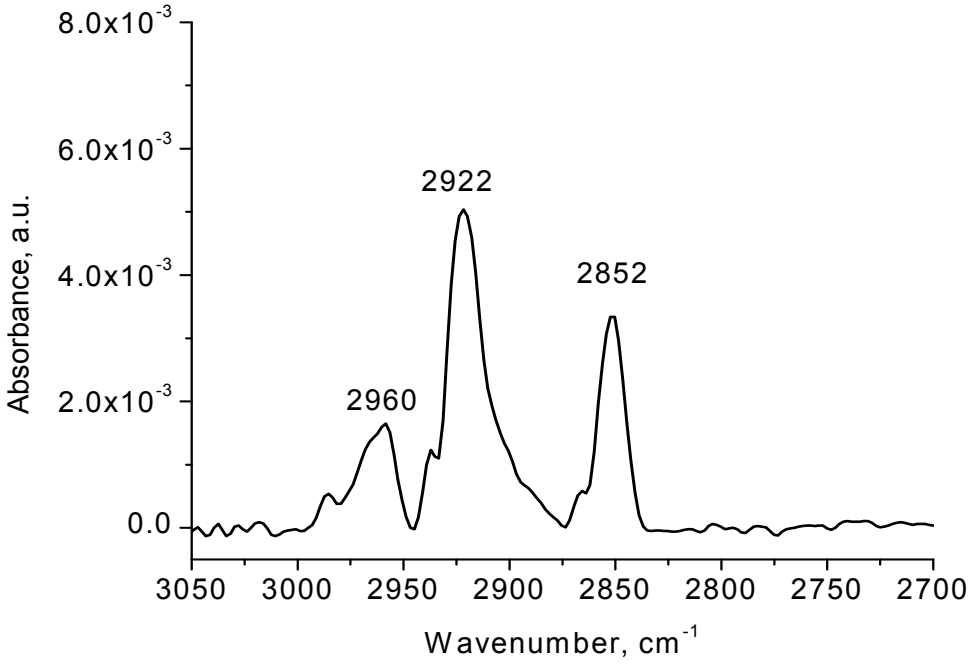

Figure 6.2. ATR-FTIR spectrum of 3-amino propyl-modified slide.

Amino groups can easily react with fluorescein isothiocyanate (FITC) to yield thiourea-like bonds. In order for this reaction to occur, 0.26 mg of FITC were dissolved

in 20 mL PBS buffer, yielding a concentration of 3.38×10^{-5} M solution (MW_{FITC}=389.4). The amino-modified slide was place in this solution and stirred for 13 h at a temperature of 4ºC using the experimental setup shown in Figure 6.3.

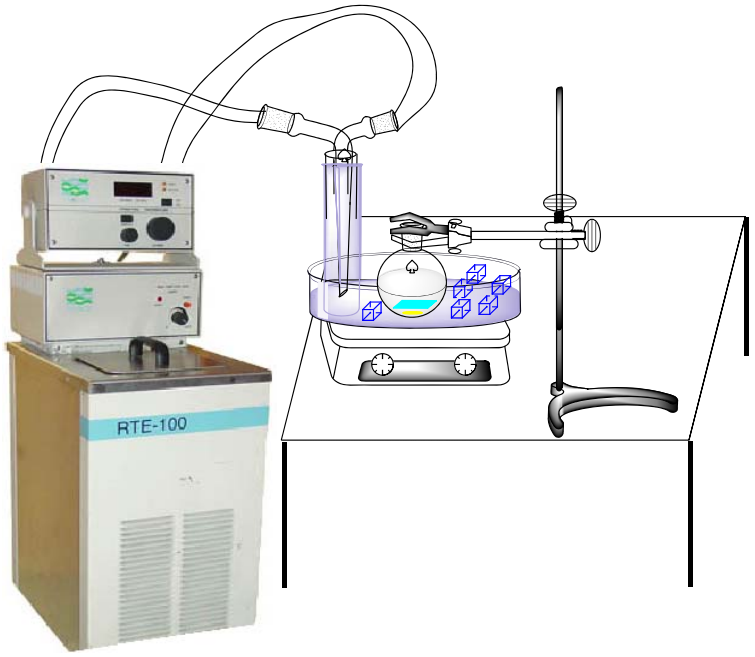

Figure 6.3. Experimental setup for stirring at 4ºC.

A Neslab (model RTE-100) temperature control was connected to a finger condenser placed in a vessel that contains a mixture of water and ice. In the same vessel is placed a round bottom flask that has the FITC solution, amino-modified slide (aqua color) and a stirrer (yellow color). Using a magnetic stirrer the FITC solution is stirred continuously. The Neslab water circulation temperature control was set at 4ºC and to assure that the temperature control, its reservoir was filled with a mixture of water and ice. Experimentally, this was the only setup being able to maintain a constant low temperature. After a time period of 13 h, the slide was removed from the FITC solution and sonicated for 30 min in PBS buffer. The resulted FITC-modified quartz slide was

characaterized using UV-vis and fluorescence spectroscopies and epifluorescence microscopy.

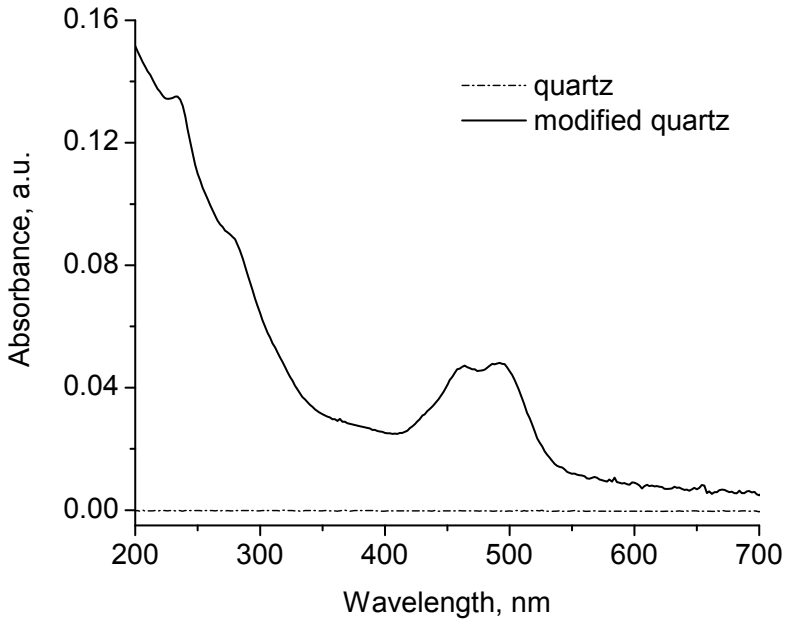

Figure 6.4. Uv-vis spectra of a quartz slide before and after modification with FITC.

Figure 6.4 shows the spectra of a quartz slide prior to the FITC labeling. Basically, the quartz substrate has no absorption in the UV-vis range. Upon modification with FITC, the absorption spectrum of FITC is revealed. The spectrum contains a shoulder around 230 nm typical of conjugated carbon double bonds. A second shoulder around 280 nm which is due to the formation of the thiourea-like bond upon surface attachment and two well defined peaks typical of the main absorption of FITC at 464 and 494 nm. The UV-vis spectra were acquired by placing the slides in the path of the beam of the HP diode array spectrophotometer using the unmodified slide as blank.

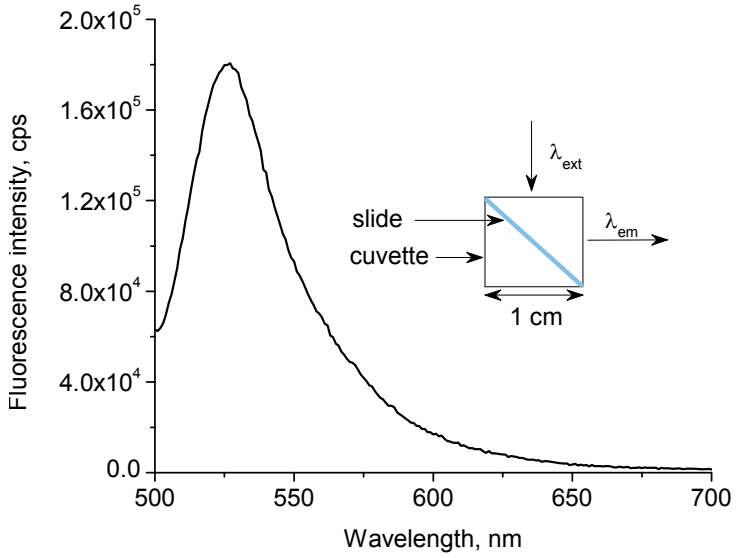

Figure 6.5. Fluorescence spectrum of FITC –modified slide (λ_{ext}= 480 nm).

Figure 6.5 shows the fluorescence spectrum of the FITC-modified slide. For this purpose the modified slide was placed in the cell compartment of the Fluorolog-3 spectrophotometer in a cuvette with 1 cm optical path length. The modified slide fits perfectly in the cuvette at an angle of 45º, which is ideal to obtain the fluorescence of the modified slide. For the UV-vis and fluorescence measurement no solution was used and the slides were blown dry using compressed N_2 gas before the measurements.

Using an excitation wavelength of 480 nm the spectrum shown in Figure 6.5 was obtained. The emission maximum is located at 525 nm typical of fluorescein emission. To be able to visualize the fluorescence, the FITC-modified slide was place in the Olympus IX-FL inverted microscope and the micrograph acquired using blue light for excitation. As shown in Figure 6.6, the epifluorescence micrograph looks very homogeneous. In some places, brighter areas can be seen that are assigned to the formation of salt, from the PBS buffer in which the slide was stored, upon drying.

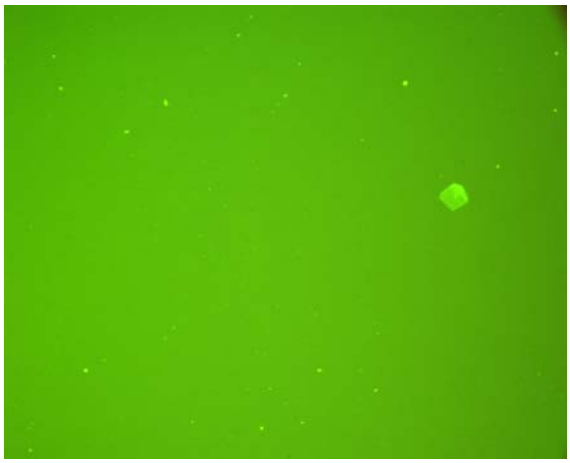

Figure 6.6. Epifluorescence micrograph of FITC-modified slide (895 μm × 713 μm).

With these data in hand, we can be certain that the initial surface modification with 3-amino propyl trimethoxysilane is efficient and that the amino groups are present on the surface of the quartz slide. Figure 6.7 shows the steps required to attach and label the mutant IgG (mab 19C7).

Figure 6.7A shows the prior step previously verified of amine surface modification followed by the conversion of the amine groups to isothiocyanate using diethylthiocarbamoyl chloride (50 mg in 20 mL acetonitrile) using 8 h reflux at 60ºC. The investigation of the surface modification yields the same result as in Figure 6.2 as measured by ATR-FTIR again the isothiocyanate groups present on the surface being too weak to be detected. The next step (Figure 6.7B) involves a similar reaction as the one described in Figure 6.1 (second reaction) an amine (from the mab 19C7) to react with isothiocyanate from the surface (modified quartz). This reaction was carried out at 4ºC using the experimental setup described in Figure 6.3. For this purpose the isothiocyanate slide was placed in a 1 cm cuvette filled with 2 mL of mab 19C7 (0.5 mg/mL in PBS buffer).

The reaction proceeded for 24 h after which the slide was removed and washed with PBS to remove any physisorbed mab. Between measurements the slide was stored in PBS buffer at 4ºC to assure that the secondary structure of mab 19C7 is maintained.

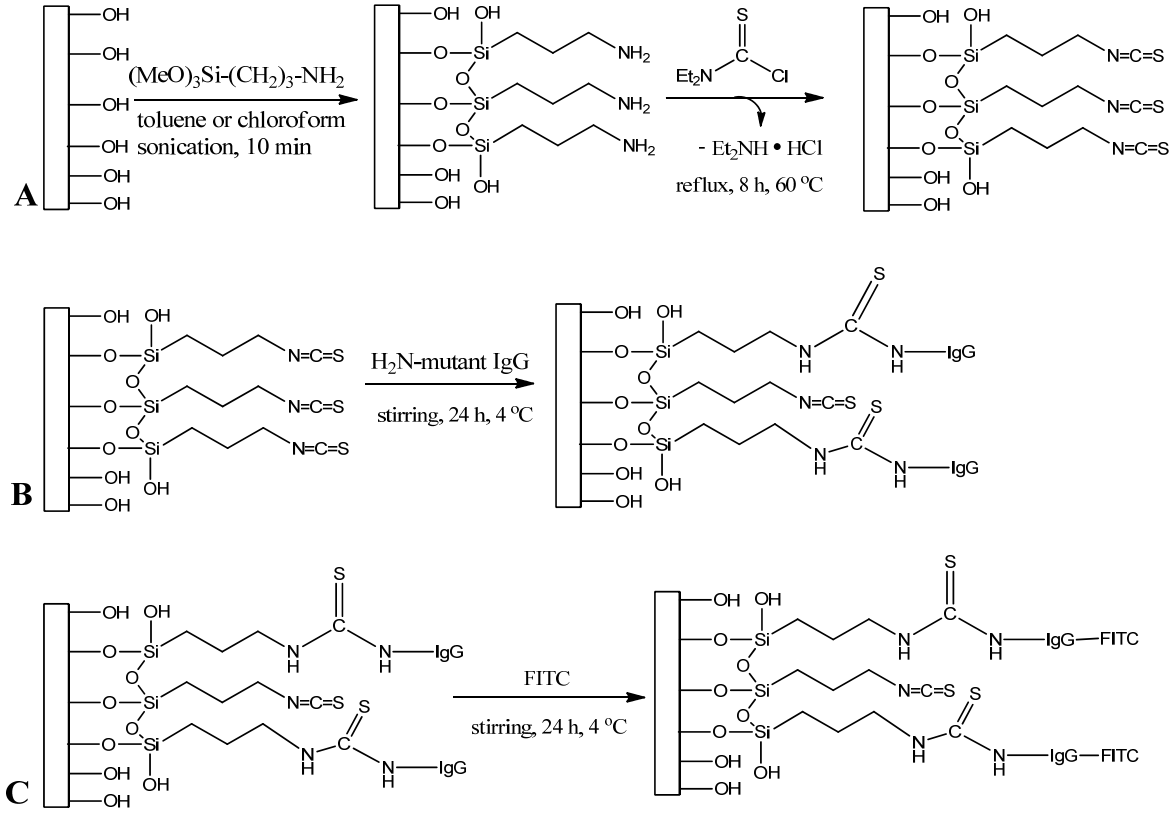

Figure 6.7. Quartz surface modification: amino-modified quartz and conversion to isothiocyanate (A); mutant IgG immobilization (B); IgG labeling with FITC (C).

A convenient method to check for the presence of mab 19C7 on the surface of the quartz slide is the use of fluorescence spectroscopy. Figure 6.8A shows the fluorescence spectrum of the mab 19C7-modified slide after the slide was blown dry using compressed N_2 gas using an excitation wavelength of 280 nm. The tryptophan emission at 350 nm can be easily distinguished.

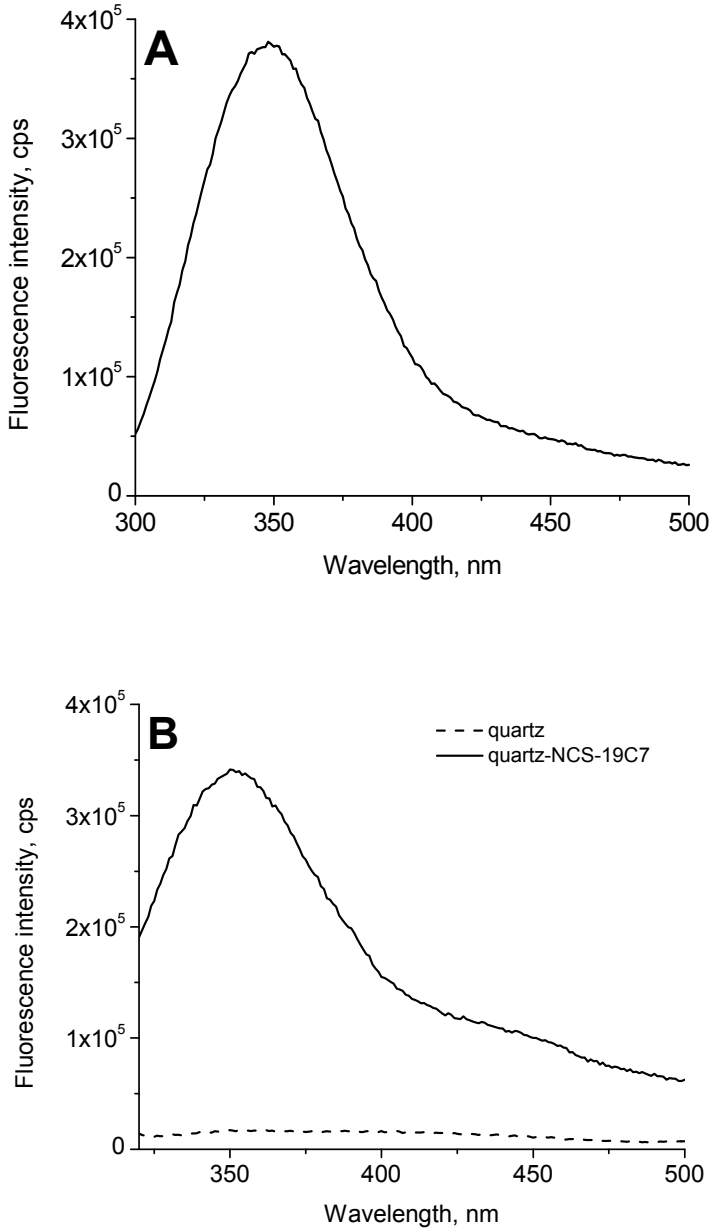

Figure 6.8. Fluorescence of mab 19C7-modified quartz slide in air (**A**) and in PBS buffer (**B**).

Since the measurements to detect cTnI will be performed in PBS buffer it is important to check the fluorescence of the slide in the same PBS buffer. Figure 7.8B shows the same emission originating from the amino acid tryptophan belonging to mab

19C7. For comparison purposes an unmodified slide was placed in the same PBS buffer and its emission verified. Since the unmodified slide does not have any protein therefore tryopophan present, its emission is nil. As shown in Figure 6.8A the fluorescence spectrum in air is measured between 300 and 500 nm, while in Figure 6.8B only the region between 320 and 500 nm is shown.

λ_{ext}	λ_{Raman}
260	285.21
275	303.36
280	309.46
285	315.58
350	397.27

Table 2. Values for the position of the Raman peak depending on the excitation wavelength for water.

This is due to the use of PBS buffer in Figure 6.8B that shows the Raman peak corresponding to water at 309.5 nm (Table 2), which was therefore not included in the fluorescence spectrum. The actual Raman peak of water solution depends on the excitation wavelength according to the equation:[142]

$$\frac{1}{\lambda_{Raman}} = \frac{1}{\lambda_{ext}} - 0.00034 \quad \text{or} \quad \lambda_{Raman} = \frac{\lambda_{ext}}{1 - \lambda_{ext} \bullet 0.00034} \tag{6.1}$$

Because both mab 19C7 and cTnI have emission at 350 nm, this emission wavelength cannot be used for detection of cTnI. For this reason, mab 19C7 was labeled with FITC as shown in Figure 6.7C. For this purpose a solution containing 0.5 mg FITC was prepared in 20 mL PBS buffer that yield 6.42×10^{-5}M FITC in PBS. The mab 19C7-modified quartz slide was place in this solution and stirred gently at 4ºC for 25 h using the experimental setup previously described in Figure 6.3. After 15 h, the slide was removed from the FITC solution and rinsed with PBS buffer. After rinsing, the slide was stored in the refrigerator at 4ºC in PBS buffer between measurements.

In order to check the mab 19C7 labeling with FITC, UV-vis spectroscopy was used for the slide blown dry with N_2 gas. The absorption spectrum is presented in Figure 6.9.

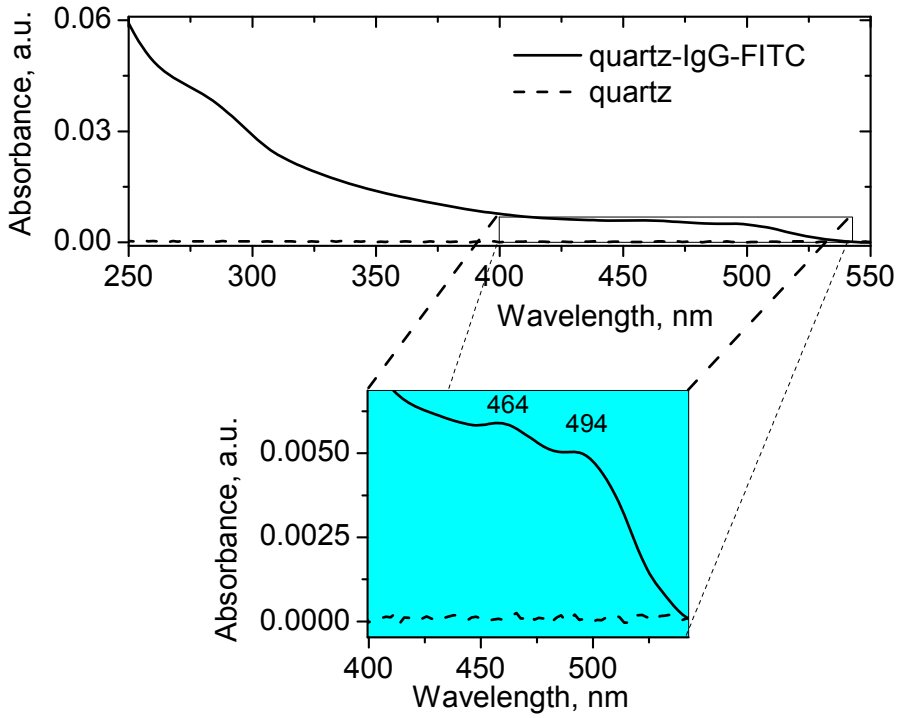

Figure 6.9. UV-vis absorption spectrum of the mab 19C7-modified quartz slide labeled with FITC.

As shown in Figure 6.9, the absorption spectrum contains a shoulder around 280 nm typical of mab 19C7 and the labeling with FITC. Also, the spectrum region 400 to 540 nm is zoomed-in to show better the absorption bands typical of FITC at 464 and 494 nm, respectively.

An epifluorescence micrograph of the mab 19C7-modified quartz slide labeled with FITC is shown in Figure 6.10. For this purpose the modified slide was irradiated with blue light. The homogeneous green regions on the surface are an additional proof

that FITC is present on the surface and some brighter spots due to salt crystals resulting from the PBS upon evaporation of water also appear.

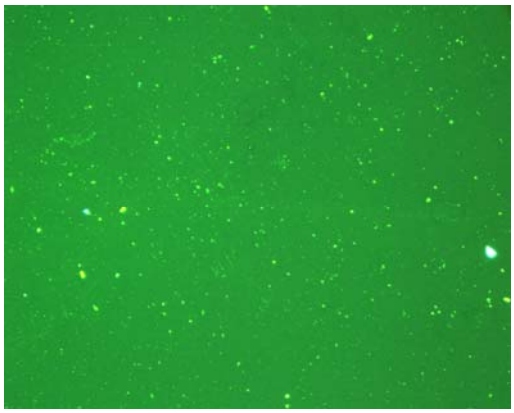

Figure 6.10. Epifluorescence micrograph of mab 19C7-modified slide labeled with FITC (895 μm × 713 μm).

6.2 Fluorescence Detection

Before to detect cTnI the mab 19C7-modified slide and labeled with FITC was placed in a 1 cm optical path length cuvette and the fluorescence of fluorescein was detected using an excitation wavelength of 494 nm (Figure 6.11 black line) in 2.5 mL PBS buffer. After this step, 10 μL of cTnI (0.8 mg/mL) in PBS were added to the 2.5 mL of PBS buffer thus the final concentration of cTnI became 3μg/mL. The 19C7-modified slide and labeled with FITC was placed in this solution and the emission spectrum acquired (Figure 6.11, red line). After this point, a fluorescence spectrum was acquired every 5 min over a time period of 135 min (Figure 6.11) in steady state (unstirred solution). It can be seen that with the increase in time there is an increase in the intensity of the emission of the fluorescein moiety. It is well known that fluorescein is a pH dependent fluorophore[143] and its fluorescence enhancement is usually attributed to changes in the microenvironment of the fluorophore.[144-146] By plotting the fluorescence maxima (518 nm) as a function of time a saturation-type of curve is obtained, that is, the

surface fluorophores present fluorescence enhancement upon cTnI binding to mab 19C7 until all the binding sites are occupied. After this point the fluorescence does not change anymore (Figure 6.12).

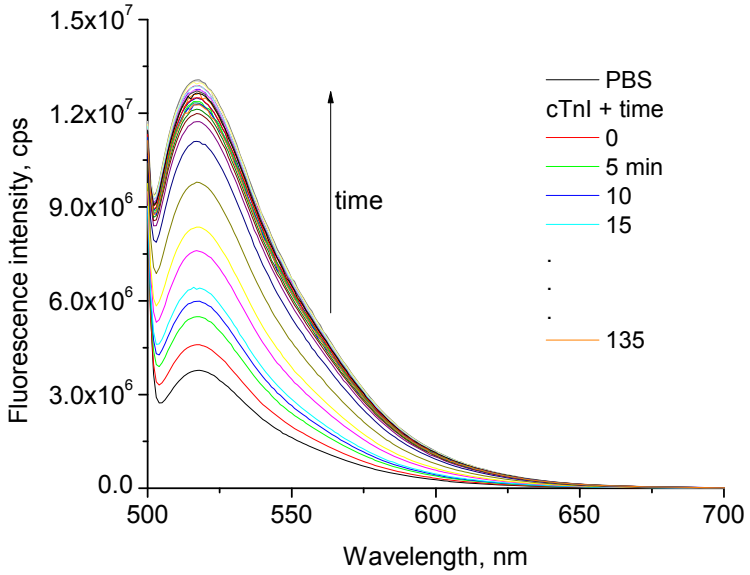

Figure 6.11. Fluorescence of FITC labeled-mab 19C7 before and after the addition of cTnI (3 µg/mL) and was followed as a function of time.

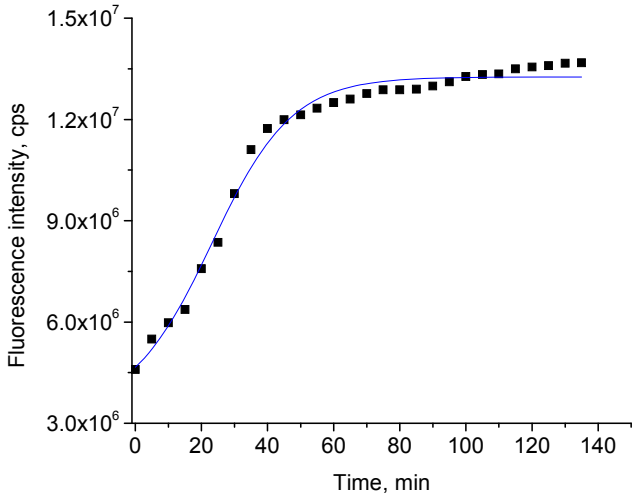

Figure 6.12. Fluorescence maxima at 518 nm as a function of time for binding of cTnI (3 µg/mL) to surface-bound mab 19C7-FITC.

Upon a closer inspection of the plot, it seems that the surface saturation with cTnI requires about 40 min for a concentration of 3 µg/mL of cTnI.

In a different experiment, instead of using a cTnI concentration of 3 µg/mL, a much lower concentration was employed, that is 0.4 ng/mL. The time dependence experiment was repeated using the mab 19C7-modified slide and the emission of FITC was again monitored as a function of time using an excitation wavelength of 494 nm. An emission spectrum was acquired every 5 min for a period of 150 min (Figure 6.13).

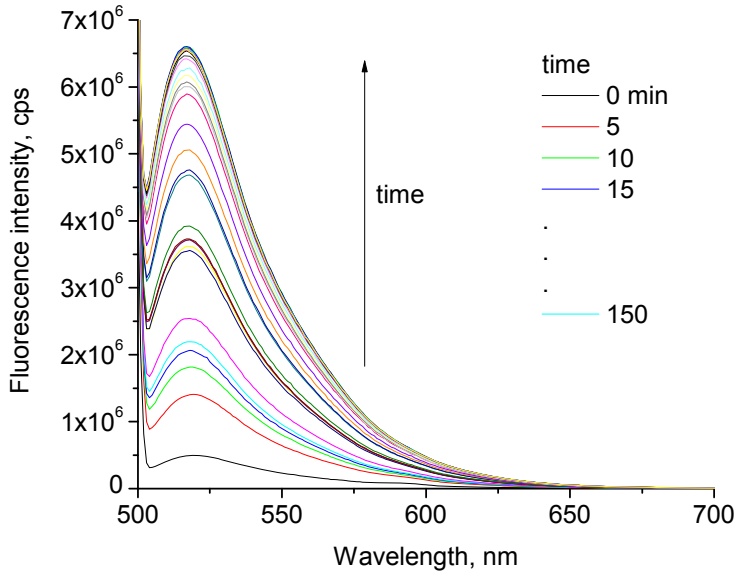

Figure 6.13. Fluorescence of FITC labeled-mab 19C7 before and after the addition of cTnI (0.4 ng/mL) and was followed as a function of time.

The same fluorescence enhancement was observed as in the previous case, even though the concentration of cTnI was in this case significantly lower. The emission position remained the same (518 nm).

By plotting the fluorescence maxima at 518 nm as a function of time (Figure 6.14) a saturation-type curve was obtained. It can be seen that in this particular case, the

time required for surface saturation was about 80 min compared to 40 min required when a more concentrated solution of cTnI (3 µg/mL) was used.

Three important conclusions can be drawn from the fluorescence enhancement of mab 19C7-FITC: (i) fluorescence enhancement occurs in presence of cTnI producing a saturation-type of curve when all mab 19C7 binding sites are occupied with cTnI; (ii) the time required to reach the saturation depends on the concentration of cTnI used. This is acceptable taking into account that all the time dependence data were acquired in steady state; (iii) in order to detect cTnI there is no need to reach saturation of the surface binding sites, a time period of 20 min long enough to cause an acceptable fluorescence enhancement for FITC in presence of both high and low concentrations of cTnI using steady state fluorescence.

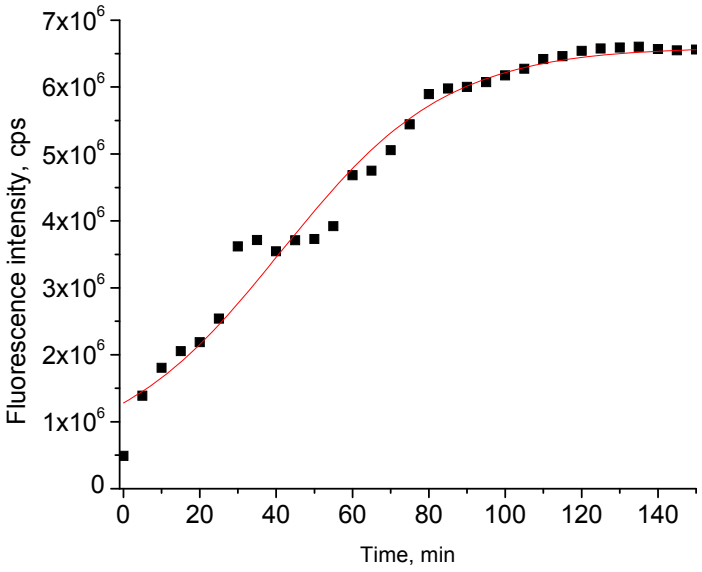

Figure 6.14. Fluorescence maxima at 518 nm as a function of time for binding of cTnI (0.4 ng/mL) to mab 19C7-FITC.

6.3 Conclusions

It was shown that detection of cTnI by a chemically –attached mutant antibody (mab 19C7) is possible even for concentrations as low as 0.4 ng/mL. In addition to the actual detection of cTnI the proper methods for surface characterization are identified and used to make sure that the chemical modification does occur according to the proposed reaction schene (Figure 6.7). These measurements are intended to be used as a platform onto which future detection schemes for cTnI bioassay development.

Chapter 7. Conclusions and Future Directions

7.1 Conclusions

In Chapter 3 it was shown that solvent evaporation is important and should not be overlooked when aromatic solvents are used.

This was proven in Chapter 4 when the effect of aromatic solvents (toluene and benzene) is compared with non-aromatic solvents such as chloroform. It was also shown that the use of toluene-water interface, widely used in asphaltene research, is not the proper choice to asses the aggregation and to investigate the spectroscopic properties of UG8 asphaltene as shown by Uv-vis and IRRAS spectroscopies. Based on the work performed in Chapter 4 it can be said that the prevention of UG8 asphaltene aggregation is hard to achieve as it seems to aggregate regardless of the solvent used for investigation.

Chapter 5 presented an attempt to study the binding of cTnI from the subphase to a monoclonal antibody (mab 560) at the air-solution interface. While the attempt was not succesfull, it provided the proper surface chemistry characterization of both the antibody and cTnI at the air-solution interface in terms of stability and spectroscopic characterization. It was shown that while UG8 asphaltene has a propensity to aggregate (UV-vis and IR measurements) visualized by BAM, the opposite can be said about the cTnI monolayer as shown using the same experimental techniques.

Chapter 6 was focused on the detection of cTnI using a chemically-attached monoclonal antibody (mab 19C7). The proposed reaction scheme for surface modification was proven to be accurate. The methods to investigate each reaction step were provided and tested.

Moreover, the proposed detection scheme detects cTnI levels as low as 0.4 ng/mL. The detection of cTnI can be pushed to lower levels as will be suggested in the following section.

7.2 Future Directions

7.2.1 Thiol-modified Surface

An alternative reaction scheme to the one proposed in Chapter 6 (Figure 6.7) using amino-modified quartz is proposed by using a thiol-modified slide.

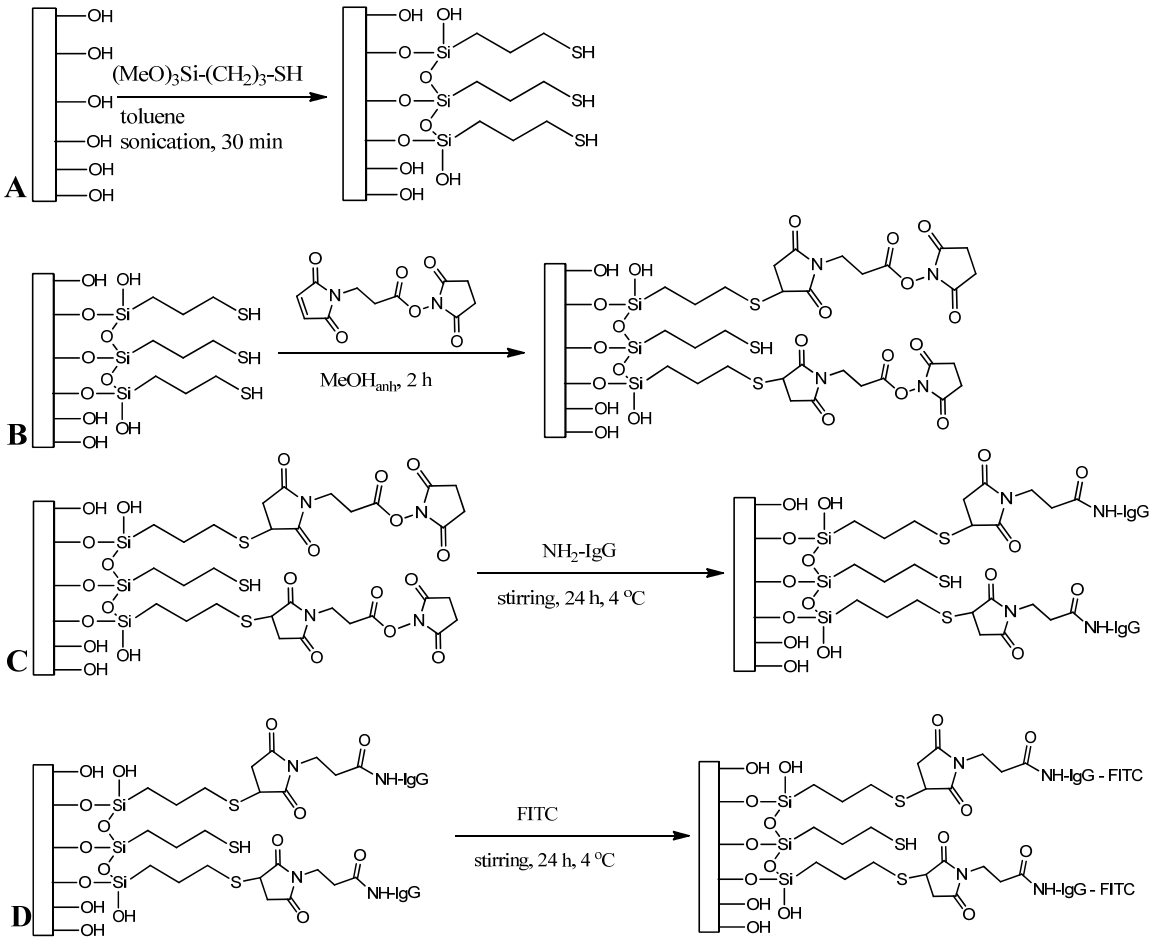

Figure 7.1. Chemical attachment scheme of mab using thiol-modified quartz slide and maleimide as linker.

The advantage of the approach depicted in Figure 7.1 relies on the use of a bifunctional linker, maleimide succinimidyl propionate. This bifunctional linker is mainly used to react the linker with a surface amino group and the second step would be to react it with a thiol group belonging to a protein.[147] An early example related to the use of thiol modified surfaces and bifunctional linkers was worked out previously.[148]

The same method used in Chapter 6 could be used for the proposed work to investigate the surface modification and the cTnI detection.

7.2.2 Amino-modified Surface

As a second alternative for the use of amino-modified surface would be to use part of Figure 6.7 related to the amino-modification and to be followed by the modification of the amino group with the maleimide succinimidyl propionate and reacting it with the thiol group from the mab 19C7 in a similar fashion as reported previously[147]. For this purpose, the whole mab 19C7 cannot be used as it does not have any surface thiol available, therefore one approach could be the use of the recombinant Fab fragment that posses a surface thiol . In addition to the fact it would maintain the mab's binding site provides a thiol group which would orient the binding site towards the solution.[149]

Chapter 8. Experimental

8.1 Chapter 3 - *Experimental*

General. All chemicals and solvents used in the experiments were the highest purity available and were purchased from Sigma-Aldrich (St Louis, MI), VWR (Estchester, PA), or MP Biomedicals (Solon, OH).

Surface Chemistry. In the present work, all surface chemistry investigations are performed in a cleanroom class 1000 where the temperature is kept constant at 20.0 ± 0.5°C and the humidity at 50.0 ± 1%. All measurements were performed on a KSV minitrough (Helsinki, Finland) equipped with computer-controlled movable barriers and fitted with the quartz window suitable for transmission absorption at the air-water interface. The KSV minitrough had an area of 225 cm^2. The UV absorption measurements were performed using an HP diode array spectrophotometer. The water used as subphase had a resistivity of 18.2 MΩ·cm and a surface tension of 72.6 mN/m at 20°C and was obtained from a Modulab 2020 water purification system (San Antonio, TX). The solvents used were of the highest purity available and were purchased from MP Biomedicals, LLC (Solon, OH). For spreading, a volume of 50 μL of pure solvent (toluene, benzene or chloroform) was used without compressing the Langmuir monolayer. An initial waiting time period of 10 min was taken before the first measurement.

8.2 Chapter 4 - *Experimental*

8.2.1 Chapter 4.1

A solution with a concentration of 1 mg/mL was prepared and the spreading volume was between 35 and 50 μL. The surface pressure which in our case was

Whatmann's filter paper soaked in ultrapure water. The spreading solvents used were toluene from Sigma Aldrich (anhydrous), MP Biochemicals (99.9% purity) and freshly distilled, and benzene (Fisher Scientific, 99.9 % purity). The measurements were performed with toluene from MP Biomedicals unless otherwise specified. The subphase used was ultrapure water with a surface tension of 72.6 mN/m and a resistivity of 18.2 MΩ·cm at 20°C and was collected from a Modulab 2020 water purification system (Continental, Houston, TX). The surface pressure-area isotherms were performed on KSV minitrough (Helsinki, Finland) with an area of 225 cm^2 fitted with a quartz window that allows the *in situ* measurement of the Langmuir film UV-vis absorbance using an HP diode array spectrophotometer. A compression rate of 10 mm/min was used for all experiments. A Kibron μtrough S (Helsinki, Finland) with an area of (5.9 cm × 21.1 cm) 124.49 cm^2 was used to monitor the surface pressure during the acquisition of the IRRAS spectra at the air-water interface.

Spectroscopy. The *in situ* UV-vis spectra of the Langmuir films were acquired using an HP diode array spectrophotometer that allows the quick collection (2-3 s) of the data compared to a typical spectrophotometer which requires a time period of 5-8 min for the data collection between 200 and 800 nm.

The IRRAS spectra were acquired using p-polarized light from the XA-511 accessory attached to a Bruker Optics (Billerica, MA) Equinox55 FTIR instrument equipped with a mercury-cadmium-telluride (MCT) liquid nitrogen-cooled detector. Each spectrum was obtained by coaddition of 1200 scans using ultrapure water as background at 8 cm^{-1} resolution and baseline correction using the polynomial option available in Bruker Optics' OPUS 5.5 software.

The solution IR measurements were performed using the Bio-ATR cell II accessory (Bruker Optics, Billerica, MA), placed in the cell compartment of the Equinox55 FTIR system, using 15-20 μL of solution. Each spectrum was obtained by coaddition of 1000 scans using toluene or deuterated toluene as background at 4 cm^{-1} resolution without background correction.

All IR measurements were performed under the following FT parameters: apodization function was Blackman-Harris 3-term; 32.00 phase resolution and Mertz phase correction mode, while the optical parameters included a KBr beamsplitter and a scanner velocity of 80 kHz for IRRAS and 10 kHz for Bio-ATR data.

Imaging. The Brewster Angle Microscopy (BAM) was performed on the IElli-2000 imaging ellipsometer equipped with the BAM2plus software to image *in situ* the asphaltene Langmuir film. A Kibron μtrough S (with an area of (5.9 cm × 21.1 cm) 124.49 cm^2) was used to monitor the surface pressure during the acquisition of the BAM micrographs under an incident angle of 53.15° using a 532 nm laser polarized light.

An atomic force microscope (AFM, Agilent Technologies, model 5420) in intermittent contact (tapping) mode using a cantilever with 159.85 kHz resonant frequency was used to acquire the AFM micrographs. To assure a repulsion dominant regime[78] the cantilever frequency was set at 159.75 kHz (Figure 8.1) to image the Langmuir-Schaefer and Langmuir-Blodgett films of UG8 asphaltene transferred onto highly oriented pyrolytic graphite (HOPG). The cantilever (Agilent Technologies) was NCL-type for acoustic AC measurements having a nominal length of 225 μm, a nominal thickness of 7 μm and the mean width of 38 μm. The nominal force constant provided by this cantilever is 48 N/m.

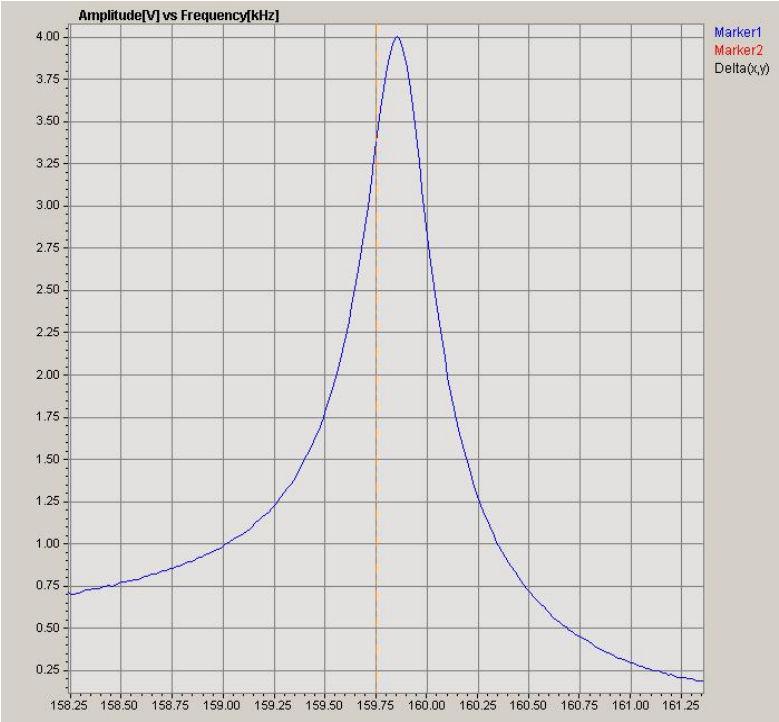

Figure 8.1. Amplitude versus frequency showing the resonant frequency at 159.85 kHz (peak maximum) and the working frequency of 159.75 kHz in repulsive dominant regime.

8.2.2 Chapter 4.2

All measurements were performed in a clean room (class 1000) under constant temperature (20.0 ± 0.5°C) and humidity (50 ± 1 %). UG8 is a type of Kuwaiti crude oil. The asphaltene extracted from UG8 crude oil is named UG8 asphaltene and was used as received from Schlumberger without further purification.

Surface chemistry. For characterization of the UG8 asphaltene Langmuir films we used surface pressure-area and compression-decompression isotherms. A solution with a concentration of 1 mg/mL was prepared in chloroform and the spreading volume was between 30 and 40 μL. The surface pressure was measured using the Wilhemy method which in our case was Whatmann's filter paper soaked in ultrapure water. The

chloroform was purchased from MP Biochemicals (99.9% purity). The subphase used was ultrapure water with a surface tension of 72.6 mN/m and a resistivity of 18.2 MΩ·cm at 20°C and was collected from a Modulab 2020 water purification system (Continental, Houston, TX). The surface pressure-area isotherms were performed on KSV minitrough (Helsinki, Finland) with an area of 225 cm^2 fitted with a quartz window that allows the *in situ* measurement of the Langmuir film UV-vis absorption using an HP diode array spectrophotometer. A compression rate of 10 mm/min was used for all experiments at the air-water interface. A Kibron μtrough S (Helsinki, Finland) with an area of 124.49 cm^2 was used to monitor the surface pressure during the acquisition of the IRRAS spectra at the air-water interface.

Spectroscopy. The *in situ* UV-vis spectra of the Langmuir films were acquired using an Hewlett-Packard (HP) diode array spectrophotometer.

The IRRAS spectra were acquired using p-polarized light from the XA-511 accessory attached to a Bruker Optics (Billerica, MA) Equinox55 FTIR instrument equipped with a mercury-cadmium-telluride (MCT) liquid nitrogen-cooled detector. The each spectrum was obtained by coadditions of 1200 scans using ultrapure water as background at 8 cm^{-1} resolution and baseline correction using the polynomial option available in Bruker Optics' OPUS 5.5 software.

All IR measurements were performed under the following FT parameters: apodization function was Blackman-Harris 3-term; 32.00 phase resolution and Mertz phase correction mode, while the optical parameters included a KBr beamsplitter and a scanner velocity of 80 kHz for IRRAS.

Imaging. The BAM was performed on the IElli-2000 imaging ellipsometer equipped with the BAM2plus software to image *in situ* the asphaltene Langmuir film. A Kibron µtrough S (area 124.49 cm^2) was used to monitor the surface pressure during the acquisition of the BAM micrographs under an incident angle of 53.15° using a 532 nm laser polarized light. An atomic force microscope (AFM, Agilent Technologies, model 5420) in intermittent contact (tapping) mode using a cantilever with 147.15 kHz resonant frequency was used to acquire the AFM micrographs. To assure a repulsion dominant regime[78] the cantilever frequency was set at 147.05 kHz (Figure 8.2) to image the Langmuir-Schaefer and Langmuir-Blodgett films of UG8 asphaltene transferred onto highly oriented pyrolytic graphite (HOPG). The cantilever (Agilent Technologies) was NCL-type for acoustic AC measurements having a nominal length of 225 µm, a nominal thickness of 7 µm and the mean width of 38 µm. The nominal force constant provided by this cantilever is 48 N/m.

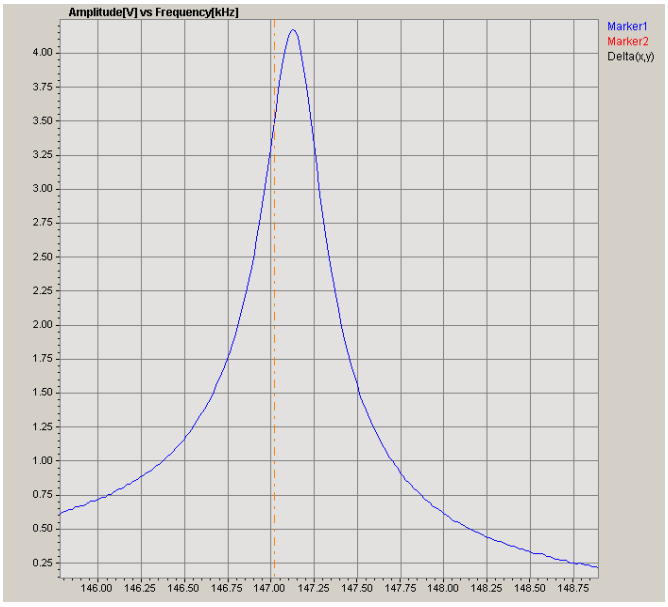

Figure 8.2. Amplitude versus frequency showing the resonant frequency at 147.15 kHz (peak maximum) and the working frequency of 147.05 kHz in repulsive dominant regime.

Mathematical treatment to show the conversion from concentration to surface density in Langmuir films

$$A = \varepsilon \times b \times c$$

$$c = \frac{mol}{L} = \frac{mol}{1000\,cm^3} \; or \; \frac{mg}{mL} = \frac{mg}{cm^3}$$

$$b \times c = cm \times \frac{mol}{1000\,cm^3} = \frac{mol}{1000\,cm^2} \; or \; \frac{mg}{cm^2} = \rho$$

$$A = \varepsilon \times \rho; \varepsilon = const.$$

$$\Rightarrow A \propto \rho$$

A = absorbance

ε = molar absorptivity

c = concentration

ρ = surface density

8.3 Chapter 5 - *Experimental*

8.3.1 Recombinant cTnI Protein Expression and Purification

The coding sequence for human cTnI was inserted into pET28a(+) (Novagen, division of EMD Biosciences/Merck K.G.A. Darmstadt, Germany) and *E. coli* BL21 (DE3) cells, which were transformed with the plasmid for expression of troponin. Cells were grown in 2 L of Lennox LB Broth (MP Biomedicals LLC, Santa Ana, CA) containing 30 μg/mL kanamycin at 37 °C × 250 rpm until the absorbance = 0.4 to 0.6. Isopropyl-β-D-thiogalactopyranoside (IPTG) was then added to a final concentration of 1 mM and the culture allowed to grow overnight. Purification of the cTnI was based on the method published before[150] with some modifications. Cells were pelleted by centrifugation and resuspended in 40 mL of buffer A (25 mM triethanolamine (TEA), pH

7.5, 2 mM EDTA, 6 M urea). The cells were lysed by FastPrep-24® system (MP Biomedicals LLC, Santa Ana, CA). The lysate was then centrifuged at 22,000× g for 25 min. The supernatant was applied to a DEAE Sepharose Fast Flow (GE Healtcare, Uppsala) column (20 mm × 65 mm) equilibrated with buffer A. The flow through fraction containing cTnI, was collected and applied to a CM Sepharose (GE Healtcare, Uppsala) column (20 mm x 65 mm) equilibrated with Buffer A. The protein was eluted using a salt gradient from 0 to 1 M NaCl in Buffer A over 10 column volumes at a flow rate of 4.5 mL/min. Fractions containing cTnI were determined by SDS-PAGE and were pooled together (Experimental section contains the SDS-PAGE and Western Blot data). Ammonium sulfate to 1 M final concentration was added to the pooled fractions and the protein was applied to a Butyl Sepharose (GE Healtcare, Uppsala) column (20 mm × 65 mm) equilibrated with buffer B (20 mM Tris/Cl, pH 7.5, 6 M urea, 1 M ammonium sulfate (all chemicals from MP Biomedicals, LLC, Santa Ana, CA). The protein was eluted from the column using a gradient of 1 to 0 M ammonium sulfate in Buffer B. Fractions containing cTnI were determined by SDS-PAGE and pooled together. Purity of the protein was determined by scanning Coomassie Blue stained gels and integrating the area under the peak using SigmaGel software. The protein was determined to be ≥ 97% pure. The molecular weight of the protein is 24,007 as determined from the known amino acid sequence. The protein expressed and purified as per protocol described above is commercially available from MP Biomedicals LLC (Santa Ana, CA).

8.3.2 Protein Expression and Purification

The human cardiac troponin I actually runs at a slightly higher molecular weight, at around 30,000 Da, on SDS-polyacrylamide gels. This apparently is a know anomaly with

the cardiac troponins; not all proteins run precisely at their predicted MW on gels and cardiac TPN is one of them.[151]

When expressing the recombinant troponin I, the author was not aware of this fact and initially thought the protein expressed was not correct because of its too large size. After confirming the sequence of the gene being expressed and seeing the protein show up in Western blots, it was found in the literature that the protein does run slightly large on gels. As a control run, purchased native and recombinant cardiac troponins along the recombinant protein were found to co-migrate in SDS-Page and Western Blot as shown in Figures 8.3 and 8.4.

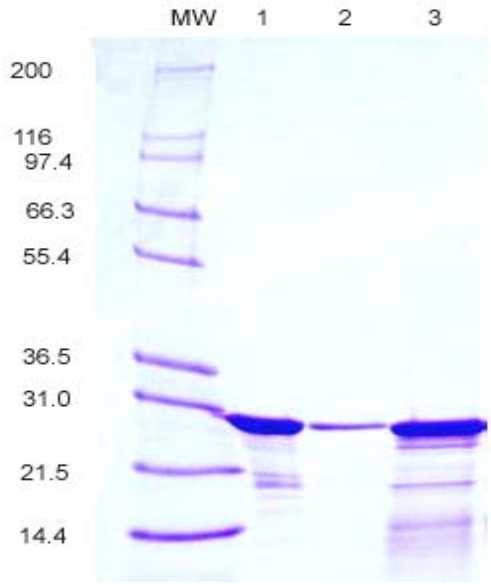

Figure 8.3. SDS-PAGE of cTnI.

MW = Mark 12 unstained standards (from Invitrogen)

Lane 1 = Native human cardiac troponin I (Abcam cat. no. 9936)

Lane 2 = Recombinant human cardiac troponin I (Abcam cat. no. 9935)

Lane 3 = Recombinant human cardiac troponin I. (Partially purified from CM Sepharose)

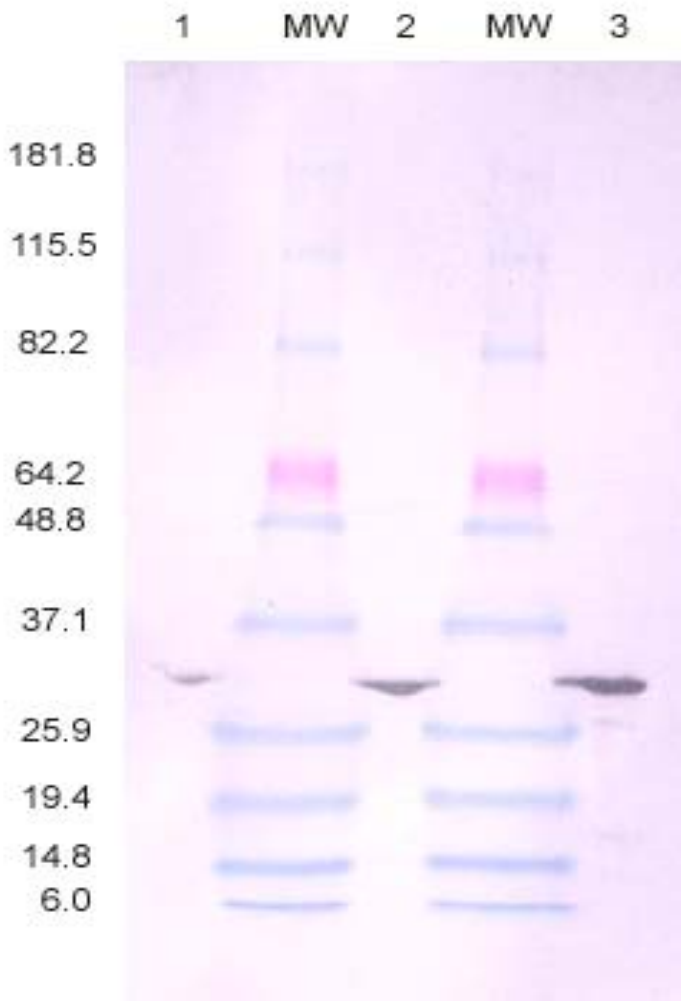

Figure 8.4. Western Blot of cTnI.

MW = Benchmark prestained molecular weight standards (Invitrogen)

Lane 1 = Recombinant human cardiac troponin I (Abcam cat. no. 9935)

Lane 2 = Recombinant human cardiac troponin I (Partially purified from CM Sepharose)

Lane 3 = Native human cardiac troponin I (Abcam cat. no. 9936)

Method for Western Blot

Proteins were run on an SDS-polyacrylamide gel and then electrophoretically transferred to a PVDF membrane. The membrane was blocked using Tris Buffer Saline (TBS, 50 mM Tris-HCl, pH 7.4, 150 mM NaCl) containing 10% non-fat dry milk (NFDM) at room temperature for 30 min. The membrane was then incubated at room temperature for 1 h with a monoclonal antibody (Chemicon cat. no. MAB3150) against the 19C7 epitope of human cardiac troponin. The antibody was diluted 1:2000 in TBS + 10% NFDM. The membrane was washed with TBS and then incubated with anti-mouse IgG-alkaline phosphatase diluted 1:5000 in TBS + 10% NFDM for 1 h at room temperature. The membrane was again washed with TBS and the color developed by incubating the membrane in alkaline phosphatase buffer (100 mM tris pH 9.5; 100 mM NaCl; 5 mM $MgCl_2$) containing substrate (20 μg nitrobluetetrazolium/ml and 50 μg bromochloroindoyophosphate/ml).

8.3.3 Surface chemistry

Surface Chemistry. All surface chemistry measurements were performed in a cleanroom (Class 1000) with controlled temperature (20.0 ± 0.5 °C) and humidity (50 ± 1%). The measurements were performed on a KSV minitrough (Helsinki, Finland) with an area of 225 cm^2. The subphase used was ultrapure water obtained from a Millipore water purification system (San Antonio, TX) and had a resistivity of 18.2 MΩ·cm and a surface tension of 72.6 mN/m at 20°C. The surface pressure-area isotherms were performed using the Wilhelmy method, which is, in our case, a Whatmann filter paper soaked in ultrapure water. The surface potential-area isotherms were measured using Kelvin probe (a vibrating electrode placed 1.5 mm above the surface and a second platinum disk electrode

placed inside the subphase between which the potential was measured). Potassium chloride of purity 99.9% (MP Biomedicals LLC, Santa Ana, CA) was used to prepare solutions of different concentrations used as subphases with different ionic strengths.

Infrared Reflection-Absorption Spectroscopy (IRRAS). The infrared spectra were acquired directly at the air-subphase interface using a Bruker Equinox55 FT-IR instrument (Billerica, MA) equipped with the XA-511 accessory for air-water interface. The trough used was a Kibron μtrough S (Helsinki, Finland) with an area of (5.9 cm × 21.1 cm) 124.49 cm^2. The measurements were performed using p-polarized light and a mercury-cadmium-telluride (MCT) liquid nitrogen-cooled detector. The spectra were obtained by co-addition of 1200 scans at different incident angles at a resolution of 4 cm^{-1} and baseline correction using the polynomial option available in Bruker Optics' OPUS 5.5 software.

The secondary structure of cTnI in solution was determined using a FT-IR accessory based on attenuated total reflectance (Bio-ATR II cell) purchased from Bruker Optics (Billerica, MA). The advantage of this cell is the low volume of solution required for measurements (10 – 20 μL). The data acquisition was performed by co-addition of 1000 scans at a resolution of 4 cm^{-1} without baseline correction.

Brewster Angle Microscopy (BAM). Brewster angle imaging was performed at the air-subphase interface using an IElli-2000 imaging ellipsometer provided by Accurion (Menlo Park, CA) with Bam2Plus Software. The standard laser of the BAM2plus was a frequency-doubled Nd:YAG laser with a wavelength of 532 nm. The laser had a power of 50 mW in a collimated beam. The angle of incidence was set at 53°, near the Brewster angle for water at 53.12°.

UV-vis absorption was performed using an HP diode array spectrophotometer on a KSV minitrough (Helsinki, Finland) equipped with computer-controlled movable barriers and fitted with a quartz window suitable for absorption measurements at the air−water interface, with the lamp located above the Langmuir trough and the detector under the quartz window of the Langmuir trough.

Fluorescence at the air-subphase interface was performed using a Fluorolog-3 spectrofluorimeter (Horiba Scientifics) equipped with a bifurcated optical fiber for excitation and emission, respectively.

Fluorescence labeling: In order to better visualize the aggregation process a contrast agent was used, namely fluorescein isothiocyanate (FITC). FITC is a commonly used fluorescent label that be attached to proteins in very mild conditions by simply mixing the protein of interest, cTnI in the present case, with the FITC over a few hours. The labeling occurs via chemical attachment of FITC through its isothiocyanate group that reacts with the amine group of the lysine amino acid present in cTnI. The labeling of cTnI was carried out in 50 mM borate buffer, pH 8.8. Unreacted FITC was removed by extensive dialysis against 30 mM TrisHCl, pH 7.6.

Epifluorescence microscopy: An epifluorescence microscope (model IX-FLA, Olympus) was used for acquiring the fluorescence micrographs of the monolayer at the air−subphase interface at different constant surface pressures during compression on a Kibron minitrough (area available for spreading solution 5.9 × 19.5 cm^2, Kibron Inc., Helsinki, Finland). A thermoelectrically cooled Optronics Magnafire^{TM} CCD camera detected the emission from the Langmuir monolayer.

References

1. Gaines G. L. Jr. *Insoluble Monolayers at Liquid−Gas Interfaces*; Interscience Publisher: New York, **1966**.

2. Roberts, G. *Langmuir-Blodgett films*; Plenum Press, New York, **1990**.

3. Orbulescu, J. MSc Thesis, University of Miami, USA, **2001**.

4. Orbulescu, J.; Mello, S. V.; Huo, Q.; Sui. G.D.; Kele, P.; Leblanc, R. M. *Langmuir* **2001**, 17, 1525-1528.

5. Langmuir, I.; Schaefer, V. J. *Chem. Rev.* **1939**, 24, 181-202.

6. Langmuir, I.; Schaefer, V. J. *J. Am. Chem. Soc.* **1938**, 60, 2803-2810.

7. KSV Instruction Manual (KSV Nima Inc), Helsinki, Finland, **2001**.

8. Bio-ATR User Manual (Bruker Optics), Ettlingen, Germany, **2004**.

9. Francis, S.A.; Ellison, A. H. *J. Opt. Soc. Am.* **1959**, 49, 131-138.

10. Hasegawa, T.; Umemura, J.; Takenaka, T. *Appl. Spectrosc.* **1993**, 47, 338-340.

11. Hasegawa, T.; Takeda, S.; Kawaguchi, A.; Umemura, J. *Langmuir* **1995**, 11, 1236-1243.

12. Brunner, H.; Mayer, U.; Hoffmann, H. *Appl. Spectrosc.* **1997**, 51, 209-217.

13. Frey, B. L.; Corn, R. M.; Weibel, S. C. In *Handbook of Vibrational Spectroscopy*, John Wiley & Sons, Ed. Chalmers, JM, Griffiths, PR, **2002**.

14. Mendelsohn, R.; Flach, C.R. In *Handbook of Vibrational Spectroscopy*, John Wiley & Sons, Ed. Chalmers, J. M.; Griffiths, P.R. **2002**.

15. Dluhy, R. A. *Appl. Spectrosc. Rev.* **2000**, 35, 315-351.

16. Simon-Kutscher, J.; Gericke, A.; Hühnerfuss, H. *Langmuir* **1996**, 12, 1027-1034.

17. Blaudez, D.; Buffeteau, T.; Cornut, J. C.; Desbat, B.; Escafre, N.; Pezolet, M.; Turlet, J. M. *Appl. Spectrosc.* **1993**, 47, 869-874.

18. Blaudez, D.; Buffeteau, T.; Cornut, J. C.; Desbat, B.; Escafre, N.; Pezolet, M.; Turlet, J. M. *Thin Solid Films* **1994**, 242, 146-150.

19. Huo, Q.; Dziri, L.; Desbat, B.; Russel, K. C.; Leblanc, R. M. *J. Phys. Chem. B* **1999**, 103, 2929-2934.

20. Dziri, L.; Desbat, B.; Leblanc, R. M. *J. Am. Chem. Soc.* **1999**, 121, 9618-9625.

21. Dluhy, R. A. *J. Phys. Chem. B* **1986**, 90, 1373-1379.

22. Mitchell, M. L.; Dluhy, R. A. *J. Am. Chem. Soc.* **1988**, 110, 712-718.

23. Brockman, J. M.; Wang, Z. D.; Notter, R. H.; Dluhy, R. A. *Biophys. J.* **2003**, 84, 326-340.

24. Mendelsohn, R.; Brauner, J. W.; Gericke, A. *Ann. Rev. Phys. Chem.* **1995**, 46, 305-334.

25. Chia, N. C.; Mendelsohn, R. *Biochim. Biophys. Acta-Biomembranes* **1996**, 1283, 141-150.

26. Mendelsohn, R.; Mao, G. R.; Flach, C.R. *Biochim. Biophys. Acta-Biomembranes* **2010**, 1798, 788-800.

27. Ulman, A. *Ultrathin Organic Films*, Academic Press, **2001**.

28. Henon, S.; Meunier, J. *Rev. Sci. Instrum.* **1991**, *62*, 936-939.

29. I-Elli200 User Manual, Gottingen, Germany, **2001**.

30. Agilent Technologies Atomic Force Microscopy User Manual, **2009**.

31. Nordgård, E. L.; Landsem, E.; Sjöblom, J. *Langmuir* **2008**, 24, 8742-8751.

32. Cadena-Nava, R. D.; Cosultchi, A.; Ruiz-Garcia, J. *Energy Fuels* **2007**, 21, 2129-2137.

33. Lamarche, F.; Picard, G.; Techy, F.; Aghion, J.; Leblanc, R. M. *Eur. J. Biochem.* **1991**, 197, 529-534.

34. Leblanc, R. M.; Thyrion, F. C. *Fuel* **1989**, 68, 260-262.

35. Hasegawa, T.; Kawato, H.; Toudou, M.; Nishijo, J. *J. Phys. Chem. B* **1997**, 101, 6701-6706.

36. Zhang, L. Y.; Xu, Z.; Masliyah, J. H. *Langmuir* **2003**, 19, 9730-9741.

37. Zhang, L. Y.; Lawrence, S.; Xu, Z.; Masliyah, J. H. *J. Coll. Interface Sci.* **2003**, 264, 128-140.

38. Baret, J. F.; Bois, A. G.; Casalta, L.; Dupin, J. J.; Firpo, J. L.; Gonella, J.; Melinon, J. P. *Coll. Polymer Sci.* **1976**, 254, 577-580.

39. Crews, P.; Rodriguez, J.; Jaspars, M. *Organic Structure Analysis* **1998**, Oxford University Press, NY, pp. 361.

40. Banat, F. A.; Simandl, J. *Chem. Eng. Sci.* **1996**, 51, 1257-1265.

41. Antoine, C. *CR Chim.* **1888**, 107, 681-684.

42. Ohe, S. *Computer Aided Data Book of Vapor Pressure,* 2nd Ed. Data Book Publishing, Chiyoda-ku, Tokyo, Japan (http://e-data.jp/vpcal2/e/Toluene_cal.html).

43. Ohe, S. *Computer Aided Data Book of Vapor Pressure,* 2nd Ed. Data Book Publishing, Chiyoda-ku, Tokyo, Japan (http://e-data.jp/vpcal2/e/Benzene_cal.html).

44. Jaffé, H. H.; Orchin, M. *Theory and Applications of Ultraviolet Spectroscopy* **1962**, Wiley, New York.

45. Wang, S.; Leblanc, R. M.; Arias, F.; Echegoyen, L. *Langmuir* **1997**, 13, 1672-1676.

46. Sheu, E.Y.; Mullins, O.C. *Asphaltenes: Fundamentals and Applications*. Plenum Press, New York, **1995**.

47. Mansoori, G. A. Nanoscale structures of asphaltene molecule, asphaltene steric-colloid and asphaltene micelles and vesicules. (http://tigger.uic.edu/~mansoori/ Asphaltene.Molecule_html).

48. Mahan, Y.; Chodakowski, M.; Zhang, X.; Shaw, J. M. Asphaltene phase behavior: Prediction at a crossroads. Presented at the Tenth International Conference on Properties and Phase Equilibria for Product and Process Design, Snowbird, UT, May 17-21, **2004**.

49. Friberg, S. E.; Micellization, Chapter 7; In: Mullins, O. C.; Sheu, E. Y.; Hammani, A.; Marshall, A. G. (Eds), *Asphaltenes, Heavy Oils and Petroleomics*, Springer, New York, **2007**.

50. Mullins, O. C. Optical interrogation of aromatic moities in crude oils and asphaltenes, Chapter 2; In: Mullins, O. C.; Sheu, E. Y. (Eds). *Structures and Dynamics of Asphaltenes*, Plenum, New York, **1998.**

51. Ruiz-Morales, Y. Molecular orbital calculations and optical transitions of PAHs and asphaltenes, Chapter 4; In: Mullins, O. C.; Sheu, E. Y.; Hammani, A.; Marshall, A. G. (Eds), *Asphaltenes, Heavy Oils and Petroleomics*, Springer, New York, **2007**.

52. Boduszynski, M. M.; Altgelt, K. H. *Composition and Analysis of Heavy Petroleum Fractions,* CRC Press: New York, NY, **1994**.

53. Rodgers, R. P.; McKenna, A. M.; Mapolelo, M. M.; Ehrmann, B. M.; Robbins, W. K.; Marshall, A. G. The compositional continuum of petroleum, Petrophase XI - 2010, 11th International Conference on Petroleum Phase Behavior and Fouling, June 13-17, **2010**, Jersey City, NJ)

54. Mullins, O. C.; Sheu, E. Y. *Structures and Dynamics of Asphaltenes*, Plenum Press: New York, **1998**.

55. Mullins, O. C.; Sheu, E. Y.; Hammani, A.; Marshall, A. G. *Asphaltenes, Heavy Oils and Petroleomics*, Springer, New York, **2007**.

56. Jones, T. J.; Neustadter, E. L.; Whittingham, K. P. *J. Can. Pet. Technol.* **1978**, *17*, 100–108.

57. Zhang, L. Y.; Xu, Z.; Masliyah, J. H. *Ind. Eng. Chem. Res.* **2005**, *44*, 1160–1174.

58. Zhang, L. Y.; Breen, P.; Xu, Z.; Masliyah, J. H. *Energy Fuels* **2007**, *21*, 274–285.

59. Sharath Chandra, M.; Xu, Z.; Maslyiah, J. H. *Energy Fuels* **2008**, *22*, 1784–1791.

60. Wang, S.; Liu, J.; Zhang, L.; Xu, Z.; Masliyah, J. H. *Energy Fuels* **2009**, *23*, 862–869.

61. Ese, M. H.; Yang, X.; Sjöblom, J. *Colloid Polym. Sci.* **1998**, *276*, 800–809.

62. Lobato, M. D.; Pedrosa, J. M.; Hortal, A. R.; Martinez-Haya, B.; Lebron-Aguilar, R.; Lago, S. *Coll. Surf. A: Physicochem. Eng. Aspects* **2007**, *298*, 72–79.

63. Zhang, L. Y.; Lawrence, S.; Xu, Z.; Masliyah, J. H. *J. Coll. Interf. Sci.* **2003**, *264*, 128–140.

64. Lobato, M. D.; Pedrosa, J. M.; Möbius, D.; Lago, S. *Langmuir* **2009**, *25,* 1377–1384.

65. Strausz, O. P.; Safarik, I.; Lown, E. M.; Morales-Izquierdo, A. *Energy Fuels* **2008**, 22, 1156– 1166.

66. Groenzin, H.; Mullins, O. C. *J. Phys. Chem. A* **1999**, *103*, 11237–11245.

67. Groenzin, H.; Mullins, O. C. *Energy Fuels* **2000**, *14*, 677–684.

68. Buenrostro-Gonzalez, E.; Groenzin, H.; Lira-Galeana, C.; Mullins, O. C. *Energy Fuels* **2001**, *15*, 972–978.

69. Groenzin, H.; Mullins, O. C.; Eser, S.; Mathews, J.; Yang, M.-G.; Jones, D. *Energy Fuels* **2003**, *17*, 498–503.

70. Badre, S.; Goncalves, C. C.; Norinaga, K.; Gustavson, G.; Mullins, O. C. *Fuel* **2006**, *85*, 1–11.

71. Buch, L.; Groenzin, H.; Buenrostro-Gonzalez, E.; Andersen, S.I.; Lira-Galeana, C.; Mullins, O. C. *Fuel* **2003**, *82*, 1075–1084.

72. Groenzin, H.; Mullins, O. C. In *Asphaltenes, Heavy Oils and Petroleomics*; Mullins, O. C., Sheu, E. Y., Hammami, A., Marshall, A. G., Eds.; Springer: New York, **2007**; Chapter 2.

73. Hurtado, P.; Hortal, A. R.; Martinez-Haya, B. *Rapid Commun. Mass. Spectrom.* **2007**, *21*, 3161–3164.

74. Klein, G. C.; Kim, S.; Rodgers, R. P.; Marshall, A. G.; Yen, A.; Asomaning, S. Energy Fuels **2006**, *20*, 1965–1972.

75. Pomerantz, A. E.; Hammond, M. R.; Morrow, A. L.; Mullins, O. C.; Zare, R. N. *J. Am. Chem. Soc.* **2008**, *130*, 7216–7217.

76. Pomerantz, A. E.; Hammond, M. R.; Morrow, A. L.; Mullins, O. C.; Zare, R. N. *Energy Fuels* **2009**, *23*, 1162–1168.

77. Orbulescu, J.; Leblanc, R. M. *J. Phys. Chem. C* **2009**, *113*, 5313–1315.

78. Haugstad, G.; Jones, R. R. *Ultramicroscopy* **1999**, *76*, 77–86.

79. Mullins, O.C. *Energy Fuels* **2010**, *24*, 2179–2207.

80. Ralston, C. Y.; Mitra-Kirtley, S.; Mullins, O. C. Energy Fuels, **1996**, 10, 623–630.

81. Orbulescu, J.; Mullins, O. C.; Leblanc, R. M. *Langmuir* **2010**, 26, 15265-15271.

82. Gawrys, K. L.; Blankenship, G. A.; Kilpatrick, P. K. *Langmuir* **2006**, *22*, 4487–4497.

83. Gericke, A.; Michailov, A. V.; Huhnerfuss, H. *Vib. Spectrosc.* **1993**, *4*, 335–348.

84. Andreatta, G.; Goncalves, C. C.; Buffin, G.; Bostrom, N.; Quintella, C. M.; Arteaga-Larios, F.; Perez, E.; Mullins, O. C. *Energy Fuels* **2005**, 19, 1282–1289.

85. Andreatta, G.; Bostrom, N.; Mullins, O. C. *Langmuir* **2005**, 21, 2728–2736.

86. Dickie, J. P.; Yen, T. F. *Anal. Chem.* **1967**, *39*, 1847–1852.

87. Freed, D. E.; Lisitza, N. V.; Sen, P. N.; Song, Y. Q. *Energy Fuels* **2009**, 23, 1189–1193.

88. Klein, G. C.; Kim, S.; Rodgers R. P.; Marshall, A. G. *Energy Fuels* **2006**, *20*, 1965–1972.

89. Klein, G. C.; Kim, S.; Rodgers R. P.; Marshall, A. G.; Yen, A. *Energy Fuels* **2006**, *20*, 1973–1979.

90. Kim, S.; Rodgers, R. P.; Blakney, G. T.; Hendrickson, C. L.; Marshall, A. G. *J. Am. Soc. Mass Spectr.* **2009**, *20*, 263-268.

91. McKenna, A. M.; Purcell, J. M.; Rodgers, R. P.; Marshall, A. G. *Energy Fuels* **2009**, *23*, 2122–2128.

92. Orbulescu, J.; Mullins, O. C.; Leblanc, R. M. *Langmuir* **2010**, 26, 15257–15264.

93. Kazakova, V. I.; Koretskii, A. F. *Russ. Chem. Bull.* **1970**, 19, 1855– 1858.

94. Vieira, V. C. C; Severino, D.; Oliveira, O. N., Jr.; Pavinatto, F. J.; Zaniquelli, M. E. D.; Ramos, A. P.; Baptista, M. S. *Langmuir* **2009**, 25, 12585– 12590.

95. Diaz, M. E.; Montes, F. J.; Gálan, M. A. *Energy Fuels* **2007**, 21, 3455– 3461.

96. Álvarez, L.; Díaz, M. E.; Montes, F. J.; Gálan, M. A. *Fuel* **2010**, 89, 691– 702.

97. Álvarez, L.; Díaz, M. E.; Montes, F. J.; Gálan, M. A. *Energy Fuels* **2010**, 24, 1771–1780.

98. Cohen, S.; Porter, R. R. *Adv. Immunol.* **1964**, 3, 287–349.

99. Edelman, G. M.; Cunningham, B. A. .; Gall, W. E.; Gottlieb, P. D.; Rutishauser, U.; Waxdal, M. J. *Proc. Natl. Acad. Sci.* **1969**, 62, 78–85.

100. Bindon, C. I.; Hale, G.; Bruggemann, M.; Waldmann, H. *J. Exp. Med.* **1988**, 168, 127–142.

101. Harlow, E.; Lane, D. *Antibodies: A Laboratory Manual.* Cold Spring Harbor, NY: Cold Spring Harbor Laboratory, **1988**.

102. Goding, J. W. *Monoclonal Antibodies: Principles and Practice.* 3rd edn. London, San Diego: Academic Press, **1996**.

103. Coligan, J. E.; Bierer, B. E.; Margulies, D. H.; Shevach, E. M.; Strober, W. *Current Protocols in Immunology*. New York: John Wiley and Sons, **2004**.

104. http://www.aceanimals.com/BalbC.htm

105. Monoclonal mouse anti-cardiac troponin I (cTnI) Catalogue #: 4T21, available at http://www.hytest.fi/sites/hytest.fi/files/4T21.pdf

106. Möhwald, H. *Annu. Rev. Phys. Chem.* **1990**, 41, 441-476.

107. Gidalevitz, D.; Ushitsuka, Y.; Muresan A. S.; Konovalov, O.; Waring, A. J., Lehrer, R. H. Lee, K.Y.C. *Proc Nat. Acad. Sci.* **2003**, 100, 11, 6302-6307.

108. Myocardial infarction redefined—a consensus document of The Joint European Society of Cardiology/American College of Cardiology Committee for the redefinition of myocardial infarction. *Eur. Heart J.* **2000**, 21, 1502–1513.

109. Thygesen, K.; Alpert, J. S.; White, H. D. *Eur. Heart J.* **2007**, 28, 2525–2538.

110. Heidenreich, P. A.; Alloggiamento, T.; Melsop, K.; McDonald, K. M.; Go, A. S.; Hlatky, M. A. *J. Am. Coll. Cardiol.* **2001**, 38, 478–485.

111. Lindahl, B. *Scand. Cardiovasc. J.* **2001**, 35, 229–232.

112. Ilva, T.; Lund, J.; Porela, P.; Mustonen, H.; Voipio-Pulkki, L. -M.; Eriksson, S.; Pettersson, K.; Tanner, P.; Pulkki, K. *Clin. Chim. Acta* **2009**, 400, 82-85.

113. Leavis, P.; Gergely, J. *CRC Crit. Rev. Biochem.* **1984**, 16, 235–305.

114. Filatov, V. L.; Katrukha, A. G.; Bulargina, T. V.; Gusev, N. B. *Biochemistry (Mosc)***1999**, 64, 969–985.

115. Adamson, A. W.; Gast, A. P. *Physical chemistry of surfaces*. Wiley and Sons **1997**.

116. Mair, J.; Apple, F. *Crit. Rev. Clin. Lab. Sci.* **1997**, 34, 1–66.

117. Sumandea, M. P.; Burkart, E. M.; Kobayashi, T.; De Tombe, P. P.; Solaro, R. J. *Ann. N.Y. Acad. Sci.* **2006**, 1015, 39-52.

118. Bjellqvist, B.; Hughes, G. J.; Pasquali, C.; Paquet, N.; Ravier, F.; Sanchez, J. -C.; Frutiger, S.; Hochstrasser, D. *Electrophoresis* **1993**, 14, 1023–1031.

119. http://ca.expasy.org/tools/pi_tool.html.

120. Kele, P.; Orbulescu, J.; Mello, S. V.; Mabrouki, M.; Leblanc, R. M. *Langmuir* **2001**, 17, 7286–7290.

121. Guilbault, G. G.; Montalvo, J. G. *J. Am. Chem. Soc.* **1969**, 91, 2164–2165.

122. Guilbault, G. G.; Montalvo, J. G. *J. Am. Chem. Soc.* **1970**, 92, 2533–2538.

123. Angenendt, P.; Glokler, J.; Murphy, D.; Lehrach, H.; Cahill, D. J. *Anal. Biochem.* **2002**, 309, 253–260.

124. Brueggemeier, S. B.; Wu, D.; Kron, S.J.; Palecek, S. P. *Biomacromolecules* **2005**, 6, 2765–2775.

125. Fidanza, J.; Glazer, M.; Mutnick, D.; McGall, G.; Frank, C. *Nucleosides Nucleotides Nucleic Acids* **2001**, 20, 533–538.

126. Wang, H.; Li, J.; Liu, H.; Liu, Q.; Mei, Q.; Wang, Y.; Zhu, J.; He, N.; Lu, Z. *Nucleic Acids Res* **2002**, 30, e61.

127. Zubtsov, D. A.; Ivanov, S.M.; Rubina, A.Y.; Dementieva, E.I.; Chechetkin, V.R.; Zasedatelev, A. S. *J. Biotechnol.* **2006**, 122, 16–27.

128. Engvall, E.; Perlman, P. *Immunochemistry* **1971**, 8, 871–874.

129. Boksányi, L.; Liardon, O.; Kováts, E. Sz. *Adv. Colloid. Interface Sci.* **1976**, 6, 95–137.

130. Tripp, C.P.; Hair, M. L. *Langmuir* **1995**, 11, 149–155.

131. Clark, J. H.; Macquarrie, D. J. *Chem. Commun.* **1998**, 8, 853–860.

132. Blitz, J. P.; Murthy, R. S. S.; Leyden, D. E. *J. Colloid Interface Sci.* **1988**, 121, 63–69.

133. Angst, D. L.; Simmons, G. W. *Langmuir* **1991**, 7, 2236–2242.

134. Azzopardi, M. J.; Arribart, H. *J. Adhesion* **1994**, 46, 103–115.

135. Orbulescu, J.; Constantine, C. A.; Rastogi, V. K.; Shah, S.S.; DeFrank, J. J.; Leblanc, R. M. *Anal. Chem.* **2006**, 78, 7016-7021.

136. Kele, P.; Orbulescu, J.; Gawley, R. E.; Leblanc, R. M. *Chem. Commun.* **2006**, 14, 1494-1496.

137. Tripp, C. P.; Hair, M. L. *Langmuir* **1992**, 8, 1961–1967.

138. McGovern, M. E.; Kallury, K. M. R.; Thompson, M. *Langmuir* **1994**, 10, 3607–3614.

139. Navarre, S.; Choplin, F.; Bousbaa, J.; Bennetau, B.; Nony, L.; Aimé, J. -P. *Langmuir* **2001**, 17, 4844–4850.

140. Gobet, J.; Kováts, E. Sz. *Adsorp. Sci. Technol.* **1984**, 1, 77–92.

141. Yoshida, W.; Castro, R. P.; Jou, J. -D.; Cohen, Y. *Langmuir* **2001**, 17, 5882–5888.

142. Marriot, G.; Parker, I. *Methods in Enzymology, Biophotonics*, Vol. 360, Part A, pp. 16, Academic Press, **2003**.

143. Laz, E.; Gregor, M.; Slavik, J.; Kotyk, A. *J. Fluor.* **1997**, 7, 317 – 319.

144. Ogawa, T.; Aoyagi, S.; Miyasaka, T.; Sakai, K. *Sensors* **2009**, 9, 8271 – 8277.

145. Aoyagi, S.; Miyasaka, T.; Yoshimi, Y.; Sakai, K. *J. Artif.Org.* **2002**, *5*, 60–63.

146. You, F.; Zhou, Y.F.; Zhang, X.E.; Huang, Z.; Bi, L.J.; Zhang, Z.P.; Wen, J.K.; Chen, U.Y.; Jiang, G.B.; Zheng, M.H.. *Anal. Chem.* **2006**, *78*, 7138–7144.

147. Yang, Y.; Cai, J.; Rauscher, H.; Behm, R. J.; Goedel, W. A. *Chemistry* **2005**, 11, 3968–3978.

148. Bhatia, S. K.; Shriver-Lake, L. C.; Prior, K. J.; Georger, J. H.; Calvert, J. M.; Bredehorst, R.; Ligler, F. S. *Anal. Biochem.* **1989**, 178, 408-413.

149. Recombinant Fab-fragments of 19C7 mouse monoclonal antibodies (Cat.# RF4T21), available at http://www.hytest.fi/sites/hytest.fi/files/RF4T21.pdf.

150. Al-Hillawi, E.; Minchin, S. D.; Trayer, I. P. *Eur. J. Biochem.* **1994**, 225, 1195-1201.

151. Matagne, A.; Joris, B.; Frere, J. -M. *Biochem. J.* **1991**, 280, 553-556.

VITA

Jhony Orbulescu was born in Cluj-Napoca, Romania on November 14th, 1972. He received his elementary education at the General School, Gilau, Romania. His secondary education was completed at the High School for Natural Sciences, Cluj-Napoca, Romania. He entered Babeş-Bolyai University, Faculty of Chemistry and Chemical Engineering in 1992, where he completed the work for a B.Sc. in Chemistry and Physics in 1997. He then pursued a M.Sc. degree in applied electrochemistry which he received in June 1998. In August 1998 he was admitted in the graduate program at University of Miami, Department of Chemistry from which he graduated in May 2001 with a M.Sc. degree. After graduate he worked as Senior Research Associate in the Department of Chemistry at University of Miami under the supervision of Dr. Roger M. Leblanc. In August 2007, he re-enrolled in the Ph.D. program in the same department. He published a total of 36 articles, from which 12 since August 2007. From the work pursued for the PhD degree he published the following articles:

Orbulescu, J.; Leblanc, R.M. "Importance of the spreading solvent evaporation time in Langmuir monolayers" *Journal of Physical Chemistry C*, 2009, 113 (13), 5313–5315.

Orbulescu, J., Micic, M., Ensor, M., Trajkovic, S., Daunert, S.; Leblanc, R.M. "Human Cardiac Troponin I: A Langmuir Monolayer Study" *Langmuir,* 2010, 26 (5), 3268–3274.

Orbulescu, J.; Mullins, O. C.; Leblanc, R. M. "Surface Chemistry and Spectroscopy of UG8 Asphaltene Langmuir Film, Part 1" *Langmuir*, 2010, 26 (19), 15257–15264.

Orbulescu, J.; Mullins, O. C.; Leblanc, R. M. "Surface Chemistry and Spectroscopy of UG8 Asphaltene Langmuir Film, Part 2" *Langmuir*, 2010, *26* (19), 15265–15271.

Orbulescu, J., Micic, M., Ensor, M., Trajkovic, S., Daunert, S. and Leblanc, R.M. "Fluorescence-based Detection of Human Cardiac Troponin I Using a Chemically-attached mouse antibody modified quartz slide" *Analytical Chemistry*, *in preparation.*